INNOVATIVE FABRICATION OF SKIN-INTERFACED BIOELECTRONICS FOR MULTIMODAL HEALTH MONITORING

A Dissertation

presented to

the Faculty of the Graduate School

at the University of Missouri-Columbia

In Partial Fulfillment

of the Requirements for the Degree

Doctor of Philosophy

---

by

GANGGANG ZHAO

Dr. Zheng Yan, Dissertation Supervisor

MAY 2024

The undersigned, appointed by the dean of the Graduate School, have examined the thesis or dissertation entitled

INNOVATIVE FABRICATION OF SKIN-INTERFACED BIOELECTRONICS FOR MULTIMODAL HEALTH MONITORING

presented by GANGGANG ZHAO

a candidate for the degree of Doctor of Mechanical Engineering, and hereby certify that, in their opinion, it is worthy of acceptance.

Professor Zheng Yan,

Professor Guoliang Huang

Professor Matthew Maschmann

Professor Qingsong Yu

Professor Ozden Ilker

ACKNOWLEDGEMENTS

Over the past five years, I have been incredibly fortunate to receive a wealth of assistance and kindness from numerous individuals. It is with deep gratitude that I acknowledge their unwavering support.

First and foremost, I extend my profound appreciation to my academic advisor, Dr. Zheng Yan. His openness to including me in his research group and his outstanding support in refining my scientific approach and advancing my projects have been invaluable. Throughout my PhD studies, Dr. Yan has consistently provided me with insightful guidance, significant assistance, and has fostered my growth in scientific research. Without his support, the completion of my project and this thesis would not have been possible. I express my heartfelt thanks to him.

My heartfelt gratitude also goes to my group members, Dr. Yadong Xu and Dr. Ling Yun, for their invaluable help and kindness, aiding me in adapting to both academic pursuits and daily life abroad. I am equally thankful to Mr. Zehua Chen, Mr. Zanyu Chen, Dr. Sicheng Chen, Dr. Lin Shi, Dr. Feng Zhang, Mr. Qunle Ouyang, Ms. Qihui Fei, Ms. Xiaoyan Qian, and Mr. Shivam Goswami, for their encouragement and contributions to my research and personal growth.

Special thanks to Prof. Guoliang Huang and his student, Mr. Shaoyun Wang, for their support with theoretical simulations, and to Prof. Qingsong Yu and Dr. Yixuan Liao for providing access to their lab equipment. I am immensely grateful to Prof. Ozden Ilker for conducting crucial animal experiments, and to my committee member, Prof. Matthew Maschmann, for his timely responses and valuable insights.

Additionally, my appreciation extends to our collaborator, Prof. Pai-Yen Chen from the University of Illinois at Chicago, and his students, Dr. Zhilu Ye and Dr. Minye

Yang, for their expertise in NFC design. My thanks also to Prof. Jingwei Xie and his team, including Dr. Yajun Su and Dr. Syed Muntazir Andrabi from the Nebraska Medical Center, for assisting us with cytotoxicity and antibacterial experiments. I am also grateful to Dr. Yunchao Xie, Dr. Chi Zhang, and Mr. Bujingda Zheng from Prof. Jian Lin's group for their collaboration and support. I am truly grateful to the staff in the Mechanical Engineering department and the NextGen Health building for their day-to-day assistance.

Last but certainly not least, I express my deepest gratitude to my parents and family. Their constant support and care have been the cornerstone of my achievements, guiding me to this significant moment in my journey.

Table of Contents

ACKNOWLEDGEMENTS ii

List of Figures and Tables vii

Abstract xiii

Chapter 1. Pencil-Paper on-Skin Electronics 1

1.1 Introduction 2

1.2 Fabrication and characterization of pencil drawing of on-skin electronics on paper 4

1.3 High conductivity pencil-paper based patterns 8

1.4 Pencil-paper based biophysical sensors and thermal stimulators 12

1.5 Monitoring of cerebral activities via real-time EEG recording using pencil-paper based biophysical sensors 17

1.6 Characterization and on-body evaluation of pencil-paper-based on-skin biochemical sensors 19

1.7 Conclusion 23

1.8 Materials and methods 24

1.9 References 28

Chapter 2. Laser-Scribed Conductive, Photoactive Transition Metal Oxide on Soft Elastomers for Janus On-Skin Electronics and Soft Actuators 32

2.1 Introduction 33

2.2 Fabrication and characterization of the LSM 35

2.3 Cytotoxicity tests and MRI compatibility characterization of the LSM 40

2.4 Electromechanical properties of LSM on porous SEBS with kirigami cuts 42

2.5 Janus on-skin wearables based on LSM 43

2.6 Demonstration of Janus on-skin wearables in daily-life activities 59
2.7 Light-driven soft actuator based on laser-scribed MoO_2 63
2.8 Conclusion 67
2.9 Materials and methods 67
2.10 References 72
Chapter 3. Phase-Separated Porous Nanocomposite with Ultralow Percolation Threshold Enables Strain-Resilient Wireless Stretchable Bioelectronics 78
3.1 Introduction 80
3.2 Fabrication of PSPN and theoretical prediction 83
3.3 Strain-insensitive characteristics with ultralow percolation threshold 88
3.4 Radiofrequency properties of PSPN spiral coils under tensile strain 94
3.5 Strain-insensitive stretchable wireless powering system 97
3.6 Wireless stretchable bioelectronics for multiplexed biochemical sensing 101
3.7 Conclusion 105
3.8 Materials and methods 106
3.9 References 111
Chapter 4. Multifunctional Cellulose Nanofibril Interfaces for High-Quality Printing, Strain Resilience, and Microfluidics in Porous Bioelectronics 117
4.1 Introduction 119
4.2 Fabrication of CNF inks and engineering CNF interfaces on porous substrates 122
4.3 CNFI enabled strain resilient wearable bioelectronics 126
4.4 Design and characterization of the CNFI for MFCs 134
4.5 Antimicrobial, biocompatibility and hemocompatibility study 138
4.6 Wireless and multimodal metabolism types monitoring 139
4.7 Conclusion 144

4.8 Materials and methods 145

4.9 References 149

Chapter 5. Conclusion 154

VITA 156

List of Figures and Tables

Figure 1.1. Concept and SEM of pencil-paper on-skin electronics……..…..…5

Figure 1.2. Raman spectrum of pencil-drawn graphite on papers…….....6

Figure 1.3. Electronic mechanical characterization of pencil-paper on-skin electronics with kirigami cuts…….....6

Figure 1.4. Breathability and adhesive characterization pencil-paper on-skin electronics…….……..8

Figure 1.5. Conductivity and Annetta design based on pencil-drawn patterns on papers ……...…….....10

Figure 1.6. Pencil-drawn 2D buildings and origami-inspired umbrella-like 3D structures on papers as interconnects integrated with LEDs…….……...11

Figure 1.7. Impedances and ECG of the skin–electrode interface of pencil-drawn graphite electrodes and conventional Ag/AgCl…….…….....12

Figure 1.8. Long-term ECG recording from the chest of a human volunteer using the pencil–paper on-skin electrophysiological sensor.…….…….....13

Figure 1.9. EMG recorded from the forearm of a human volunteer using pencil–paper on-skin sensor and conventional Ag/AgCl gel electrodes….…….....14

Figure 1.10. On-skin bioelectronics based on pencil and adhesive water-soluble paper.……....15

Figure 1.11. Pencil-paper on-skin temperature sensor and joule-heating……...…16

Figure 1.12. Pencil-paper-enabled reconfigurable assembly.…….....17

Figure 1.13. Monitoring of cerebral activities via real-time EEG recording……...18

Figure 1.14. Schematic illustrations of pencil-paper-based sweat biochemical sensors for in-situ measurement of pH, UA and glucose in sweat.……...…19

Figure 1.15. The performances of pencil-based pH sensor...…….…….....20

Figure 1.16. The performances of pencil-based UA sensor....…….…….…...21

Figure 1.17. The performances of pencil-based glucose sensor...…….....22

Figure 1.18. On body test of pencil-based sweat sensor……. ……..…..23

Figure 2.1. Schematic illustration of laser scribing of MoO_2 on supporting substrates…….....35

Figure 2.2. Optical image and SEM of LSM...…….……..…….....36

Figure 2.3. XRD pattern of LSM on porous SEBS...…….…….....37

Figure 2.4. Raman spectrum and TEM image of LSM on porous SEBS…….....37

Figure 2.5. Conductivity of LSM and fabrication of LSM on various substrates.....38

Figure 2.6. Stability of LSM on porous SEBS...…….……..…….…..39

Figure 2.7. Breathability test of LSM on porous SEBS...…….……...40

Figure 2.8. Cytotoxicity tests of LSM on porous SEBS...…….…….....41

Figure 2.9. MRI comptability tests of LSM on porous SEBS...…….….....42

Figure 2.10. Electromechanical properties of LSM on porous SEBS with kirigami cuts……43

Figure 2.11. Exploded view of the Janus on-skin wearable based on LSM patterned on porous SEBS.....…….……..44

Figure 2.12. Schematic illustration and optical image of Janus wearable.....…….45

Figure 2.13. LSM-based on-skin temperature sensor and joule-heating.....…46

Figure 2.14. Contact impedances of the skin-device interface of LSM electrodes fabricated on porous SEBS.....…….……...…….47

Figure 2.15. On-body evaluation of the LSM-based ECG sensor.....…….....…48

Figure 2.16. On-body evaluation of the LSM-based EEG sensor.....……...…...49

Figure 2.17. On-body evaluation of the LSM-based EMG sensor.....…….....50

Figure 2.18. In-vitro evaluation of the LSM-based glucose sensor.....…….……..51

Figure 2.19. In-vitro evaluation of the LSM-based uric acid sensor.....…….....52

Figure 2.20. In-vitro evaluation of the LSM-based caffeine sensor.....……...…53

Figure 2.21. In-vitro evaluation of the LSM-based UV sensor.....…….....…54

Figure 2.22. In-vitro evaluation of the LSM-based humidity sensor.....……...…..55

Figure 2.23. In-vitro evaluation of the LSM-based ethanol sensor.....…..…...……...56

Figure 2.24. In-vitro evaluation of the LSM-based NH_3 sensor.....……..…57

Figure 2.25. In-vitro evaluation of the LSM-based biogenic amine gases sensor……58

Figure 2.26. Wireless transmission system for Janus wearables.....……59

Figure 2.27. Illustration (left) and the UV light density and relative humidity on the campus playground and a nearby trail (right) measured with the LSM-based Janus wearable.....…….……...…60

Figure 2.28. Daily activities monitoring using the LSM-based Janus wearable.....61

Figure 2.29. Alcohol intake monitoring using the LSM-based Janus wearable……..62

Figure 2.30. Breath alcohol concentrations (BrAC) measured by the LSM-based alcohol gas sensor.....…….……63

Figure 2.31. LSM-based light-driven soft actuator.....…….…….……63

Figure 2.32. Optical images of LSM-based soft actuators under bending.....…64

Figure 2.33. 2D and reconfigurable multilayer 3D architectures based on LSM-based soft actuators…….....64

Figure 2.34. Four reconfigurable multilayer 3D architectures formed by combining LSM soft actuators with mechanically assembled 3D structure……..65

Figure 2.35. LSM based reshapable wearable airflow sensor.....……..…65

Figure 2.36. Dynamic resistance responses of six sensing channels of the reshapable wearable airflow sensor at the 2D configuration and 3D configuration .....…….……...66

Figure 2.37. LSM-based worm-like smart soft robot integrated with the ammonia sensor……66

Figure 3.1. Schematic illustration of a cross-sectional view of the phase-separation process.....…….……82

Figure 3.2. Schematic illustration of porous and nonporous Ag NWs nanocomposites at original and stretched states.....…….……...…83

Figure 3.3. Schematic illustration of the isothermal ternary phase diagram of polymer, solvent, and nonsolvent.....…….…….....84

Figure 3.4. SEM images and corresponding particle size distributions of PSPN.....85

Figure 3.5. SEM images and corresponding particle size distributions of PSPN with 1-butanol.....…….……...…86

Figure 3.6. Electrical resistances as a function of applied strain.....……87

Figure 3.7. SEM and electrical conductivities of PSPN with different Ag NWs concentrations.....88

Figure 3.8. Percolation thresholds of PSPN with 1-butanol.....89

Figure 3.9. SEM images and electrical mechanical characterizations of PSPN under mechanical deformation.....90

Figure 3.10. SEM images of nonporous Ag NWs nanocomposite before and after 100% strain.....91

Figure 3.11. Comparison of electromechanical characteristics with other reported elastic conductors.....92

Figure 3.12. Demonstration of PSPN resilience to different physical damage and its mechanism 93

Figure 3.13. Demonstration of the water vapor transmission rate and Young's modulus of nonporous nanocomposites and PSPN.....94

Figure 3.14. Two-port network model of the stretchable wireless power transfer system and simulations under strain 95

Figure 3.15. Characterization of the PSPN coil under strain.....95

Figure 3.16. Characterization of the PSPN coil under bending.....96

Figure 3.17. Characterization of the cattering parameters and transfer efficiency of PSPN coil under strain 96

Figure 3.18. Characterization of the cattering parameters and transfer efficiency of nonporous coil under strain.....97

Figure 3.19. Schematic of the structure and Maxwell simulations of the magnetic field generated by a soft transmitter on human skin.....98

Figure 3.20. Characterization of the coupling coefficient of stretchable PSPN coil under different condition.....99

Figure 3.21. Implantable PSPN coil and corresponding demonstrations.....101

Figure 3.22. Schematic illustration and characterization of the stretchable, battery-free, and wireless LC circuit-based bioelectronics for biochemical sensing.....102

Figure 3.23. Characterization of the stretchable, battery-free, and wireless LC circuit-based bioelectronics for multiplexed biochemical sensing.....103

Figure 3.24. Characterization of the stretchable, battery-free, and wireless LC circuit-based bioelectronics for Na^+ sensing under strain.....……..……104

Figure 3.25. On-body stretchable bioelectronics for multiplexed biochemical sensing……105

Figure 3.26. Real-time glucose and alcohol concentration monitoring in human sweat using the multiplexed wireless biochemical sensing system.....……..…..106

Figure 4.1. Illustration of multifunctional CNFI for high-quality printing, stain resilience, and microfluidics in porous soft bioelectronics.....…….121

Figure 4.2. TEM image of CNF bundles and CNF.....……..….122

Figure 4.3. Rheological properties of the CNF inks.....…….123

Figure 4.4. CNFI on porous SEBS.....……..…….124

Figure 4.5. Bifunctional PEDOT: PSS/ Ag NWs inks for printing.....…….125

Figure 4.6. High quality printing on CNFI.....…….126

Figure 4.7. CNFI for strain isolation.....…….127

Figure 4.8. FEA simulation of the stress distribution for the CNFI on porous SEBS and no porous SEBS.....……..…….127

Figure 4.9. Molecular dynamics simulation of the interfaces between CNF and SEBS.....…….128

Figure 4.10. Strong interfaces between CNF and porous SEBS.....……..….129

Figure 4.11. Electromechanical performances of conductive patterns on CNFI.....130

Figure 4.12. Performances comparison of various electrodes on CNFI and porous SEBS under strain ……..131

Figure 4.13. Performances comparison of wireless power transmitter system printed on CNFI and porous SEBS under strain ……....132

Figure 4.14. ECG signals recorded using the electrodes printed on the CNFI and bare porous SEBS ……..…….133

Figure 4.15. Performance of Na^+ sensor pinted on CNFI under strain ……..133

Figure 4.16. Liquid diffusion on CNFI…….…….135

Figure 4.17. Schematic illustration of the design of MFCs…….……..….135

Figure 4.18. Filling progress of the CNFI based MFCs…….....136

Figure 4.19. Refreshing progress of the CNFI based MFCs for β-HB……...137

Figure 4.20. Refreshing progress of the CNFI based MFCs for glucsoe……...137

Figure 4.21. Antimicrobial, biocompatibility and hemocompatibility study…….139

Figure 4.22. Illustration of the CNFI enhanced wearable bioelectronics that continuously monitor multimodal biochemicals and ECG from skin for diverse metabolism monitoring……..….140

Figure 4.23. Characterizations of the nicotinamide adenine dinucleotide (NADH) and β-hydroxybutyrate (β-HB) sensors…….141

Figure 4.24. Characterizations of the glucose sensor…….142

Figure 4.25. Characterizations of the glucose and β-HB sensors under strain…..….143

Figure 4.26. On body evaluation of the CNFI enhanced wearable bioelectronics for diverse metabolism monitoring……..….144

Table 2.1. Electronic components used in the mobile data acquisition circuit……72

Abstract

INNOVATIVE FABRICATION OF SKIN-INTERFACED BIOECTRONICS FOR MULTIMODAL HEALTH MONITORING

by

Ganggang Zhao

Skin-interfaced wearable electronics capable of real-time monitoring of vital biophysiological signals have gained significant attention. However, traditional wearable devices often face challenges such as the use of costly materials, intricate fabrication processes, and poor stability under mechanical stress and prolonged wear. Moreover, the limited breathability of substrates can compromise comfort and cause inflammation over long-term use. My research primarily addresses these challenges by innovating materials, adapting fabrication technologies, and modifying devices to enhance breathability, stretchability, affordability, and other unique characteristics essential for on-skin wearables.

The dissertation starts from the development of cost-effective, eco-friendly, and breathable wearable electronics. Direct writing technique to apply conductive graphite patterns onto cellulose paper, facilitating the development of on-skin electronics (chapter 1). Then laser-scribed molybdenum dioxide (LSM) with high electrical conductivity, biocompatibility, chemical stability, and MRI compatibility.is developed to achieve mask-free, high-resolution, and large-scale fabrication of highly conductive materials on flexible substrates and Janus devices capable of monitoring both bodily and environmental signals (Chapter 2) is also obtained. Using phase-separation technology, we develop porous composites of silver nanowires (Ag NWs) with an ultralow percolation threshold. These composites enable strain-resilient near-field communication (NFC), facilitating wireless powering and data transmission for both

skin-interfaced and implantable bioelectronics (Chapter 3). Last work is focus on the engineering cellulose nanofiber interfaces (CNFI) on porous substrates to achieve surface flatness for high-quality bioelectronics printing and to construct mechanical heterogeneity for strain-resilient bioelectronics. Additionally, CNFI for microfluidic channel (MFC) is also constructed for continuous and real-time collection, transportation, and discharge of sweat (Chapter 4).

Chapter 1. Pencil-Paper on-Skin Electronics

This chapter is copied and reformatted from a paper published in *Proceedings of the National Academy of Sciences,* 117 (31), 18292-18301 (2020) (*1*).

Abstract: Pencils and papers are ubiquitous in our society and have been widely used for writing and drawing, because they are easy-to-use, low-cost, widely accessible, and disposable. However, their applications in emerging skin-interfaced human health monitoring and interventions are still not well explored yet. Herein, we report a variety of pencil-paper-based on-skin electronic devices, including biophysical (temperature, biopotential) sensors, sweat biochemical (pH, uric acid, glucose) sensors, thermal stimulators, and humidity energy harvesters. Among these devices, pencil-drawn graphite patterns (or combined with other compounds) serve as conductive traces and sensing electrodes, and commercial office-copy papers work as flexible supporting substrates. The enabled devices can perform real-time, continuous, and high-fidelity monitoring of a range of vital biophysical and biochemical signals from human bodies, including skin temperatures, electrocardiograms, electromyograms, alpha, beta and theta rhythms, instantaneous heart rates, respiratory rates, and sweat pH, uric acid, and glucose, as well as deliver programmed thermal stimulations. Notably, the qualities of recorded signals are comparable to those measured with conventional methods. In addition, pencil-paper-based antennas, 2D and 3D circuits with LEDs and batteries, reconfigurable assembly, and biodegradable electronics (based on commercial water-soluble papers) are explored.

1.1 Introduction

On-skin electronics, also termed as epidermal electronics or skin-interfaced electronics, have demonstrated a variety of promising applications in human healthcare, human-machine interfaces, and virtual and augmented reality, among many others (*2-11*). Currently, on-skin electronics are usually made by patterning conventional inorganic electronic materials (e.g., copper, gold, silicon), novel organic electronic materials [e.g. poly(3,4-ethylenedioxythiophene) polystyrene sulfonate, poly(3-hexylthiophene)], or emerging nanomaterials (e.g., graphene, carbon nanotubes, silver nanowires) on mechanically compliant polymer supporting substrates (e.g., silicone elastomers, polyimide, polyethylene terephthalate) (*2-11*). Consequently, the state-of-the-art on-skin electronics often suffer from expensive precursor materials, costly fabrication facilities, complex fabrication processes, and limited disposability. For example, well-established fabrication procedures of on-skin electronics are usually associated with spin-coating, photolithography, vacuum deposition, and dry/wet etching, which are complicated, time consuming, and expensive. Solution-based printing techniques can enable simple and scalable fabrication of flexible devices but usually suffer from expensive facilities, tedious efforts in ink formulations and complex post-printing processes (*12,13*). In addition, most polymer substrates used in on-skin electronics need hundreds of years to decompose in natural environments. Considering that on-skin electronics should be one-time use to minimize infection risks, their future wide implementation in our daily life would result in dramatic accumulations of electronic wastes. It is worth noting that emerging physically transient and recyclable bioelectronics might address the concerns of environmental pollutions (*14,15*). However, their potential is dampened by expensive precursor materials, costly fabrication facilities, and

sophisticated fabrication processes.

Papers have a history of more than 2000 years and have been widely used in our daily life ranging from packaging to printing and information display. Papers are usually made of natural cellulose fibers and can completely decompose within six weeks. Also, papers are one of the most inexpensive materials (0.1 cent dm^{-2}) as compared to polymer substrates such as polyethylene terephthalate (≈2 cent dm^{-2}) and polyimide (≈30 cent dm^{-2}) (*16*). In addition, their high flexibility and breathability can benefit their applications in on-skin electronics. Pencils were invented in the 16th century and have been used for writing and drawing. Pencil lead is composed of fine graphite powers with various additives, by which pencils are classified into "H" and "B" categories. "H" and "B" refer to hardness and blackness, respectively. The graphite particles are rubbed off due to friction between the pencil lead and the rough and porous paper substrate in a writing cycle, where conductive graphite flakes are transferred to papers. Despite the recent progress of their applications in supercapacitors and strain gauges (*17,18*), pencil-paper-based on-skin electronic devices, which can stick to human bodies for a long term, record vital biophysical and biochemical signals in a high-fidelity fashion, harvest energy from ambient humidity, and deliver programmed physical and chemical interventions, are still lacking.

In this work, we explore the pencil drawing of a variety of bioelectronic devices on commonly used office-copy papers with commercial 9B pencils. Here, pencil-drawn graphite patterns (or combined with other compounds) work as conductive traces and sensing electrodes, and paper serve as flexible supporting substrates as well as the basis materials for ambient humidity energy harvesters. Besides, a trace number of adhesive materials (Silbione RT Gel 4717 A/B; Elkem Silicones; the weight ratio of Silbione and paper: ~5:100) is spray-coated onto the bared regions of pencil-paper on-

skin electronics to improve the skin-device adhesion. The prototypic device examples include temperature sensors, electrophysiological (i.e., biopotential) sensors, electrochemical sweat sensors, joule-heating elements, and ambient humidity energy harvesters, that can record a variety of vital biophysical information from bodies [including skin temperatures, electrocardiograms (ECGs), electromyograms (EMGs), alpha, beta and theta rhythms, instantaneous heart rates, and respiratory rates] in a real-time, continuous and high-fidelity manner, as well as provide programmed thermal stimulations; in-situ analyze three proof-of-concept sweat biomarkers, including pH, uric acid (UA) and glucose, with high sensitivity and selectivity. Besides, pencil-paper-based antennas, 2D/3D circuits with LEDs and batteries, biodegradable electronics (based on water-soluble paper) and reconfigurable assembly are explored. The fabrication and characterization are detailed in SI Appendix Methods.

1.2 Fabrication and characterization of pencil drawing of on-skin electronics on paper

Pencil lead is usually composed of graphite, clay, and wax. High graphite contents could enable drawing of high-electrical-conductivity patterns on paper. Here, a 9B sketching pencil with ~93% graphite content by weight is used for drawing of a variety of on-skin bioelectronic devices on office-copy papers (~100 μm thick; Staples Inc; **Figure 1.1A**). **Figure 1.1B** provides a typical optical image of fabricated on-skin bioelectronic devices, including temperature sensors, electrophysiological sensors, sweat electrochemical sensors and humidity energy harvesters, which have open-mesh, serpentine-like layouts. Similar device layouts of temperature sensors can also be used as joule-heating elements. Scanning electron microscope (SEM) images show that graphitic materials are successfully transferred from the pencil lead to the rough and

porous cellulose paper substrate, where a boundary is clearly observed (**Figure 1.1C** and **D**).

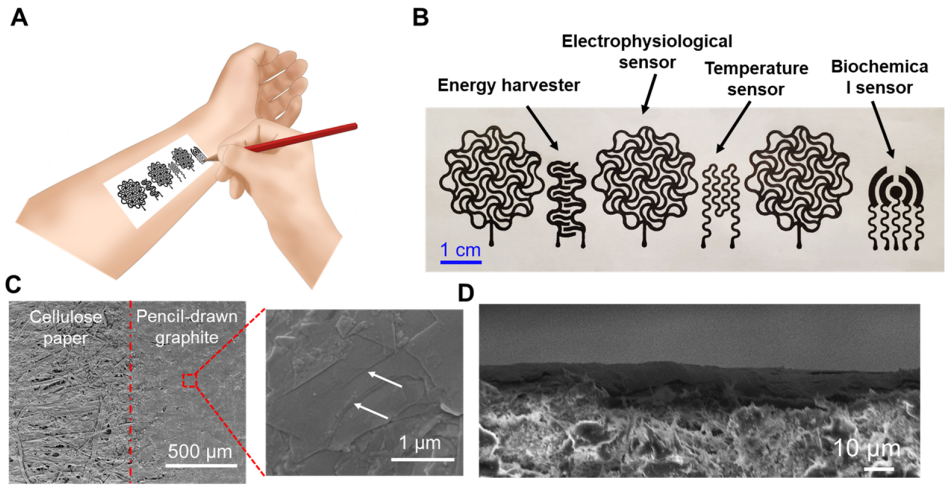


Figure 1.1. A, Conceptual illustrations of drawing on-skin electronics on papers using a 9B sketching pencil. **B**, Photograph of pencil–paper on-skin electronics. **C**, SEM images of pencil-drawn graphite on papers. Arrows indicate the multilayer structures and edges of graphitic flakes. **D**, Cross-sectional SEM image of pencil-drawn graphite on the paper with 15 writing cycles, indicating the thickness of the graphite layer is around 6 μm.

The shear-peeling force of the direct-drawing process creates multilayer graphitic materials with many open-edge structures due to their anisotropic mechanical properties. Raman spectrum of pencil-drawn graphite on paper shows characteristic spectrum with three main peaks centered at 1332, 1582 and 2691 cm^{-1}, which can be attributed to D, G and 2D bands, respectively (**Figure 1.2A**) (*19*). The G band is due to the in-plane E_{2g} mode, which arises from the stretching of C-C bond, while D and D' bands can be attributed to the defects at the graphite edges. Besides, the open-mesh, serpentine-like layout was adopted for the fabrication of bioelectronic devices in **Figure 1.1B**. mainly because electrical performances of such structures are less susceptible to mechanical deformations. For example, only a small resistance change (~20%) was observed at a bending radius of 1.5 mm (**Figure 1.3A**).

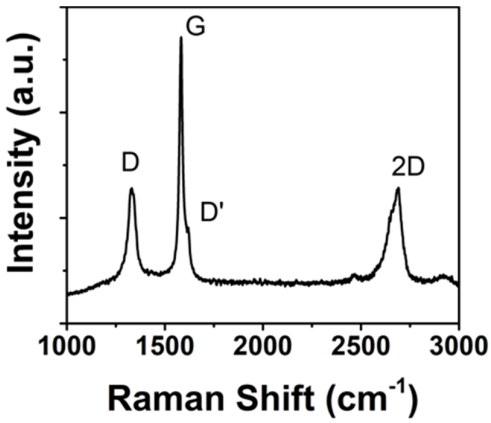


Figure 1.2. Raman spectrum of pencil-drawn graphite on papers.

In addition, we adopt kirigami cuts (*23*) to overcome the papers' intrinsically poor stretchability and high modulus (**Figure 1.3B** and **C**). With kirigami cuts, the electrical resistance of pencil-drawn, serpentine-like graphite patterns show no measurable change under up to ~150% tensile strain (**Figure 1.3D**). Moreover, after 1,000 cycles

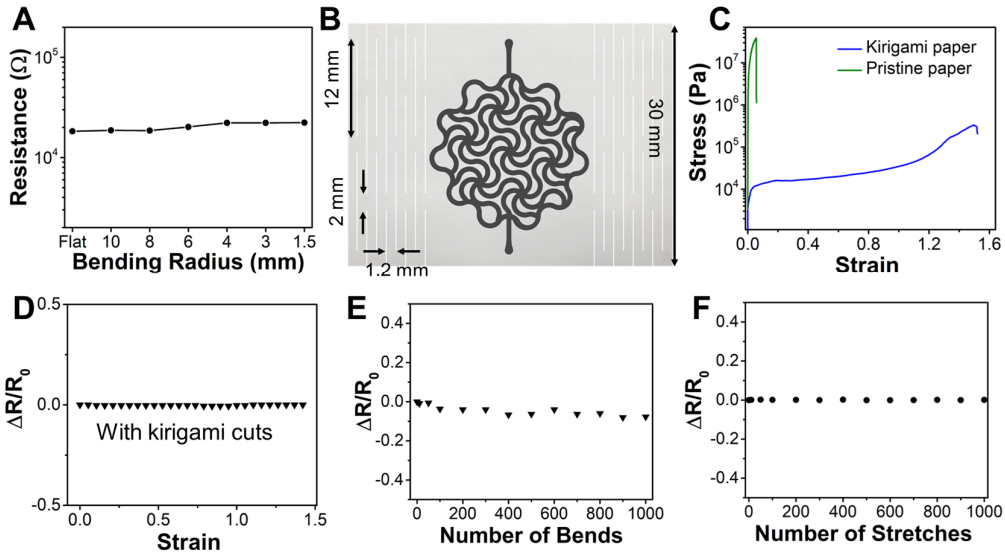


Figure 1.3. A, Variations in the electrical resistance of pencil-drawn graphite as a function of bending radius. **B**, A schematic illustration of pencil-drawn graphite patterns on papers with kirigami cuts. **C**, Stress-strain curves of the pristine paper and the paper with kirigami cuts, indicating the significantly improved stretchability and dramatically reduced modulus. **D**, Variations in the sheet resistance of pencil-drawn graphite on papers as a function of writing cycles.

of bending tests (bending radius: 6 mm) and uniaxial stretching tests (tensile strain: 100%), only ~8% and ~0.1% resistance changes were observed, respectively (**Figure 1.3E** and **F**). Such excellent electromechanical performances are sufficient for a broad range of on-skin bioelectronic applications considering relatively small natural deformations of human skins (bending: > ~140 mm for chest and > ~50 mm for foot; stretching: up to 50-80%) (*11, 25*).

Furthermore, commonly used office-copy paper is not sticky and cannot form intimate contact with the skin, which is of extreme importance for long-term and high-fidelity recording of vital physiological signals from human bodies. To overcome this handicap, we spray coat Silbione, which is biocompatible and has low elastic modulus (~3.0 kPa), onto bare regions of on-skin electronic devices to improve their stickiness. As shown in **Figure 1.4A**, a trace amount of Silbione coating can dramatically improve the stickiness of the resulting on-skin electronic devices. The measured adhesion force from the forearm of a human volunteer increases from ~0.01 N to ~0.85 N after Silbione coating. Here, the weight ratio of the spray coated Silbione and paper is ~5:100. The enabled sticky pencil-paper on-skin devices can stay on human bodies for more than three days. Besides, high breathability is desirable for on-skin electronics, which can expedite skin perspiration evaporation, minimize sweat accumulation, and alleviate inflammatory reactions (*26-28*). The optimal amount of spray coated Silbione is obtained based on a trade-off between the stickiness and breathability (**Figure 1.4B** and **C**). As shown in **Figure 1.4D-F**, after an optimal amount of spray-coated Silbione (the weight ratio of Silbione and paper: ~5:100) was obtained for the fabrication of pencil-paper on-skin electronics, the device exhibits high adhesive to skin and the paper still exhibits a decent water vapor transmission rate (2137 g m^{-2} day^{-1}), which is sufficiently higher than that of human skin (204 g m^{-2}

day^{-1}) (*28*). Here, Silbione is used to improve the skin adhesion of commonly used office-copy papers. Notably, our results also demonstrate that pencils can be used to directly draw high-quality bioelectronic devices on commercially available adhesive papers without needing additional Silbione coating to further simplify the fabrication process. More details are provided in subsequent sections.

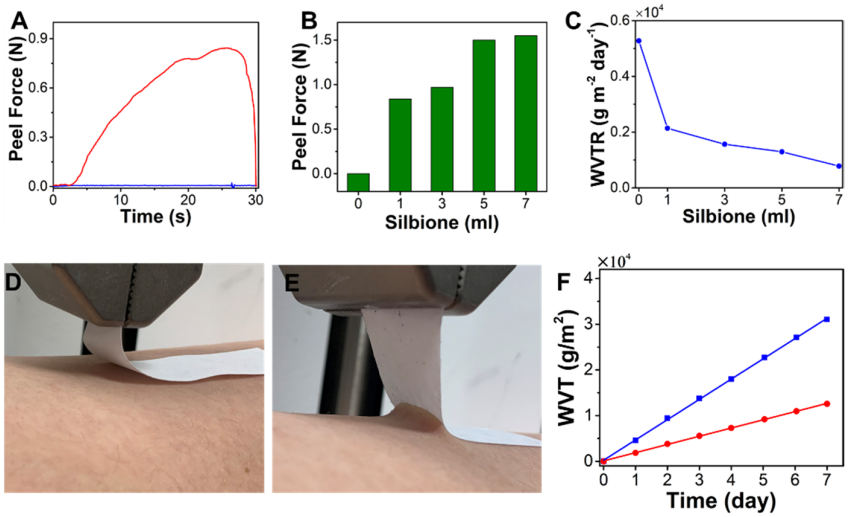


Figure 1.4. A, Peel-adhesion tests of pristine papers (blue) and papers with spray-coated Silbione (red) on the forearm of a human volunteer, indicating the significantly enhanced adhesion after Silbione coating. Peel-adhesion test (**B**), water vapor transmission rate (WVTR) (**C**) of the papers with different amounts of spray-coated Silbione. Optical images of the papers without (**D**) and with (**E**) Silbione coating. Here, Silbione solutions were prepared by first equally mixing the base and curing agent, followed by the dilution with hexane to ~70 mg ml^{-1}. Then the solution was spray-coated onto the paper substrate at a distance of ~10 cm through a stencil mask using a commercial airbrush (G222, Master Airbrush), and then dried in the air at room temperature. During the peeling test, the sample sizes are 1.5×4 cm^2. After cleaning the skin, alcohol swabs were applied to wet the skin, followed by the lamination of the papers spray coated with Silbione after the skin was dried. **F**, Water vapor transmissions (WVT) of pristine papers (blue) and papers coated with Silbione (red) as a function of the elapsed time.

1.3 High conductivity pencil-paper based patterns

The electrical conductivity of pencil-drawn graphitic materials on paper is systematically investigated by orthogonally ruler-guided drawing for a number of cycles. As shown in **Figure 1.5A**, the sheet resistance of pencil-drawn graphite is inversely correlated with writing cycles, decreasing from ~10 kΩ sq^{-1} at the first cycle to ~160 Ω sq^{-1} at the 15th cycle. In this research, 15 writing cycles were used for the fabrication of on-skin devices with the thickness of graphite layers at ~6 μm (**Figure 1.1C**). Also, the patterns drawn by 9B pencils exhibit better electrical conductivities than the ones drawn by others largely because of their higher graphite contents (**Figure 1.5B**). The high electrical conductivity of pencil-drawn traces on office-copy papers makes them suitable for a variety of on-skin electronic devices (e.g., biophysical, and biochemical sensors, humidity energy harvesters, antennas, interconnects). To exemplify their potential use in radio-frequency (RF) and wireless communication applications, we have applied the pencil-drawing method to build a low-profile planar dipole antenna onto the office-copy paper substrate (**Figure 1.5C-I**). Center-fed half-wavelength dipole antennas with an omnidirectional radiation pattern are widely used for radio transmitting and receiving applications (*21*). **Figure 1.5C** shows the schematic of this type of antenna with its dipole-arms formed by multiple layers of pencil-drawn graphite on paper. The in-phase oscillating AC currents induced on dipole arms generate an omnidirectional radiation pattern in the far-field (Fraunhofer) region. Intuitively, increasing the number of stacked pencil-paper layers can reduce the sheet resistance, thus enhancing the radiation efficiency and the realized gain of RF antennas (**Figure 1.5D-F**). **Figure 1.5G** presents the reflection coefficient (S_{11}) for half-wavelength dipole antennas consisting of 1, 5 and 12 layers (see **Figure 1.5F** for the manufactured antenna on the paper substrate). We find that the measurement results agree well with simulated ones, indicating that increasing the

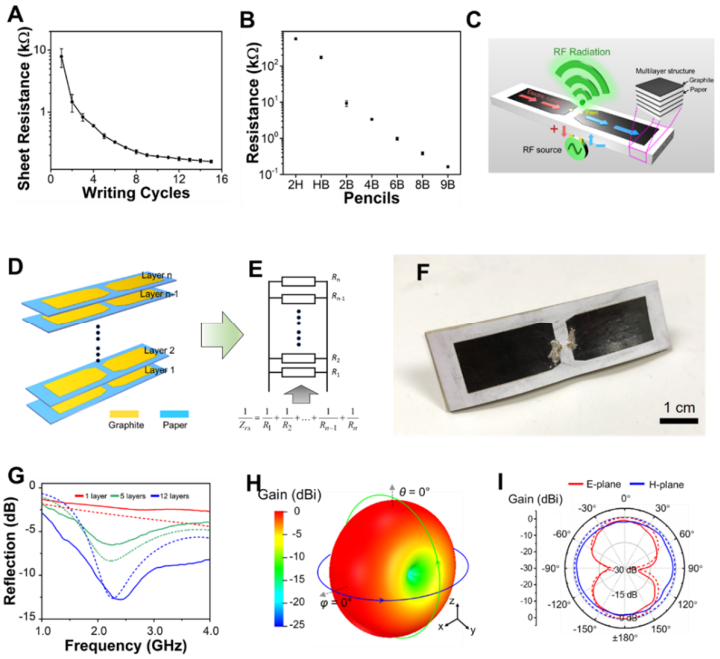


Figure 1.5. **A**, Variations in the sheet resistance of pencil-drawn graphite on papers as a function of writing cycles. **B**, Sheet resistances of the patterns that were drawn with various types of pencils (15 writing cycles) on office-copy papers. Error bars in **A** and **B** represent the SDs of three individual samples. **C**, Schematic of a planar dipole antenna based on the multilayered structure of pencil-drawn graphite and paper. **D**, Schematic, and equivalent circuit model (**E**) for the multilayered paper-pencil-based antennas. Each pencil-drawn graphite layers can be seen as a shunt resistance, and the total sheet resistance is reduced by increasing the number of graphite layers. **F**, Photograph of the fabricated 12 layers of pencil-paper-based dipole antenna. **G**, Reflection (S_{11}) spectra for the pencil-paper-based dipole antenna with different numbers of stacked layers (5G midband). **H**, Simulated 3D and simulated and measured 2D (**I**) radiation patterns for the pencil-paper-based dipole antenna (12 layers) working at 2.3 GHz. In **G** and **I** solid and dashed lines represent the measurement and simulation results, respectively.

number of layers of pencil-drawn graphite on paper can improve the impedance matching condition, owing to the reduction of the antenna's loss resistance (which is associated with the effective sheet resistance). When 12 layers of pencil-drawn graphite on paper are used, a -10 dB bandwidth of 0.77 GHz can be achieved at 2.3GHz (4G LTE and Bluetooth band). **Figure 1.5H** and **I** present the simulated and

measured radiation patterns at 2.3 GHz for the 12-layer pencil-paper-based antenna. We find a good agreement between numerical simulations and experimental results, showing that the maximum realized gain is ~-1.63 dBi. This value is slightly lower than that of an ideal half-wavelength dipole made of perfect conductor (2.15 dBi) but is comparable to those measured from the-state-of-the-art flexible dipoles made of conductive polymers (*21*), ink-jet printed metals (*22*) and thin film metal (*23*). Finally, we should note that the realized gain can be further improved by stacking more pencil-paper layers. According to our simulation results, a realized gain of 0.80 dBi can be achieved by stacking 25 pencil-paper layers. This simple and low-cost manufacturing technique may open up new avenues for development of flexible and disposable RF electronics (e.g., RFID and IoT tags).

In addition, as shown in **Figure 1.6**, pencil-drawn interconnects on office-copy papers can integrate with commercial electronic components (e.g., LEDs, batteries) in both 2D and 3D circuits. These results, together with the results of bioelectronic sensors and humidity energy harvesters that are described subsequently, indicate the possibility of developing pencil-paper-based whole wearable systems, which is worth exploring in the future.

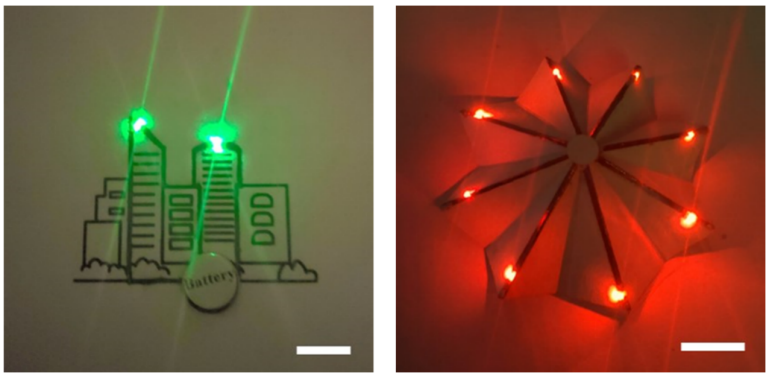


Figure 1.6. Pencil-drawn 2D buildings on papers as interconnects integrated with two green LEDs and one battery (left) and origami-inspired umbrella-like 3D paper structures with pencil-drawn interconnects and eight red LEDs (right). Scale bars: 2 cm.

1.4 Pencil-paper based biophysical sensors and thermal stimulators

The on-skin electrophysiological sensor consists of pencil-drawn reference, ground, and measurement electrodes. **Figure 1.7A** shows that the skin-device contact impedance of pencil-drawn electrophysiological electrodes is ~40 kΩ at 100 Hz, comparable to conventional silver/silver chloride (Ag/AgCl) gel electrodes (~37 kΩ at 100 Hz). The magnified ECG signal indicates distinguishable P-wave, QRS complex, and T-wave (**Figure 1.7B**). As shown in **Figure 1.7C**, the signal-to-noise ratio (SNR) of the ECG signals, recorded with pencil-paper on-skin electrophysiological sensors, is ~30 dB, comparable to the results measured from Ag/AgCl electrodes (~32 dB).

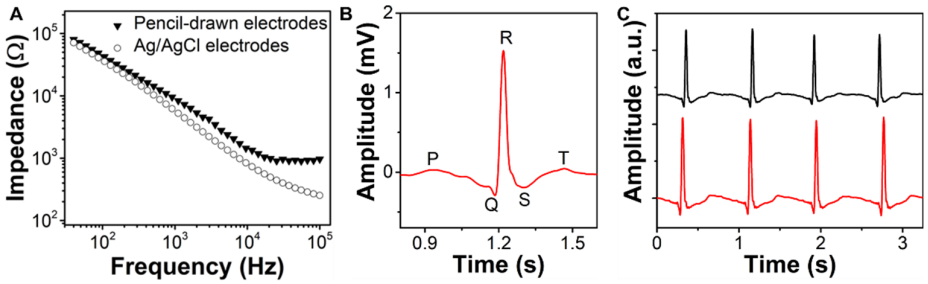


Figure 1.7. A, Impedances of the skin-electrode interface of pencil-drawn graphite electrodes and conventional Ag/AgCl electrodes, measured from the forearm of a human volunteer. **B**, Magnified ECG signals recorded with pencil-paper on-skin electrophysiological sensors, showing distinguishable P-wave, QRS complex and T-wave. **C**, Comparisons of ECG signals recorded using pencil-paper on-skin electrophysiological sensors (black; SNR: 30 dB) and conventional Ag/AgCl electrodes (red; SNR: 32 dB).

Figure 1.8A shows that pencil-paper on-skin electrophysiological sensors can measure ECG from human chests in a continuous and high-fidelity manner. The signal-to-noise ratios of the recorded ECG signals before and after continuous measurement for 24 hours are 30.9 and 32.6 dB, respectively, indicating high stability. Furthermore, respiratory rates can be determined from the recorded ECG signals by analyzing intrathoracic impedance variations caused by human breathing (*31*).

Specifically, the R peak amplitude in QRS complex decreases as the intrathoracic impedance increases during the inspiration, while it increases as the latter decreases during the expiration, and no obvious amplitude change is observed when holding breath (**Figure 1.8B**). The extracted respiratory rates match well with those obtained by visual counting (**Figure 1.8C**). Meanwhile, instantaneous heart rates (containing the information of heart rates and heart rate variations) can be determined by the R-to-R intervals of the ECG signals recorded with pencil-paper on-skin electrophysiological sensors, which agree well with the results extracted from the ECG signals measured with Ag/AgCl electrodes (**Figure 1.8D**).

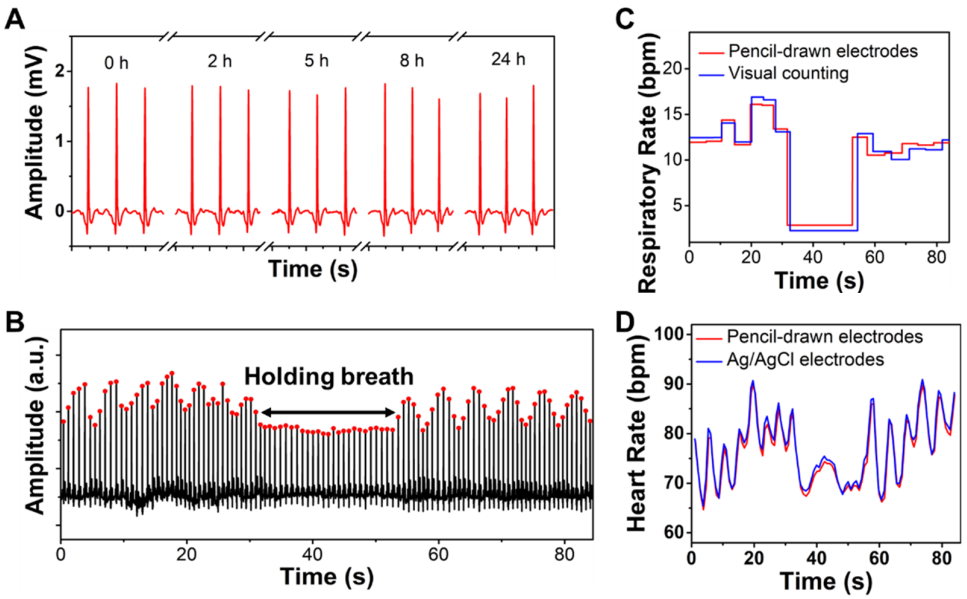


Figure 1.8. A, Long-term ECG recording from the chest of a human volunteer using the pencil-paper on-skin electrophysiological sensor, indicating high stability. **B**, Dynamic amplitude responses of the R peaks in the ECG signals while the volunteer held the breath for ~25 s. **C**, Respiratory rates determined by the R peak amplitude variations in G and visual counting by physician. **D**, Comparisons of instantaneous heart rates determined from the R-to-R peak intervals in the ECG signals recorded with pencil-paper on-skin sensors and conventional Ag/AgCl electrodes.

In addition, **Figure 1.9** demonstrate that EMG signals with a SNR of ~30 dB can be

collected from the forearm (flexor carpi radialis muscle) of a human volunteer using pencil-paper on-skin electrophysiological sensors, which are quantitatively comparable to the data recorded with Ag/AgCl electrodes (~32 dB). The real-time EMG recording is useful in human-machine interfaces (*26*).

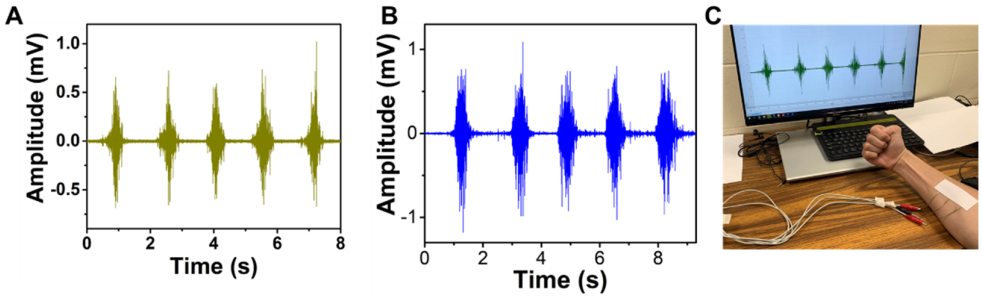


Figure 1.9. A, EMG recorded from the forearm of a human volunteer using pencil–paper on-skin sensor and conventional Ag/AgCl gel electrodes (**B**). **C**, A photo of EMG recording with pencil-paper-based sensors.

In addition, high-quality electrophysiological sensors can be directly drawn with pencils on commercial adhesive papers (Aquasol water-soluble paper for this demonstration) without needing Silbione coating to further simplify fabrication processes (**Figure 1.10**). Interestingly, pencil-drawn bioelectronic devices on water-soluble paper are biodegradable and can dissolve in water rapidly (**Figure 1.10**).

The continuous and high-fidelity monitoring of skin temperatures and electrophysiological signals can facilitate an understanding of an individual's evolving physiological state and stress levels (*2, 29*). The pencil-paper on-skin temperature sensor consists of a pencil-drawn graphite conductive trace, with a negative temperature coefficient (-0.36% $°C^{-1}$), calibrated using a thermocouple (**Figure 1.11A**). The enabled devices demonstrate fast electrical responses to temperature changes and can work well in the physiological temperature range (**Figure 1.11B**). The electrical resistance of the temperature sensor decreased by ~1% immediately upon contact with

the forearm of a human volunteer and fully reverted to its initial value upon removal

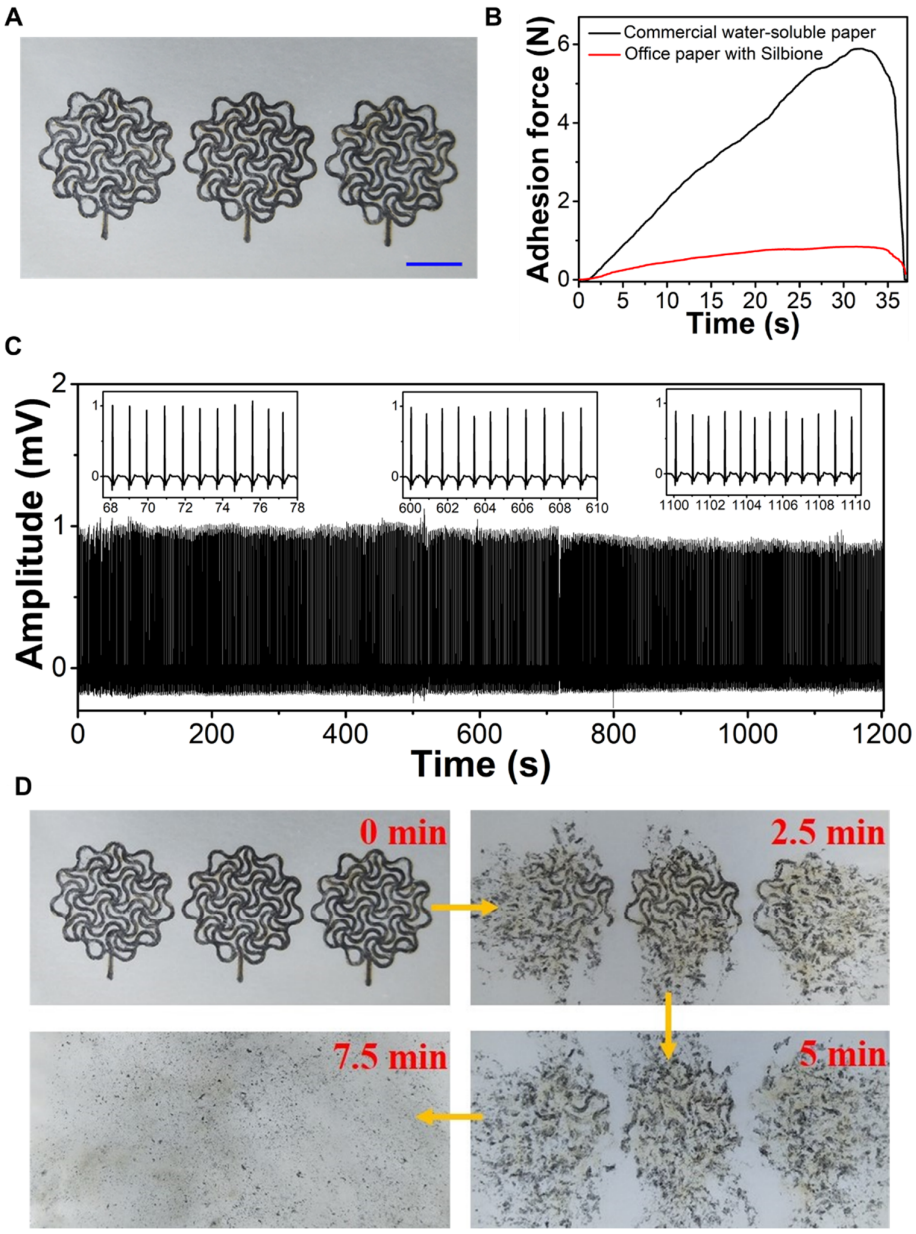


Fig. 1.10. On-skin bioelectronics based on pencil and adhesive water-soluble paper. **A**, A photo of pencil-drawn electrophysiological sensors on adhesive water-soluble papers. Scale bar: 1cm. B, Peel-adhesion tests conducted on the forearm of a human volunteer, indicating adhesive water-soluble paper-based devices is much sticker than office-paper-based devices with Silbione coating. **C**, Continuous ECG recording for 20 min from a human volunteer, indicating high stability. **D**, Rapid dissolution of enabled devices in water because of water-soluble paper substrates. Here, non-degradable pencil-drawn graphite only occupies ~3% by weight of the whole device.

from the volunteer forearm (**Figure 1.11C**). The similar device layout can also be used as the on-skin joule-heating element, which are useful for biomedical treatment (e.g., wound healing). **Figure 1.11D** provides the temperature-time profiles of pencil-paper

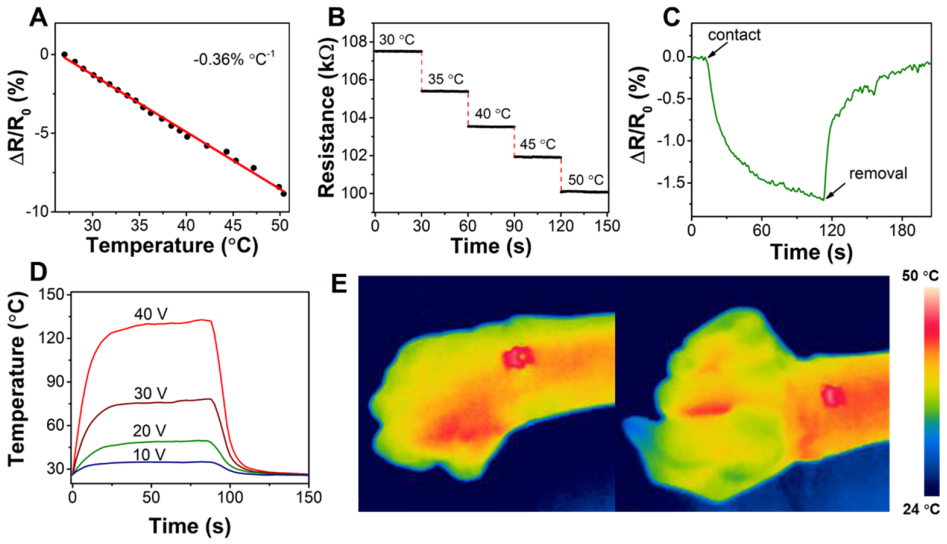


Figure 1.11. A, Calibration plot of the pencil-paper on-skin temperature sensor using a thermocouple in the physiological temperature range. **B**, Dynamic electrical responses of the pencil–paper on-skin temperature sensor on a hotplate with various fixed temperatures and upon contact and removal from the human skin (**C**). **D**, Temperature-time profiles of the pencil-paper on-skin joule-heating element with applied voltages of 10, 20, 30, and 40 V. **E**, Infrared thermal camera images of the pencil–paper on-skin joule-heating element laminated on the wrist of a human volunteer with an applied voltage of 15 V.

on-skin joule-heating elements with various applied voltages. The temperature exhibits sharp increase from room temperature to ~125 ℃ within 30 s when 40 V voltage was applied owing to the graphite's high thermal conductivity. **Figure 1.11 E** demonstrates that the enabled devices can maintain stable thermal stimulations even when the human wrist is flexed and extended. Furthermore, **Figure 1.12** demonstrates that pencil-drawn joule heaters on papers can serve the basis to enable electrothermally triggered reversible assembly, which can open new research and application avenues

of pencil-on-paper methods in reconfigurable and responsive devices, 3D functional devices and soft robotics (*30*).

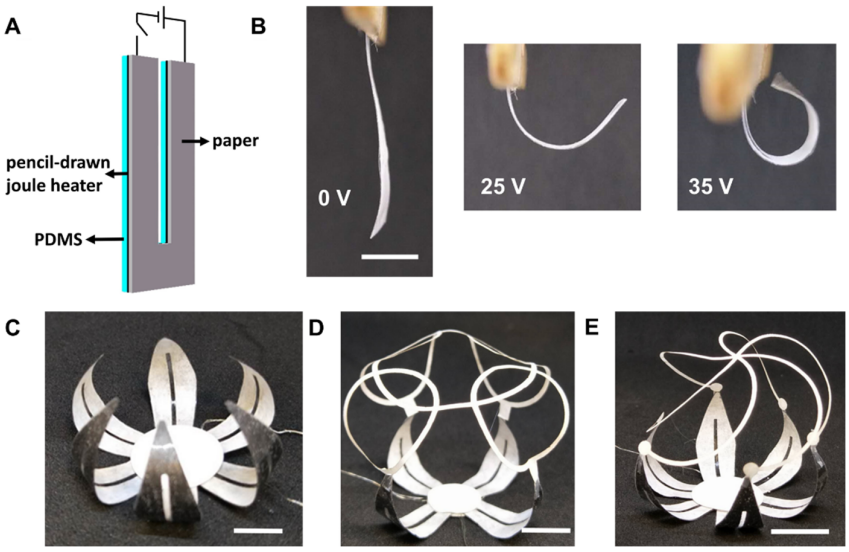


Figure 1.12. Pencil-paper-enabled reconfigurable assembly. **A,** Schematic illustration of pencil-paper-based electrothermal soft actuators, consisting of paper, pencil-drawn joule heaters and polydimethylsiloxane (PDMS). Upon applying an actuation voltage, joule heaters introduce temperature differences via joule heating. The stress caused by the significant difference in thermal expansion between paper and PDMS can induce bending deformations of actuators toward the paper side (**B**). A variety of 3D structures, such as flow-like structures (**C**) rings-table-like structures (**D**) and cage-like structures (**E**) can be reversibly assembled with pencil-paper-based soft actuators. Scale bars: 1 cm.

1.5 Monitoring of cerebral activities via real-time EEG recording using pencil-paper based biophysical sensors

Continuous monitoring of cerebral activities via high-fidelity, real-time electroencephalogram (EEG) recording is of critical importance for studying cognitive behaviors and can also provide insights into various neurological disorders and human fatigue (*32-34*). Cerebral activities can be divided into five frequency bands: delta wave (0-4 Hz), theta wave (4-8 Hz), alpha wave (8-12 Hz), beta wave (12-40 Hz) and gamma wave (>40 Hz) (*35*). Each frequency band is associated with different mental

states. For example, high-frequency, low-amplitude beta waves are often observed during intensive, complex, attentional mental states (*36*). Pencil-paper on-skin electrophysiological sensors can be used to monitor cerebral activities via real-time EEG recording when human subjects engaged in different mental states (**Figure 1.13A**). During the testing, the subject was asked to first close eyes, then open eyes and maintain a twilight state (i.e., dreamy state without awareness of the surroundings), and finally do complex math calculations. Each mental state was maintained for 90 s

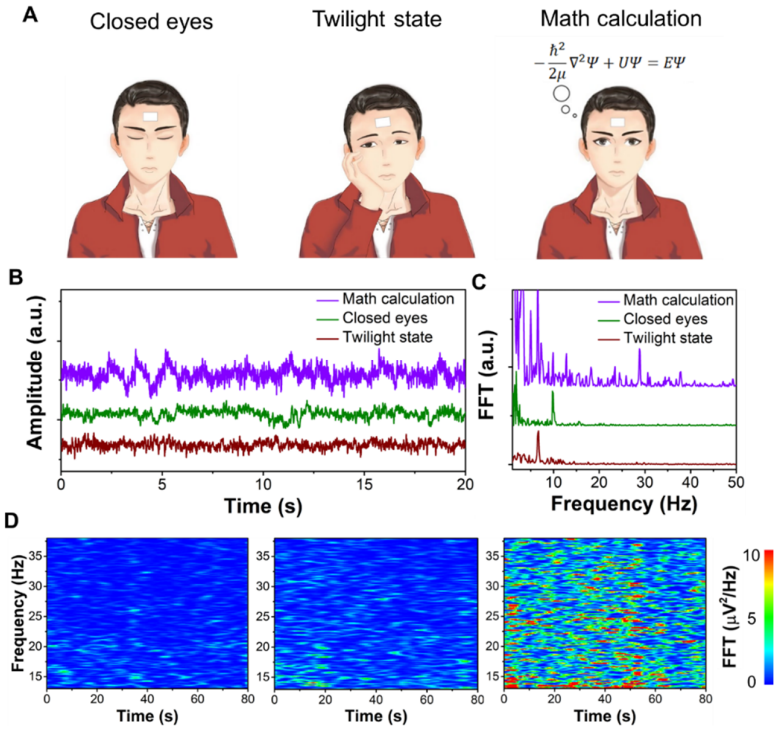


Figure 1.13. Monitoring of cerebral activities via real-time EEG recording. **A**, Schematics and recorded EEG signals (**B**) using pencil–paper on-skin electrophysiological sensors when a human volunteer engaged in three mental states. **C**, FFT-processed frequency distributions of the EEG signals in B. **D**, Time–frequency spectrograms of the EEG signals within beta band (13-38 Hz) during three mental states (Left: closed eyes; Middle: twilight state; Right: math calculation), showing significantly higher signal intensities during math calculation.

and there was a 5-minute break between each state. The recorded EEG signals reveal intense high-frequency cerebral activities during math calculation and strong low-

frequency cerebral activities during closed eyes and twilight state (**Figure 1.13B**). Fast Fourier transform (FFT) was further applied to analyze the recorded EEG signals (**Figure 1.13C**), indicating clear alpha wave (~10 Hz) for closed eyes, theta wave (~6.5 Hz) for twilight state, and beta wave (~28 Hz) for math calculation. The time-frequency spectrograms of recorded EEG signals show clear differences in signal intensities during three mental states (**Figure 1.13D**).

1.6 Characterization and on-body evaluation of pencil-paper-based on-skin biochemical sensors

In-situ perspiration biochemical analysis, together with real-time measurement of biophysical signals, can provide a dynamic and complete picture of human health states (*4, 7, 37*). As proof-of-concept examples, we have developed pencil-paper-based sweat pH, UA and glucose sensors (Fig. 4 and *SI Appendix*, Figs. S20-S25). **Figure 1.14** provides the schematic illustrations and working mechanisms of pencil-paper-based on-skin biochemical sweat sensors.

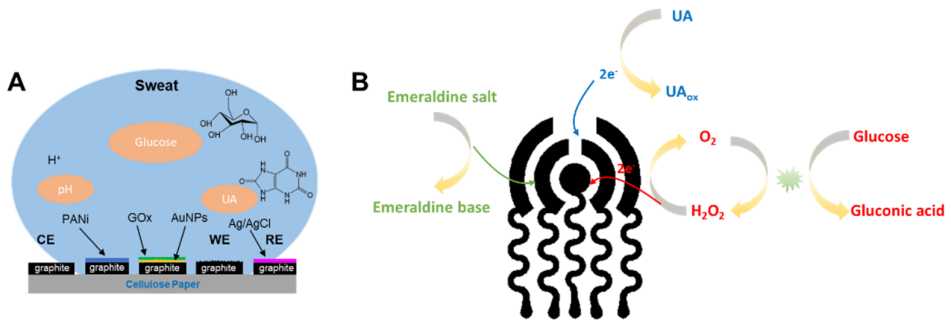


Figure 1.14. A, Schematic illustrations of pencil-paper-based sweat biochemical sensors for in-situ measurement of pH, UA and glucose in sweat. CE: counter electrode; WE: working electrode; RE: reference electrode; AuNPs: gold nanoparticles; GOx: glucose oxidase; PANi: polyaniline. **B**, Schematic illustrations of the working mechanisms of pencil-paper-based pH, uric acid and glucose sensors.

The pH sensors consist of polyaniline (PANi)-coated pencil-drawn graphite

working electrodes and Ag/AgCl ink-coated pencil-drawn graphite reference electrodes, which are used to record the dynamic responses of open-circuit potentials (OCP) at different pH levels. The pH sensors are calibrated in standard buffer solutions and exhibit stable signals from pH 3 to pH 10 (**Figure 1.15A**). The enabled pH sensors are reliable over continuous use at different pH levels and have an average sensitivity of 35 mV/decade (**Figure 1.15B**). Additionally, the pH sensor exhibits reproducible and stable performances as shown in **Figure 1.15C** and **D**.

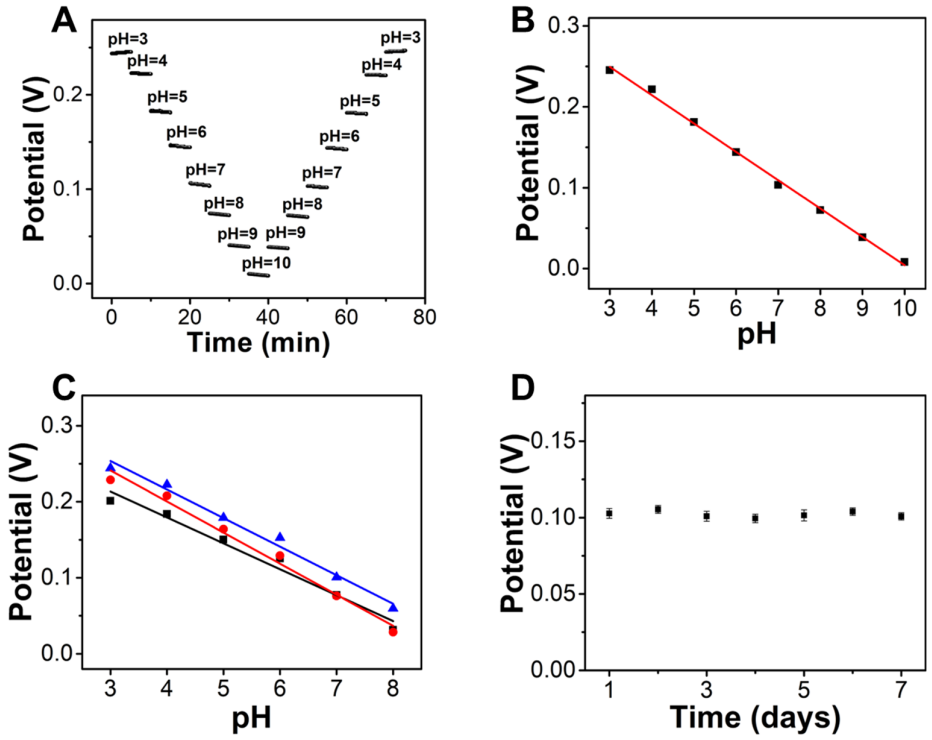


Figure 1.15. The performances of pencil-based pH sensor**. A**, Dynamic open-circuit potential responses to pH variations. **B**, Calibration plot, reproducibility (**C**) and long-term stability (**D**) of pencil-paper-based pH sensors.

The UA sensors consist of working, reference and counter electrodes, which can be used to measure UA concentrations with the differential pulse voltammetry (DPV) method. The current peaks of the UA sensors in DPV signals are attributed to the selective oxidation of UA at ~0.3 V (**Figure 1.16A**). The pencil-paper-based UA

sensor exhibits a good linear relationship with a high sensitivity of ~21.9 nA μM^{-1} in the range of 0-600 µM (**Figure 1.16B**) and high selectivity over other interferential sweat analytes (**Figure 1.16C**), including glucose (Glu), lactate (LA), and ascorbic acid (AA). Additionally, the reproductivity, long-term stability and effects of physiological pH and temperature variations on UA sensors are also evaluated as shown in **Figure 1.16D-G.**

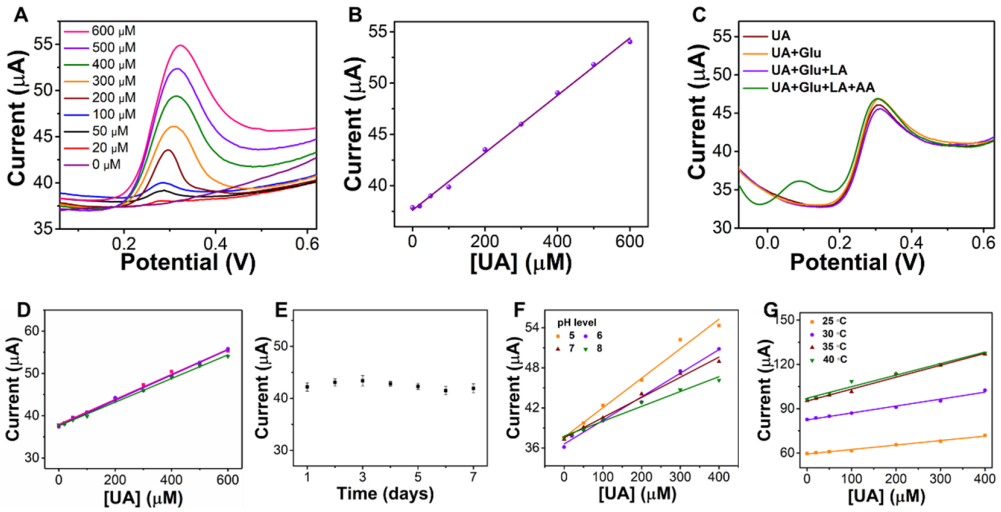


Figure 1.16. The performances of pencil-based UA sensors**. A**, Dynamic current responses to UA variations. **B**, Calibration plot, selectivity (**C**), reproducibility (**D**) and long-term stability (**E**) and the dependance of pencil-paper-based pH sensors on pH (**F**) and temperature(**G**).

The amperometric glucose sensor consists of pencil-drawn graphite working electrodes functionalized with gold nanoparticles (AuNPs), Prussian blue and glucose oxidase (GOx), and Ag/AgCl ink-coated pencil-drawn graphite reference electrodes. The glucose sensors indicate a dynamic current response over the glucose concentration range of 0-90 and 90-600 µM, showing linear relationships between current and glucose concentration with the sensitivities of 1.64 and 3.04 nA μM^{-1}, respectively (**Figure 1.17A-C**). The enabled glucose sensor exhibits negligible signal variations with the addition of a variety of interferential biomarkers (AA, LA, UA),

demonstrating a good selectivity (**Figure 1.17D**). Besides, the glucose sensors also present good reproductivity (**Figure 1.17E**), long-term stability (**Figure 1.17F**) and effects the effects of physiological pH and temperature variations on glucose and UA sensors were investigated and provided in **Figure 1.17G** and **H**.

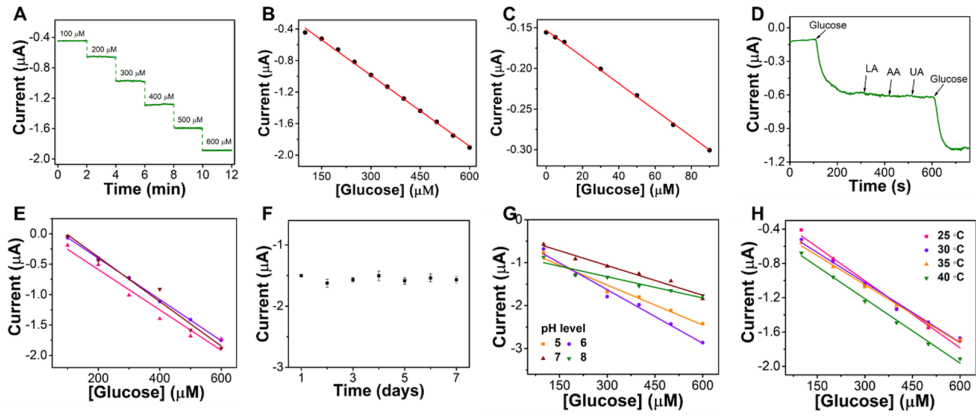


Figure 1.17. The performances of pencil-based glucsoe sensor**. A**, Dynamic open-circuit potential responses to pH variations. **B-C**, Calibration plot , selectivity (**D**), reproducibility (**E**) and long-term stability (**F**) and the dependance of pencil-paper-based pH sensors on pH (**G**) and temperature(**H**).

To further demonstrate the capability of pencil-paper-based sweat sensors, we laminated the devices onto the forehead of one volunteer for real-time perspiration analysis. Also, the raw sweat samples were collected and analyzed using conventional methods. Here, glucose, pH and UA were analyzed with high-performance liquid chromatography, a commercial pH meter, and commercial colorimetric assay kits (*38*), respectively. As shown in **Figure 1.18A**, the data measured with pencil-paper-based sweat sensors from human bodies after heavy perspirations match well with the results obtained using these conventional approaches. Continuous on-body monitoring of UA concentrations before and after a purine-rich diet (300 g of canned sardines for this study) over a 9-hour period is provided in **Figure 1.18B**, further demonstrating the capability of pencil-paper-based sweat biochemical sensors for continuous, in-situ perspiration analysis.

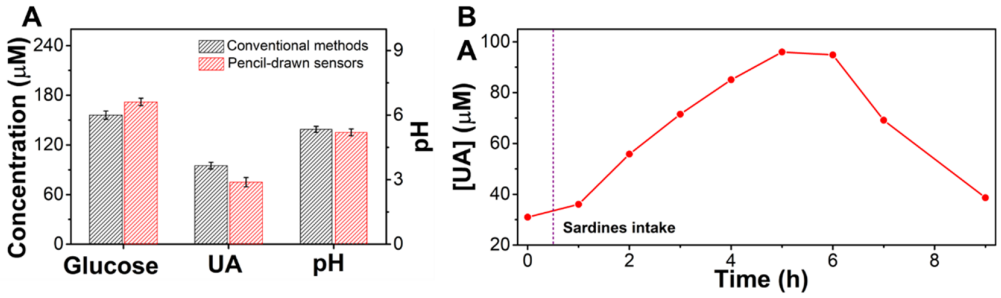


Figure 1.18. A, Comparisons of the data measured with pencil–paper-based biochemical sensors and the results obtained with the conventional methods. **B**, Dynamic change of the UA concentrations, recorded by pencil-paper-based UA sensors, before and after a purine-rich diet over a 9-h period.

1.7 Conclusion

In summary, we report the fabrication and evaluation of a rich variety of pencil-paper-based skin-interfaced bioelectronic devices, ranging from biophysical sensors and sweat biochemical sensors to thermal stimulators. The enabled devices can record a broad spectrum of vital physiological signals from human bodies in a high-fidelity and continuous manner, generate sustained electricity from ambient humidity, and deliver on-skin physical (thermal stimulations) and chemical (transdermal drug delivery) interventions in a programmed manner. Also, pencil-paper-based antennas, 2D and 3D circuits with commercial LEDs and batteries, biodegradable devices, and reconfigurable assembly are explored. These comprehensive demonstrations in emerging on-skin wearables not only will grant this ancient and ordinary pair of tools (i.e., pencils and papers) with new vigor and vitality, but also can broaden the impacts of skin-interfaced human health monitoring and interventions in general. It is worth noting that pencil-paper-based methods cannot achieve as high patterning resolutions as other advanced fabrication techniques (such as photolithography and solution printing) but can work as valuable complements to the state-of-the-art fabrication methods of on-skin electronic devices. For example, pencil-paper-based on-skin

devices can serve as propaganda and inspirational materials for education and training purposes, and can find wide applications in low-resource environments and home-centered personalized healthcare owing to their low-cost resources, handy operation, time-saving fabrication, and abundant potential designs.

1.8 Materials and methods

Materials and regents. Potassium ferricyanide [$K_3Fe(CN)_6$], potassium chloride (KCl), gold chloride trihydrate ($HAuCl_4$), polyaniline, potassium phosphate dibasic (K_2HPO_4), potassium phosphate monobasic (KH_2PO_4), chitosan, uric acid, ascorbic acid, glucose, glucose oxidase, and acetic acid were purchased from Sigma-Aldrich. Iron chloride hexahydrate ($FeCl_3 \cdot 6H_2O$), hydrochloric acid (HCl), sulfuric acid (H_2SO_4), lactic acid (LA) and dimethylformamide (DMF) were purchased from Fisher Scientific. Silbione RT Gel 4717 A/B (Silbione) was received from Elkem Silicones. All chemicals were used as received.

Fabrication of pencil-paper-based biophysical and biochemical sensors. The biophysical sensors were directly drawn on commonly used office-copy papers (DPS; Staples Inc.) using a 9B sketching pencil (Staedtler Mars Lumograph; Pencil Things). Silbione solutions (~70 mg ml^{-1} in hexane) were spray-coated onto the non-device covered regions of the paper using a commercial airbrush (G222, Master Airbrush) to improve the stickiness. To fabricate the pencil-paper-based sweat biochemical sensors, graphite electrodes were first drawn onto commonly used office-copy papers using a 9B sketching pencil (The Fine Touch; Hobby Lobby) as the basis electrodes. For the UA sensors, the pencil-drawn graphite working electrodes were treated with CO_2 laser (VLS2.30 universal laser system) to improve electrochemical activities. Here, the setting was fixed at 10% of the maximum power, 6% of the maximum scanning speed, and raster mode. And pristine pencil-drawn graphite electrodes were used as counter

electrodes without further treatment. To prepare the pH sensors, around ~50 µl of the polyaniline base solution (20 mg ml^{-1}) was drop-casted onto the pencil-drawn graphite electrodes as the working electrodes. Subsequently, the working electrodes were treated with 1.0 M HCl for 15 min to convert polyaniline base into polyaniline emeraldine salt to improve the electrical conductivity and stability. For the fabrication of the glucose sensors, the pencil-drawn graphite working electrodes were first deposited with AuNPs using $HAuCl_4$ in H_2SO_4 as precursor materials with the chronoamperometry method. Next, Prussian blue was deposited on the AuNPs-decorated pencil-drawn graphite electrodes through the cyclic voltammetry in an aqueous solution including 2.5 mM $K_3Fe(CN)_6$, 2.5 mM $FeCl_3$, 100 mM KCl, and 100 mM HCl. The potential was swept from 0 to 0.5 V (vs. Ag/AgCl) with a scan rate of 20 mV s^{-1}. Finally, the addition of the glucose oxidase and chitosan solution (20 µl) completed the fabrication process. Here, the solution was prepared by mixing the glucose oxidase solution (10 mg ml^{-1} in 0.1 M phosphate buffer solution, pH 7.2) and chitosan solution (1% chitosan in 2% acetic acid) at a volume ratio of 1:1. Besides, the reference electrodes were prepared by drop-casting Ag/AgCl inks (ALS Co., Ltd) onto the pencil-drawn graphite electrodes, which were dried at 120 ℃ for 5 min. Also, Silbione solutions (~70 mg ml^{-1} in hexane) were spray-coated onto the non-device covered regions of the paper to improve the stickiness. To ensure reproducibility and reliability, we used stencil masks, prepared by commercial desktop paper cutting machines, to guide pencil drawing and Silbione coating on flat office papers during the device fabrication, and then attached the obtained devices on human bodies for signal recording. The drawing process was repeated for 15 times to achieve desired electrical conductivity.

Design and fabrication of pencil-paper-based dipole antennas. The pencil-paper

based dipole antenna is designed and optimized with commercial ANSYS HFSS software. In our simulations, we assume that the sheet resistance of this pencil-drawing graphite is 160 ohm sq^{-1} with a thickness of 6 μm. Wave port is applied for the antenna excitation and radiation boundary is employed. Based on the optimized parameters, single-layer dipole antennas were directly drawn on commonly used office-copy papers (DPS; Staples Inc.) using a 9B sketching pencil (Staedtler Mars Lumograph; Pencil Things). The drawing process was repeated for 15 times to achieve desired electrical conductivity (~160 ohm sq^{-1}). Afterward, to fabricate multilayer structure, double side tape is utilized to bond each antenna layer together followed by the Sub-Miniature Version A (SMA) connection through silver paste.

Characterizations and measurements. SEM images were taken with a FEI Quanta 600 FEG Environmental SEM. Raman spectra were collected with a Renishaw Raman microscope. XPS data were recorded on an ESCALAB 250Xi photoelectron spectrometer (Thermo Fisher Scientific) with Al Kα (1486.6 eV). EDS data were taken by iXRF EDS Elemental Analysis System. Mechanical properties were measured with a dynamic tensile tester (Mark-10). Skin adhesion was measured with a force gauge (M5-05). The open-circuit voltage and short-circuit current of the energy harvester were measured by a digital sourcemeter (2604B, Keithley Instruments Inc.). Water vapor transmission rate was evaluated based on ASTM96 at 35 °C. On-skin temperature sensors were calibrated using thermocouples (SA1-K, OMEGA Engineering) with a thermometer (HH309A, OMEGA Engineering). Infrared images were captured with a commercial thermal camera (FLIR E6). The antennas' reflection coefficient (S_{11}) measurements were conducted using Vector Network Analyzer (VNA) with the pre-calibrated range from 1 to 6 GHz. The radiation pattern was measured in the anechoic chamber room with our under-test antenna acting as transmitter (T_x),

which transmits a fixed 20 dBm radio wave generated by signal generator. A broadband horn antenna with 16.5 dBi realized gain at 2.6 GHz is used as receiver (R_x) and the data is recorded by spectrum analyzer. Finally, the radiation pattern can be calculated based on the Friis equation.

Electrophysiological signals were recorded with PowerLab T26 (AD Instruments). The resistances and impedances were measured with LCR Meter (IM3523, HIOKI). Electrochemical characterizations were conducted on an electrochemical station (CHI660E, CH Instruments, Inc.). For on-body measurement of sweat biomarkers, a water-absorbent thin rayon pad was placed between skins and sensors to collect sweat. The pH, UA and glucose in sweat were measured using a pH meter (pH-22, Horiba LAQUAtwin), Uric Acid Assay Kits (QuantiChrom, BioAssay Systems) (RS2), and a Waters Acquity HPLC system coupled to a Bruker Impact II quadrupole time-of-flight mass spectrometer (QTOFMS), respectively. The results were compared to the data obtained with pencil-paper-based sweat biochemical sensors. Continuous recording of UA concentration variations was conducted before and after a purine-rich diet (300 g of canned sardines). Before data collection, pencil-paper enabled UA sensors were calibrated using the DPV method. The forehead of the subject was cleaned with alcohol swabs and then pencil-paper sweat sensors were laminated. Data collection was initiated after 5 min of outdoor running. In the research, anisotropic conductive films (ACF) were used for wiring the on-skin devices to the external data acquisition equipment. The diffusion of dyes into pig skins was imaged with a Nikon FN1 epifluorescence microscope equipped with a CoolSNAP-EZ CCD-camera. The pig skin was procured from a local slaughterhouse, which is exempt from approval by the Institutional Animal Care and Use Committee at University of Missouri-Columbia.

1.9 References

1.Y. Xu, G. Zhao, L. Zhu, Q. Fei, Z. Zhang, Z. Chen, F. An, Y. Chen, Y. Ling, P. Guo, S. Ding, G. Huang, P.Y. Chen, Q. Cao, Z. Yan, Pencil-paper on-skin electronics. *Proc. Natl.Acad. Sci. U. S. A.* **117**, 18292-18301 (2020).

2. T.R. Ray, J. Choi, A.J. Bandodkar, S. Krishnan, P. Gutruf, L.M. Tian, R. Ghaffari, J.A. Rogers, Bio-Integrated Wearable Systems: A Comprehensive Review. *Chem. Rev.* **119** , 5461-5533 (2019).

3. N. Matsuhisa, X.D. Chen, Z.A. Bao, T. Someya, T., Materials and structural designs of stretchable conductors. *Chem. Soc. Rev.* **48** , 2946-2966 (2019).

4. M. Bariya, H.Y.Y. Nyein, A. Javey, Wearable sweat sensors. *Nat. Electron.* **1** , 160-171(2018).

5. S.X. Yang, Y.C. Chen, L. Nicolini, P. Pasupathy, J. Sacks, B. Su, R. Yang, D. Sanchez, Y.F. Chang, P.L. Wang, D. Schnyer, D. Neikirk, N.S. Lu, "Cut-and-Paste" Manufacture of Multiparametric Epidermal Sensor Systems. *Adv. Mater.* **27** (41), 6423-6430 (2015).

6. Sim, Z.Y. Rao, F. Ershad, C.J. Yu, Rubbery Electronics Fully Made of Stretchable Elastomeric Electronic Materials. *Adv. Mater.* **32**, 22 (2020).

7. J. Kim, A.S. Campbell, B.E.F. de Avila, J. Wang, Wearable biosensors for healthcare monitoring. *Nat. Biotechnol.* **37**, 389-406 (2019).

8. W. Gao, H. Ota, D. Kiriya, K. Takei, A. Javey, Flexible Electronics toward Wearable Sensing. *Accounts Chem. Res.* **52**, 523-533 (2019).

9. D.C. Kim, H.J. Shim, W. Lee, J.H. Koo, D.H. Kim, Material-Based Approaches for the Fabrication of Stretchable Electronics. *Adv. Mater.* **32** , 29 (2020).

10. T. Someya, M. Amagai, Toward a new generation of smart skins. *Nature Biotechnology* **37**, 382-388 (2019).

11. T. Someya, Z.N. Bao, G.G, The rise of plastic bioelectronics. *Nature* **540** , 379-385 (2016).

12. F. Molina-Lopez, T.Z. Gao, U. Kraft, C. Zhu, T. Öhlund, R. Pfattner, V.R. Feig, Y. Kim, S. Wang, Y. Yun, Z. Bao, Inkjet-printed stretchable and low voltage synaptic transistor array. *Nat. Commun.* **10**, 10 (2019).

13. N. Matsuhisa, D. Inoue, P. Zalar, H. Jin, Y. Matsuba, A. Itoh, T. Yokota, D.

Hashizume, T. Someya, Printable elastic conductors by in situ formation of silver nanoparticles from silver flakes. *Nat. Mater.* **16**, 834-840 (2017).

14. Z.N. Zou, C.P. Zhu, Y. Li, X.F. Lei, W. Zhang, J.L. Xiao, Rehealable, fully recyclable, and malleable electronic skin enabled by dynamic covalent thermoset nanocomposite. *Sci. Adv.* **4**, 8 (2018).

15. S.K. Kang, J. Koo, Y.K. Lee, J.A. Rogers, Advanced Materials and Devices for Bioresorbable Electronics. *Accounts. Chem. Res.* **51**, 988-998 (2018).

16. D. Tobjörk, R. Österbacka, Paper Electronics. *Adv. Mater.* **23**, 1935-1961 (2011).

17. G.Y. Zheng, L.B. Hu, H. Wu, X. Xie, Y. Cui, Paper supercapacitors by a solvent-free drawing method. *Energ. Environ. Sci.* **4**, 3368-3373 (2011).

18. X.Q. Liao, Q.L. Liao, X.Q. Yan, Q.J. Liang, H.N. Si, M.H. Li, H.L. Wu, S.Y. Cao, Y. Zhang, Flexible and Highly Sensitive Strain Sensors Fabricated by Pencil Drawn for Wearable Monitor. *Adv. Funct. Mater.* **25**, 2395-2401 (2015).

19. L.M. Malard, M.A. Pimenta, G. Dresselhaus, M.S. Dresselhaus, Dresselhaus, M. S., Raman spectroscopy in graphene. *Phys. Rep.-Rev. Sec. Phys. Lett.* **473** , 51-87 (2009).

20. Z.J. Zhang, M.F. Iskander, J.C. Langer, J. Mathews, Dual-band WLAN dipole antenna using an internal matching circuit. *Ieee Transact. on Antennas and Propagat.* **53**, 1813-1818 (2005).

21.] N.J. Kirsch, N.A. Vacirca, E.E. Plowman, T.P. Kurzweg, A.K. Fontecchio, K.R. Dandekar, Ieee In *Optically Transparent Conductive Polymer RFID Meandering Dipole Antenna*, IEEE International Conference on RFID, Orlando, FL, Apr 27-28; Ieee: Orlando, FL; pp 270-274 (2009).

22. G.A. Casula, G. Montisci, G. Mazzarella, A Wideband PET Inkjet-Printed Antenna for UHF RFID. *IEEE Antennas Wirel. Propag. Lett.* **12,** 1400-1403 (2013).

23. A. Sarycheva, A. Polemi, Y.L. Liu, K. Dandekar, B. Anasori, Y. Gogotsi, 2D titanium carbide (MXene) for wireless communication. *Sci. Adv.* **4**, 8 (2018).

24. T.C. Shyu, P.F. Damasceno, P.M. Dodd, A. Lamoureux, L.Z. Xu, M. Shlian, M. Shtein, S.C. Glotzer, N.A. Kotov, A kirigami approach to engineering elasticity in nanocomposites through patterned defects. *Nat. Mater.* **14**, 785 (2015).

25. H.U. Chung, B.H. Kim, J.Y. Lee, J. Lee, Z.Q. Xie, E.M. Ibler, K. Lee, A. Banks, J.Y. Jeong, J. Kim, C. Ogle, D. Grande, Y. Yu, H. Jang, P. Assem, D. Ryu, J.W. Kwak,

M. Namkoong, J.B. Park, Y. Lee, D.H. Kim, A. Ryu, J. Jeong, K. You, B.W. Ji, Z.J. Liu, Q.Z. Huo, X. Feng, Y.J. Deng, Y.S. Xu, K.I. Jang, J. Kim, Y.H. Zhang, R. Ghaffari, C.M. Rand, M. Schau, A. Hamvas, D.E. Weese-Mayer, Y.G. Huang, S.M. Lee, C.H. Lee, N.R. Shanbhag, A.S. Paller, S. Xu, J.A. Rogers, Binodal, wireless epidermal electronic systems with in-sensor analytics for neonatal intensive care. *Science* **363**, 947 (2019).

26. Y.Xu, B. Sun, Y. Ling, Q. Fei, Z. Chen, X. Li, P. Guo, N. Jeon, S. Goswami, Y. Liao, S. Ding, Q.Yu, J. Lin, G. Huang, Z. Yan, Multiscale porous elastomer substrates for multifunctional on-skin electronics with passive-cooling capabilities. *Proc. Natl. Acad. Sci. U. S. A*. **117**, 205-213 (2020).

27. B. Sun, R.McCay, S. Goswami, Y. Xu, C. Zhang, Y. Ling, J. Lin, Z. Yan, Gas-Permeable, Multifunctional On-Skin Electronics Based on Laser-Induced Porous Graphene and Sugar-Templated Elastomer Sponges. *Adv. Mater.* **30**, 8 (2018).

28. A. Miyamoto, S. Lee, N.F. Cooray, S. Lee, M. Mori, N. Matsuhisa, H. Jin, L. Yoda, T. Yokota, A. Itoh, M. Sekino, H. Kawasaki, T. Ebihara, M. Amagai, T. Someya, Inflammation-free, gas-permeable, lightweight, stretchable on-skin electronics with nanomeshes. *Nat. Nanotechnol.* **12**, 907 (2017).

29. D. Kim, N. Lu, R. Ma, Y. Kim, R. Kim, S. Wang, J. Wu, S. Won, H. Tao, A. Islam, K.Yu, T. Kim, R. Chowdhury, M. Ying, L.Xu, M. Li, H. Chung, H. Keum, M. McCormick, P. Liu, Y. Zhang, F. Omenetto, Y. Huang, T. Coleman, J.A Rogers, Epidermal Electronics. *Science* **333**, 838-843 (2011).

30. Y. Ling, W.Pang, X. Li, S. Goswami, Z. Xu, D. Stroman, Y.Liu, Q. Fei, Y. Xu, G. Zhao, B. Sun, J. Xie, G. Huang, Y. Zhang, Z. Yan, Laser-Induced Graphene for Electrothermally Controlled, Mechanically Guided, 3D Assembly and Human-Soft Actuators Interaction. *Adv. Mater.* **32**, 9 (2020).

31. J. Kim, S. Han, S.M. Cho, S. Lee, Y.R. Son, K.J. Lee, W. Kim, T. Park, Y. Lee, M. Oh, D. Choo, J. Jang, Is In *OTFT on plastic substrate for AMOLED driving*, 30th International Congress of Imaging Science (ICIS 06), Rochester, NY, May 07-11; Soc Imaging Science & Technology: Rochester, NY; pp 692 (2006).

32. F. Rosenow, K.M. Klein, H.M. Hamer, Non-invasive EEG evaluation in epilepsy diagnosis. *Expert Rev. Neurother.* **15**, 425-444 (2015).

33. K.G. Jordan, Emergency EEG and continuous EEG monitoring in acute ischemic

stroke. *J. Clin. Neurophysiol.* **21**, 341-352 (2004).

34. G. Borghini, L. Astolfi, G. Vecchiato, D. Mattia, F. Babiloni, Measuring neurophysiological signals in aircraft pilots and car drivers for the assessment of mental workload, fatigue and drowsiness. *Neurosci. Biobehav. Rev.* **44**, 58-75 (2014).

35. N.H. Liu, C.Y. Chiang, H.C. Chu, Recognizing the Degree of Human Attention Using EEG Signals from Mobile Sensors. *Sensors* **13** , 10273-10286 (2013).

36. D.H. Ho, S. Cheon, P. Hong, J.H. Park, J.W. Suk, D.H. Kim, J.T. Han, J.H. Cho, Multifunctional Smart Textronics with Blow-Spun Nonwoven Fabrics. *Adv. Funct.Mater.* **29** , 9 (2019).

37. S. Imani, A.J. Bandodkar, A.M.V. Mohan, R. Kumar, S.F. Yu, J. Wang, P.P. Mercier, A wearable chemical-electrophysiological hybrid biosensing system for real-time health and fitness monitoring. *Nat. Commun.* **7**, 7 (2016).

38. Y.Yang, Y. Song, X. Bo, J. Min, O. Pak, L. Zhu, M. Wang, J. Tu, A. Kogan, H. Zhang, T. Hsiai, Z. Li, W. Gao, A laser-engraved wearable sensor for sensitive detection of uric acid and tyrosine in sweat. *Nat. Biotechnol.* **38**, 217 (2020).

Chapter 2. Laser-Scribed Conductive, Photoactive Transition Metal Oxide on Soft Elastomers for Janus On-Skin Electronics and Soft Actuators

This chapter is copied and reformatted from a paper published in *Science Advances,* 2022, 8, 25, eabp9734 (2020) (*1*).

Abstract: Laser-assisted fabrication of conductive materials on flexible substrates has attracted intense interests due to its simplicity, easy customization, and broad applications. However, it remains challenging to achieve laser scribing of conductive materials on tissue-like soft elastomers, which can serve as the basis to construct bioelectronics and soft actuators. Herein, we report laser scribing of metallic conductive, photoactive transition metal oxide (molybdenum dioxide) on soft elastomers, coated with molybdenum chloride precursors, at ambient conditions. Laser-scribed molybdenum dioxide (LSM) exhibits high electrical conductivity, biocompatibility, chemical stability, and compatibility with magnetic resonance imaging. Also, LSM can be made on various substrates (polyimide, glass, and hair), showing high generality. Furthermore, LSM-based Janus on-skin electronics are developed to record information from human skin, human breath, and environments. Taking advantage of its outstanding photothermal effect, LSM-based soft actuators are developed to build light-driven reconfigurable 3D architectures, reshapable airflow sensors, and smart robotic worms with bioelectronic sensors.

2.1 Introduction

Laser-assisted, mask-free fabrication is emerging as a versatile and powerful technique for the scalable production of conductive materials with customized patterns on flexible substrates (*2-6*). For example, laser-induced graphene (termed as LIG), taking advantage of laser-irradiation-induced, localized, high temperatures to convert carbonaceous materials into porous graphene with arbitrary patterns at ambient conditions, features simple fabrication, easy customization and high electrical conductivity, and has shown promising applications in flexible electronics, soft actuators, artificial throats, energy storage, and others (7-*10*). In spite of recent progresses in laser-assisted fabrication, it remains challenging to enable laser scribing of graphene or other highly conductive materials on tissue-like soft elastomers. For instance, high-quality LIG is usually obtained on rigid polyimide films (PI; Young's modulus: ~2.5 GPa) (*2*), which has a big mechanical mismatch with biological tissues. Soft elastomers indicate tissue-like pliability, high stretchability, and biocompatibility. And their integrations with customized conductive patterns are the ideal building blocks (e.g., conductive traces, basis electrodes) to make various bio-interfaced electronics and soft actuators (*11-13*). While LIG can be transferred from rigid PI mother substrates onto soft elastomer substrates for bio-related applications, the additional transfer-printing process is complicated and tedious (*14*). It is worth noting that laser-assisted fabrication of silicon carbide (SiC) has been recently achieved on soft silicone elastomers (*15, 16*). However, laser-scribed SiC demonstrates a relatively poor electrical conductivity, thereby restricting its broad applications in on-skin electronics and others.

Molybdenum dioxide (MoO_2) is an unusual and attractive transition metal oxide due to its metallic electrical resistivity (8.8×10^{-5} Ω·cm), high chemical stability, high

biocompatibility, and low magnetic susceptibility (*17-19*), which is a fascinating material for bioelectronic applications. Additionally, on account of its high photothermal conversion efficiency (over 60% in the near-infrared region) (*20, 21*), MoO_2 can be adopted for light-driven soft actuators. Presently, MoO_2 is mainly prepared using hydrothermal or calcination methods and is usually used for photothermal therapy, lithium-ion batteries, electrocatalysts, surface-enhanced Raman spectroscopy, and others (*19, 22-24*). Even with these promising properties, the applications of MoO_2 in emerging bioelectronics and soft actuators are still rare, mainly due to the lack of the fabrication technique that can enable simple, scalable, and mask-free fabrication of MoO_2 on tissue-like soft elastomers at ambient conditions.

To fill the aforementioned-gaps in material fabrications, in this article, we first demonstrate laser-assisted, mask-free, scalable scribing of MoO_2 (termed as LSM) on soft elastomers and other substrates at ambient conditions (*10, 11*). In addition, existing on-skin wearables usually have bioelectronic devices patterned on the bottom side that directly touches human skin to record various biosignals. And the studies of developing Janus wearable devices, which have different biosensing functions on the skin-touch side and air-exposed side, are still rare. Herein, we have further developed LSM-based Janus on-skin wearables with different bioelectronic devices patterned on the two sides, which can provide concurrent monitoring of comprehensive information from human skin, human breath, and environments for potential applications in health monitoring and daily-life management. Besides, soft actuators based on laser-induced graphene have been recently achieved, which are usually electrothermally actuated and need conductive wires to connect soft actuators with external power sources (*13*). In this work, we have developed LSM-based, untethered, light-driven soft actuators and

demonstrated their applications in reconfigurable 3D architectures, reshapable wearable airflow sensors, and smart soft robotic worms with bioelectronic sensors.

2.2 Fabrication and characterization of the LSM

The fabrication process of LSM is illustrated in **Figure.2.1**. In brief, the process starts with spray-coating of molybdenum chloride ($MoCl_5$) on supporting substrates, which are annealed at 85°C for 2 min in the air. Next, CO_2 laser irradiation is used to convert the precursors into MoO_2 at ambient conditions by a photothermal process. Here, CO_2 laser centers at 10.6 μm with a range of 927-951 cm^{-1} (*25*). These frequencies can be well absorbed by the precursors. The Hilbert serpentine pattern is used as an illustrative example and the computer-controlled CO_2 laser beam can create arbitrary MoO_2 patterns on substrates coated with precursors. In the end, washing away the precursors, unexposed to the CO_2 laser irradiation, completes the fabrication process.

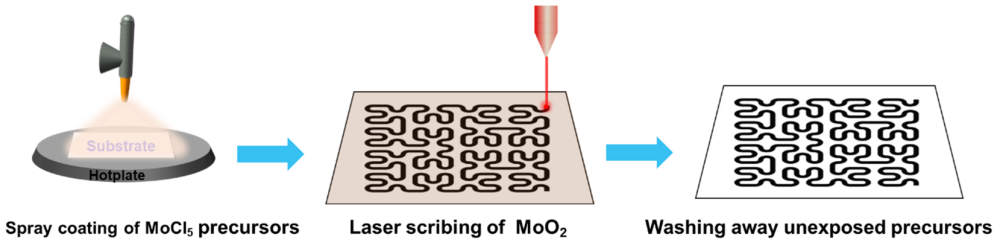


Figure 2.1. Schematic illustration of laser scribing of MoO_2 on supporting substrates.

The phase-separation-synthesized porous poly (styrene-ethylene-butadiene-styrene) (SEBS) is used as the substrate example to illustrate LSM formation because of its ultrasoftness (Young's modulus: ~1.5 MPa) (*26*), high breathability, and self-cooling effect, which is a promising soft supporting substrate for on-skin bioelectronics. **Figure 2.2A**. provides an optical image of a laser-scribed Hilbert serpentine pattern of MoO_2 on porous SEBS. **Figure 2.2B** displays an array of LSM letters of laser-scribed

MoO_2 on porous SEBS, indicating scalability and high reproducibility of the laser-assisted fabrication. The top-view scanning electron microscopy (SEM) image (**Figure 2.2C** demonstrates that LSM exhibits porous structures. The cross-section SEM image (**Figure 2.2D**) and corresponding energy-dispersive X-ray spectroscopy (EDS) element mapping (**Figure 2.2E**) show the interconnected interface of LSM and porous SEBS, and the thickness of LSM is ~50 µm.

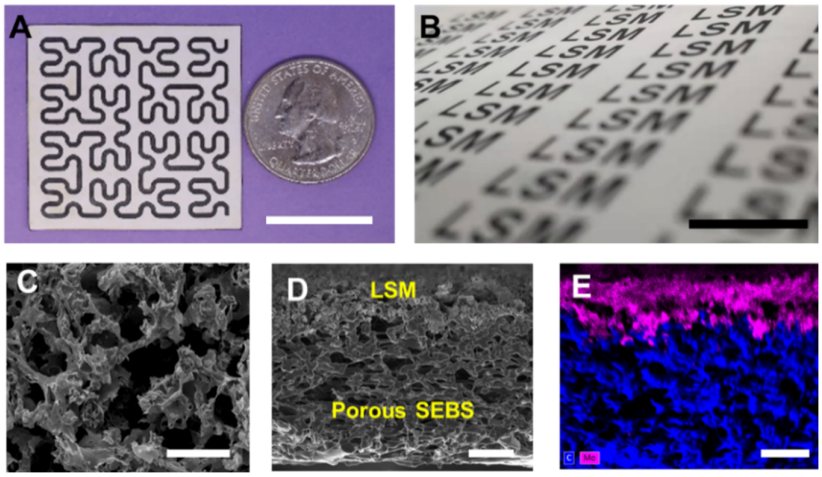


Figure 2.2. Optical image of LSM with the Hilbert pattern **(A)** and an array of LSM letters **(B)** on porous SEBS. Scale bar: 2 cm. **C**, Top-view SEM image and cross-section SEM image (**D**) and cross-section EDS mapping of Mo (pink) and C (blue) elements (**E**) of LSM on porous SEBS. Scale bars in (**C**, **D** and **E)**: 20 µm, 50 µm and 50 µm.

Furthermore, X-Ray Diffraction (XRD) analysis (**Figure 2.3**) shows that LSM can be indexed as the monoclinic-phase MoO_2 (JCPDS. 32-0671) with lattice constants of a = 5.6068 Å, b = 4.8595Å, and c = 5.5373Å (*27*). The inset in **Figure 2.3** illustrates the crystal structure of MoO_2, where six O atoms form octahedron with a Mo atom in the center, occupying half space of the octahedron. All the O atoms in the octahedron are triply shared to form monoclinic MoO_2, which is a distorted rutile structure with two alternative Mo-Mo bond distances, contributing to high electrical conductivity (*17, 24*).

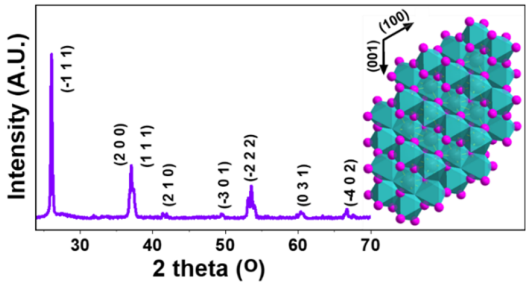


Figure 2.3. XRD pattern of LSM on porous SEBS. Inset: crystal structures of monoclinic MoO_2.

The Raman spectrum of LSM (**Figure 2.4A**) further confirms the formation of MoO_2. The characteristic peaks at ~571 and 744 cm^{-1} arise from Mo-O bond vibration modes, while other fingerprint peaks at ~201, 228, 361, 462 and 495 cm^{-1} can be attributed to phonon vibration modes of MoO_2 (*24*). The high-resolution transmission electron microscopy (HRTEM) image (**Figure 2.4B**) and corresponding fast Fourier transform pattern (**Figure 2.4C**) demonstrate that LSM possesses a high degree of crystallinity. The spacing of the lattice fringe of 0.34 nm and 0.24 nm can be indexed to (-111) and (200) planes of monoclinic MoO_2, respectively.

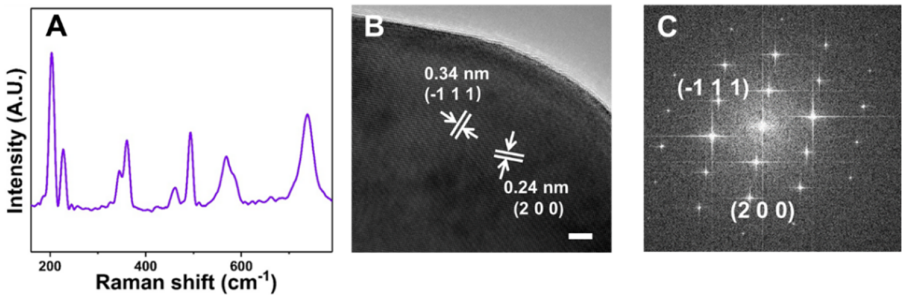


Figure 2.4. A, Raman spectrum of LSM on porous SEBS. (**B**, **C**) HRTEM image and corresponding fast Fourier transform pattern of LSM. Scale bar: 5 nm.

Moreover, as shown in **Figure 2.5A**, a low sheet resistance of ~4.6 Ω sq^{-1} can be achieved on LSM by optimizing the laser scribing power and the amount of $MoCl_5$ precursors coated on porous SEBS, which is well suitable for bioelectronic applications. Also, the laser-assisted fabrication process is highly repeatable and a

standard deviation of 0.4 Ω sq^{-1} is obtained in the sheet resistances of 20 independently prepared LSM samples (**Figure 2.5B**). It is worth noting that laser irradiation on porous SEBS without coating $MoCl_5$ precursors results in the substrate ablation (**Figure 2.5C and D**) instead of the formation of laser-induced graphene, possibly due to its low-melting point and lack of cross-linked aromatic structure (*28*).

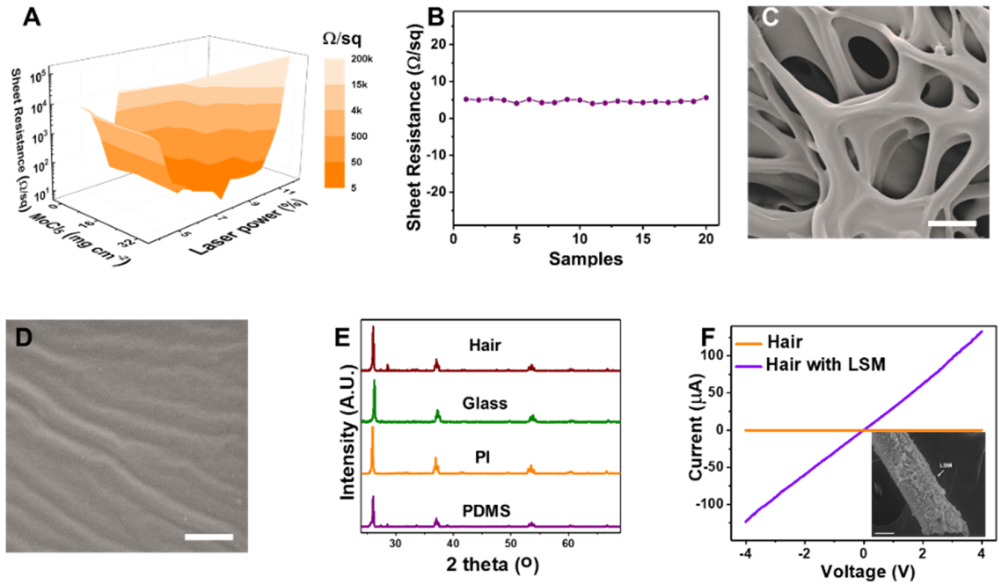


Figure 2.5. A, Variation of sheet resistances of LSM on porous SEBS as a function of the laser-scribing power and the amount of spray-coated $MoCl_5$ precursors. The colour bar indicates distributions of sheet resistances. **B**, Sheet resistances of 20 independently prepared LSM samples on porous SEBS. SEM images of porous SEBS without coating $MoCl_5$ precursors before (**C**) and after (**D**) laser irradiation, indicating the laser ablation instead of graphene formation. Scale bars: 5 μm. **E,** XRD patterns of LSM fabricated on human hair, glass, PI and PDMS. **F**, I-V curves of human hair before and after LSM fabrication. Inset: SEM image of LSM fabricated on human hair. Scale bar: 50 μm.

In addition to porous SEBS, LSM has been made on a variety of substrates, including polydimethylsiloxane (PDMS), PI, glass, and even human hair by using thesimilar procedures (**Figure 2.5E**), indicating high generality of the reported fabrication technique. Inset of **Figure 2.5F** provides an SEM image of LSM formed on human hair. After LSM formation, human hair becomes conductive (**Figure 2.5F**).

Also, as shown in **Figure 2.6A** and **B**, LSM indicates high stability at high temperatures and in both strong acid and strong alkali. In addition, as shown in **Figure 2.6C** and **D**, with precursor coating, laser irradiation has small effects on the underneath polymer substrates during MoO_2 fabrication, possibly due to the strong absorptions of precursor materials in the CO_2 laser wavelengths.

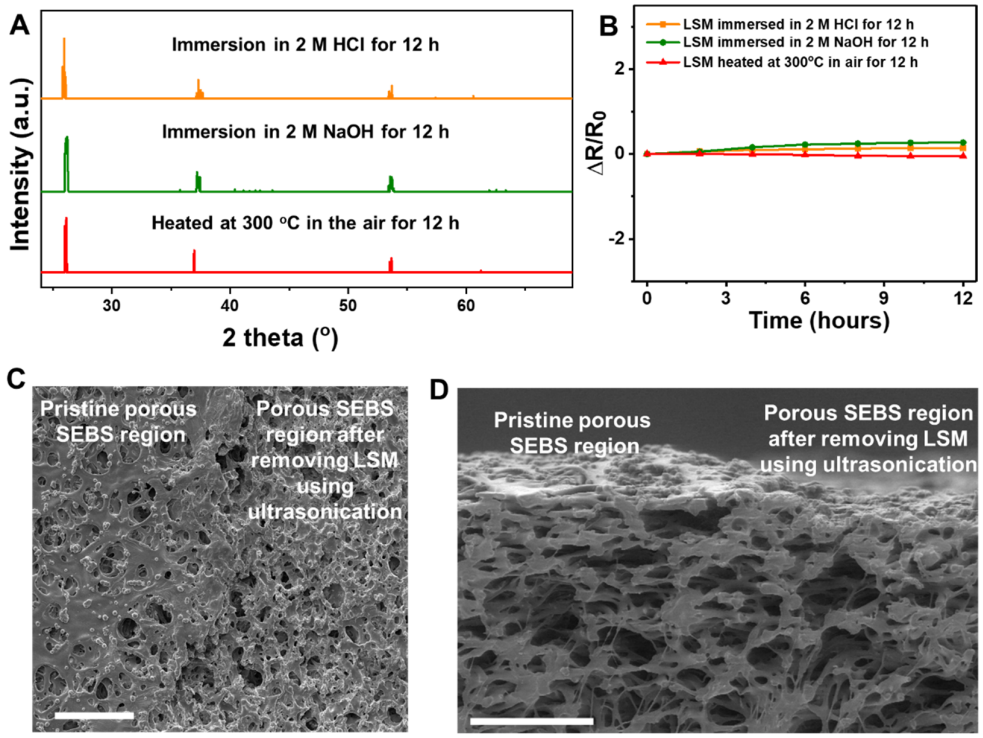


Figure 2.6. XRD patterns (**A**) and relative changes of electrical resistances (**B**) of LSM after being treated with the strong acid (orange), strong alkali (green), and high temperature (red), indicating high chemical stability. For example, after being immersed in strong acid (2 M HCl) for 12 hours, the electrical resistance of LSM only increased ~14%. Top-view (**C**) and cross-section-view (**D**) SEM images of porous SBES after using ultrasonication to remove LSM patterns, indicating laser irradiation has small damages on porous SEBS coated with $MoCl_5$ precursors.

Notably, LSM fabrication has the negligible effect on the breathability (water vapor transmission) of the porous elastomer substrate **Figure 2.7** owing to the porous structures of LSM and well-preserved porous structures of porous SEBS after LSM fabrication (**Figure 2.6C** and **D**).

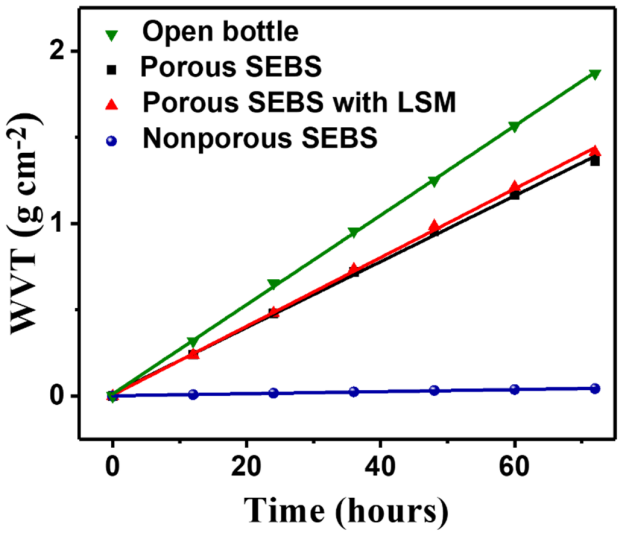


Figure 2.7. Water vapor transmissions (WVT) of open bottle (green), porous SEBS (black), porous SEBS with LSM (red), and nonporous SEBS (blue) as a function of the elapsed time, indicating the negligible changes of water vapor transmission rates after MoO_2 fabrication on porous SEBS.

2.3 Cytotoxicity tests and MRI compatibility characterization of the LSM

In addition, cytotoxicity tests were conducted by incubating three different types of cell lines, including human immortalized epidermal cells (HaCaT), human histiocytic lymphoma cells (U937) and human dermal fibroblasts (HDF-α), on LSM. Here, the obtained data were evaluated for statistical significance using an ordinary two-way ANOVA followed by a post-hoc Tukey's multiple comparison test and the differences were considered significant at $p<0.05$. The relative fluorescence intensity (**Figure 2.8A**) shows that there are no significant differences ($p >0.05$) in cell viability among the cells cultured with LSM and on tissue culture polystyrene (control) on the fifth day. The fluorescence micrographs (**Figure 2.8B**) show that HaCaT cells attach well and spread uniformly on LSM and no visible apoptosis or necrosis are observed, indicating outstanding biocompatibility.

Besides, it is desirable to develop magnetic resonance imaging (MRI)-compatible

bioelectronics (*29, 30*). The unique combination of MRI and bioelectronics can provide comprehensive information of the human psychological state. Here, the magnetic susceptibility of LSM is about -2 ppm (**Figure 2.9A**). The material is usually

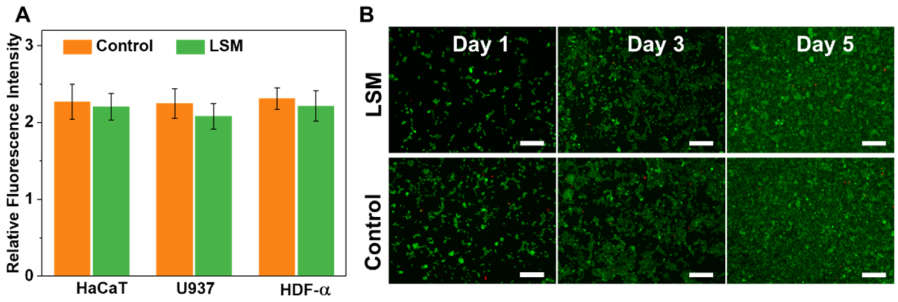


Figure 2.8. A, Relative fluorescence intensity of three cell lines after five-day culturing on the LSM and control sample (tissue culture polystyrene). **B**, Fluorescence images of stained HaCaT cells on the LSM and control sample after one-day, three-day, and five-day culturing. Live and dead cells were stained in green and red, respectively. Scale bars: 50 μm.

considered to be MRI compatible when the absolute value of the magnetic susceptibility difference between the investigated material and water (magnetic susceptibility: -9 ppm) is less than 10 ppm. As shown in **Figure 2.9B**, LSM has better MRI compatibility than several other conductive materials used in bioelectronics [e.g., platinum (Pt), gold (Au), silver (Ag)] (*31*). While copper (Cu) has better MRI compatibility than LSM, Cu can be easily oxidized into copper oxide with high magnetic susceptibility (~17 ppm) (*32*) in the air and biofluids, dampening its promise. Also, a negligible temperature fluctuation was observed on LSM during a 20-min MRI scanning process (**Figure 2.9C**), measured with a fiber optic temperature sensor. To further demonstrate MRI compatibility, LSM was attached on a porcine head (**Figure 2.9D**) for imaging using a 3T clinical MRI scanner. The obtained MRI images show no artifacts or distortion in the LSM vicinity (**Figure 2.9E** and **F** obtained from T1-weighted MPRAGE sequence scans and T2-weighted SPACE sequence scans, respectively), indicating outstanding MRI-compatibility.

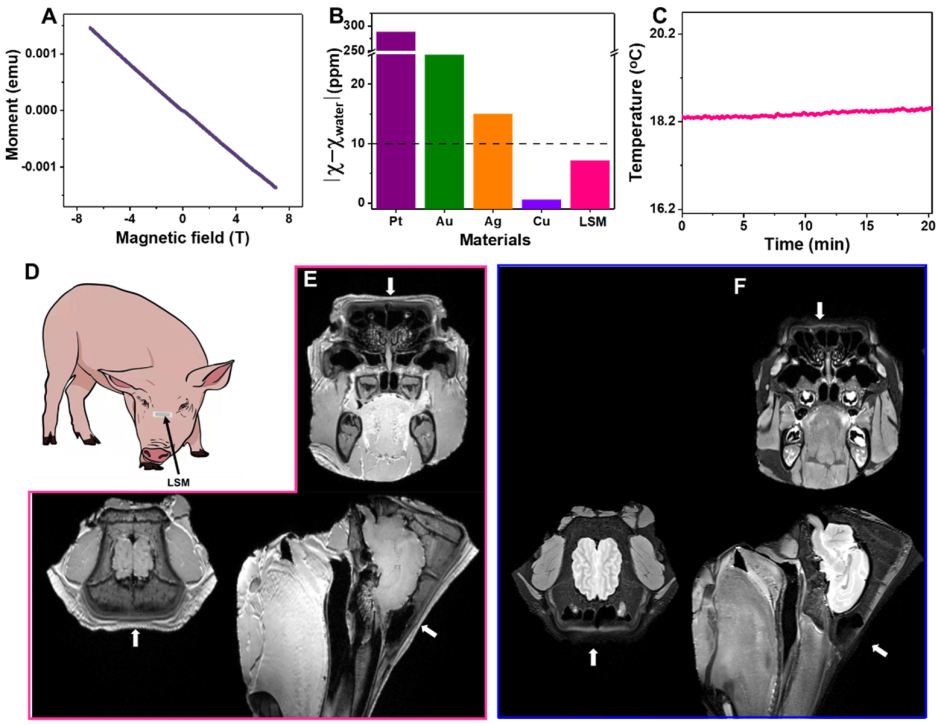


Figure 2.9. A, Magnetic susceptibility of LSM on porous SEBS measured at 300 K under applied magnetic fields of -7 to 7 T. **B**, Absolute values of magnetic susceptibility (χ) differences between water and some conductive materials (LSM, Pt, Au, Ag and Cu) used in bioelectronics. **C**, Temperature changes of LSM during the MRI scanning measured with a fiber optic temperature sensor, showing negligible fluctuation. **D**, Schematic illustration of the location of LSM on the porcine head. **E**, MRI images obtained using T1-weighted MPRAGE sequence scans and T2-weighted SPACE sequence scans (**F**) of a porcine head attached with LSM from the coronal (top right), axial (bottom left) and sagittal (bottom right), showing no distortion or artifact in the LSM vicinity. The arrows indicate the LSM location on the porcine head.

2.4 Electromechanical properties of LSM on porous SEBS with kirigami cuts

To enhance the electromechanical properties of LSM on porous SEBS, we employed kirigami cuts as depicted in **Figure 2.10A** and hot-pressing techniques. The electrical resistance of the LSM pattern on porous SEBS demonstrated no significant change under tensile strains of up to approximately 1000% (**Figure 2.10B**) and

maintain stability even after 1000 stretching cycles at 600% tensile strain (**Figure 2.10C**). Moreover, this design maintains good resistance stability across various bending radii, as shown in **Figure 2.10D**. Additionally, the devices exhibit minimal conductivity changes even after 1000 bending cycles at a 4 mm bending radius (**Figure 2.10E**)

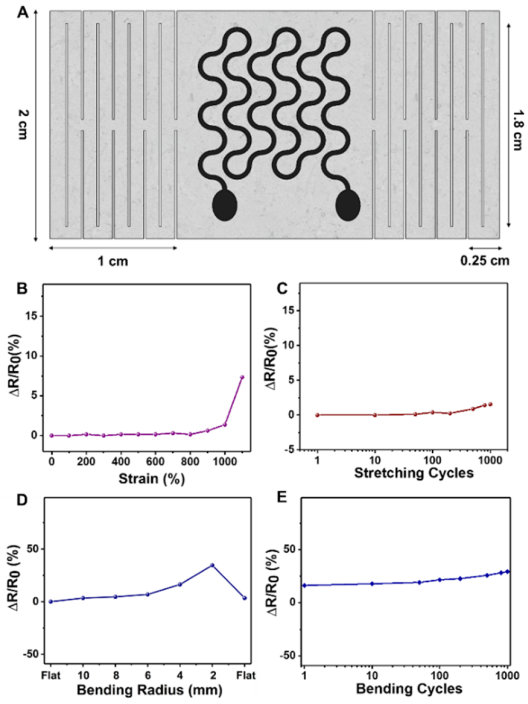


Figure 2.10. Electromechanical properties of LSM on porous SEBS with kirigami cuts. Design layout of LSM on porous SEBS with kirigami cuts (**A**), and the corresponding resistance variations at different tensile strains (**B**) and as a function of stretching cycles under the 600% tensile strain (**C**). Resistance variations of LSM on porous SEBS at different bending radiuses (**D**) and as a function of bending cycles under the 4 mm bending radius (**E**).

2.5 Janus on-skin wearables based on LSM

Emerging on-skin wearable electronics can provide continuous, real-time monitoring of a range of physiological signals from human skin and can find wide

applications in human healthcare, fitness tracking, human-machine interface, and others (*33-35*). Despite the recent considerable progress, on-skin wearables with Janus device layouts, which can not only record multiple biological signals from human skin but also capture useful information from human breath and surrounding environments, are still rare. In this section, we have demonstrated the Janus on-skin wearables based on LSM patterned on porous SEBS (**Figure 2.11**).

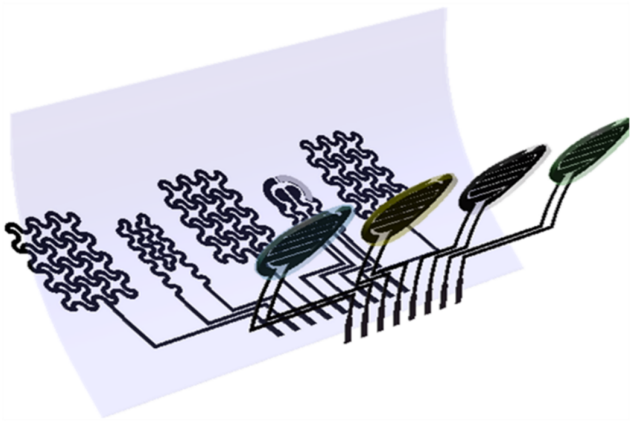


Figure 2.11. Exploded view of the Janus on-skin wearable based on LSM patterned on porous SEBS.

The top side (**Figure 2.12A** and **C**) of the Janus wearable is exposed to the air and has the alcohol gas sensor, humidity sensor, ultraviolet (UV) sensor, and ammonia (NH_3) gas sensor, consisting of LSM interdigital electrodes coated with tungsten diselenide (WSe_2) nanoflakes, graphene oxides (GO), zinc oxide (ZnO) nanowires, and p-toluene sulfonate hexahydrate doped polyaniline (PTS-PANI), respectively. The bottom side of the Janus wearable (**Figure 2.12B** and **D**) directly touches human skin and has the electrophysiological sensor, temperature sensor, and sweat biochemical sensor. The electrophysiological sensor consists of LSM reference, ground and measurement electrodes, which can monitor electrocardiograms (ECG), electroencephalograms (EEG) and electromyograms (EMG). The temperature sensor consists of an LSM conductive trace and can measure the body temperature. The sweat

biochemical sensor consists of the LSM counter electrode, LSM working electrode (coated with carbon inks), LSM working electrode (coated with carbon inks, Au nanoparticles, Prussian blue, and glucose oxidase), and LSM reference electrode [coated with silver/silver chloride (Ag/AgCl)], and can concurrently measure glucose,

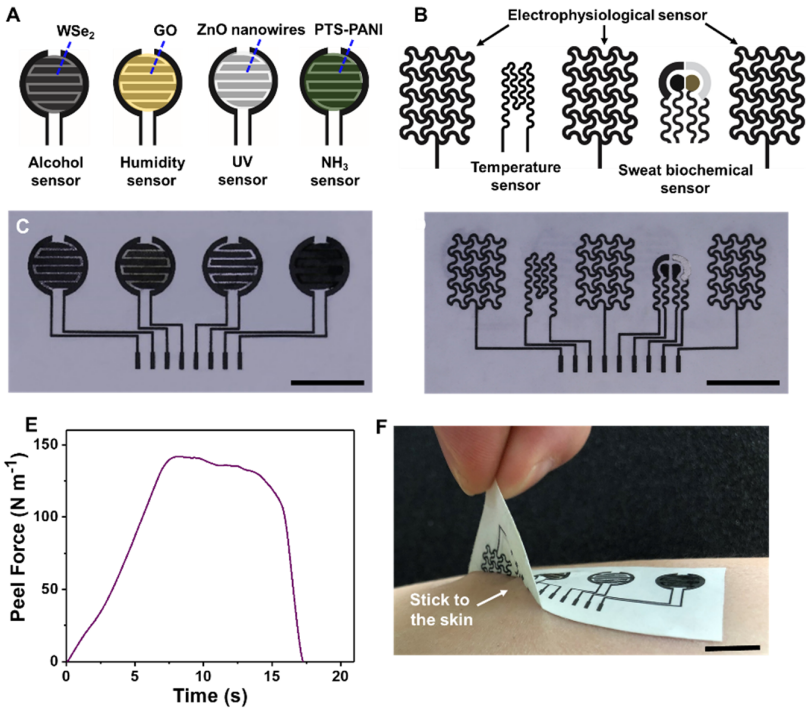


Figure 2.12. Schematic illustration of bioelectronic devices on the top side (**A**) and the corresponding optical image (**C**). Schematic illustration of bioelectronic devices on the top side (**B**) and the corresponding optical image (**D**). **E**, peeling tests of the adhesion from the forearm of a human volunteer and **F**, Photograph showing the good stickiness between the Janus wearable and skin. Scale bar:0.5 cm for **B**, **D** and **F.**

uric acid (UA) and caffeine (CAF) from human sweat. Besides, gelatin-dopamine-based adhesives are coated on porous SEBS to improve the device stickiness and enhance the conformal contact between the Janus wearable and skin with an adhesion force of ~140 N m^{-1} (**Figure 2.12E** and **F**).

Here, the fabricated LSM-based devices can monitor a rich variety of health-related

biophysical and biochemical signals from human skins and provide programmed thermal and electrical stimulations. In specific, the LSM-based temperature sensor exhibits a positive temperature coefficient of resistance (~0.72% $^{o}C^{-1}$) and can precisely measure dynamic skin temperature changes induced by hot blowing (**Figure 2.13A-C**). The same device can be used as a joule heater by applying voltages on the LSM conductive trace, which operates well on the human wrist at the flexed and extended states (**Figure 2.13D** and **E**).

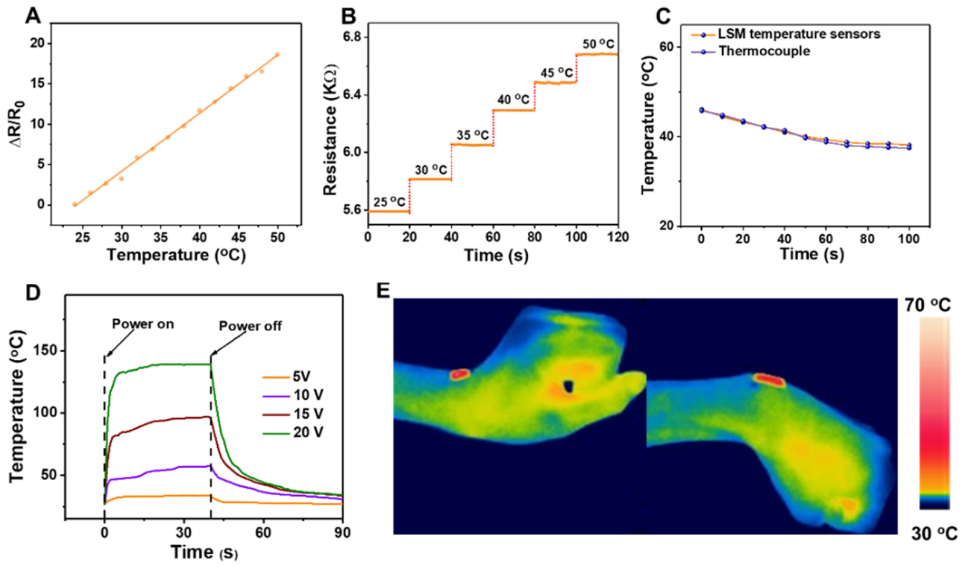


Figure 2.13. Characterizations and on-body evaluations of LSM-based wearable temperature sensors and joule heaters. **A**, Calibration plot of the LSM-based temperature sensor in the physiological temperature range, which was calibrated with a commercial thermocouple. Here, R^2 is 0.996 for the line fit. **B**, Dynamic resistance responses of the LSM-based temperature sensor on a hotplate with the stepwise changed temperatures. **C**, Skin temperature changes after applying a hot pad, which were recorded with LSM-based temperature sensors and a commercial thermocouple, showing good alignment. **D**, Temperature responses of the LSM-based joule heater at various incident powers. **E**, Infrared images of the LSM-based joule heater on the human wrist at the flexed and extended states.

The LSM-based electrophysiological sensors, exhibiting a skin-device contact impedance of ~28 kΩ at 100 Hz, comparable to that of conventional Ag/AgCl gel

electrodes (~34 kΩ at 100 Hz) (**Figure 2.14**), demonstrate the potential to perform high-fidelity measurements of ECG, EEG and EMG from various locations of human bodies.

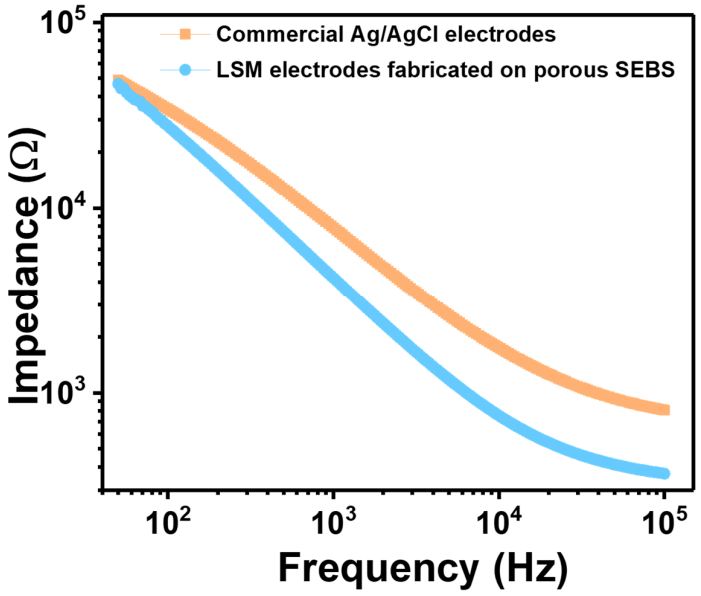


Figure 2.14. Contact impedances of the skin-device interface of LSM electrodes fabricated on porous SEBS and conventional Ag/AgCl gel electrodes. The impedances were measured from the forearm of a human subject.

Figure 2.15A and **B** show that the electrophysiological sensors can continuously record ECG signals from human chests with clearly distinguishable P-wave, QRS complex and T-wave and high quality signals with the signal-to-noise ratio (SNR) of ~21.2 dB and, which is comparable with the electrophysiological sensors made of silver nanowires on porous SEBS (SNR: ~22.7 dB). Additionally, since breathing can cause the intrathoracic impedance variations, and R peak amplitude decreases as the intrathoracic impedance increases during inspiration, while it increases as the latter decreases during expiration. The respiration rates, together with the instantaneous heart rates can be determined from recorded ECG signals as shown in **Figure 2.15C-E** and the results agree well with the data measured with conventional methods.

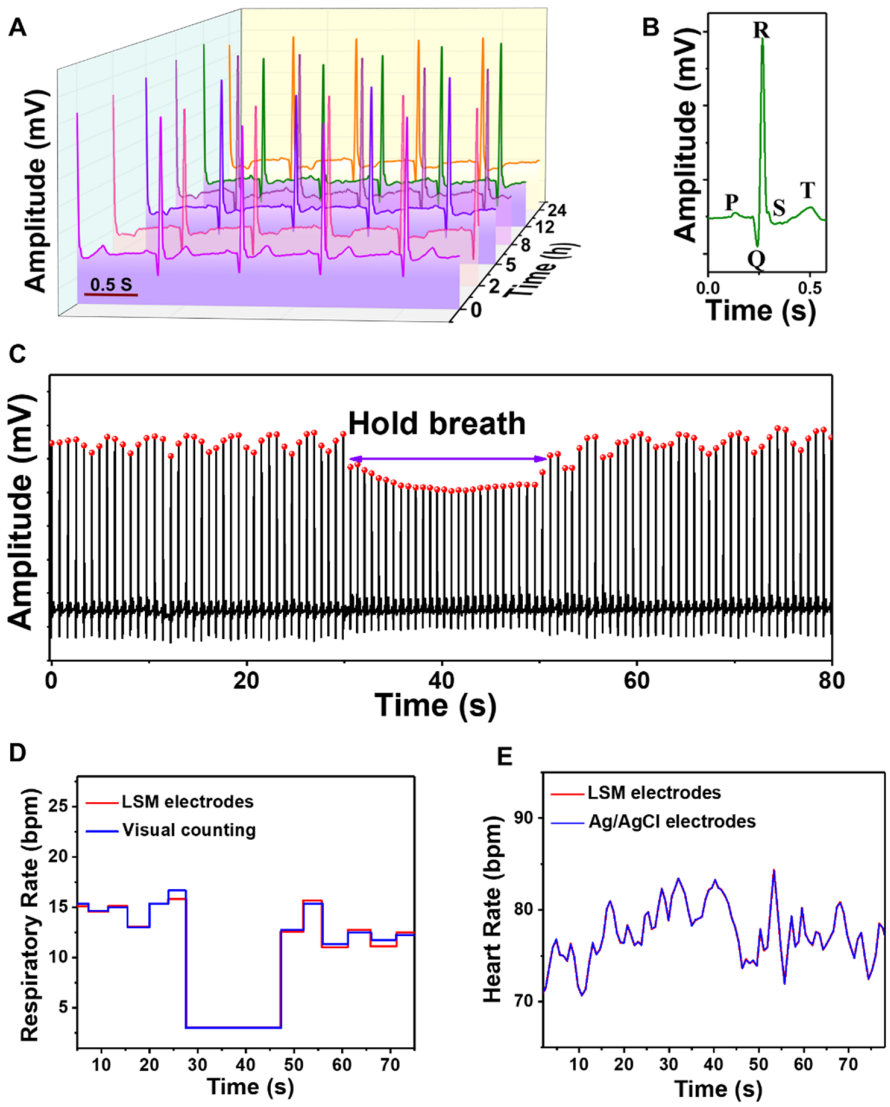


Figure 2.15. On-body evaluation of the LSM-based ECG sensor**. A,** 24-hour ECG recording from the chest skin of a human volunteer using the LSM-based electrophysiological sensor. **B,** A magnified ECG signal from (**A**), demonstrating clearly distinguishable P-wave, QRS complex, and T-wave. **C,** Amplitude response of R peak of recorded ECG signals while human volunteer held the breath for 20 s.. **D**, Respiratory rates calculated by R peak amplitude variations in ECG signals recorded by LSM electrodes and visual counting by a physician. **E**, Instaneous heart rates calculated from R-to-R peak intervals in ECG signals recorded by LSM electrodes and Ag/AgCl electrodes, which agree well with each other.

In addition, the electrophysiological sensors can capture EEG signals (i.e., alpha

rhythm with the frequency centered at 10 Hz) from the forehead when the volunteer first closed the eyes for 50 s and then opened the eyes for 100 s as shown in **Figure 2.16**.

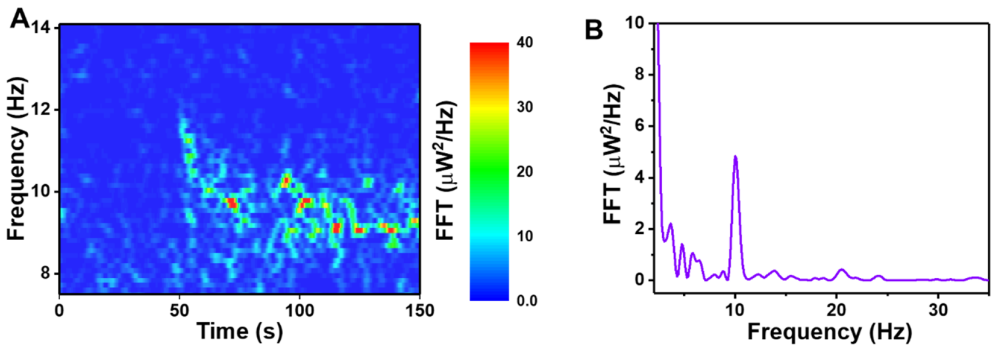


Figure 2.16. On-body evaluation of the LSM-based EEG sensor. EEG signals recorded from the foreheads of human volunteers using the LSM-based electrophysiological sensors when human volunteers first opened their eyes for 50 s and then closed their eyes for 100 s (**A**) and the corresponding fast Fourier transform (FFT) analysis **(B)**, indicating that the alpha rhythm centers at ~10 Hz.

High quality EMG signals are also collected from the LSM epidermal electronics on porous SEBS. When the devices are applied on the forearm (flexor carpi radialis muscle) of a volunteer, the EMG signals produced by wrist flexion for different times (**Figure 2.17A**) and even a finger flexion (**Figure 2.17B**) can be clearly detected. The SNR of the LSM-based EMG sensor is ~19.2 dB, comparable to that of EMG signals recorded with the electrophysiological sensors made of silver nanowires on porous SEBS (with SNR of~20.7 dB). Furthermore, when we use LSM as electrodes and a monophasic square pulse of 2 mA with pulse duration of 50 ms (**Figure 2.17C**, bottom) are applied to the forearms of a volunteer to conduct electrical stimulations, high-amplitude EMG signals are also detected (**Figure 2.17C**, top) and they show a good alignment between the stimulated electrical signals and induced EMG signals, indicating potential applications in wound healing, pain relief, and rehabilitation by providing programmed electrical stimulations (*36-38*).

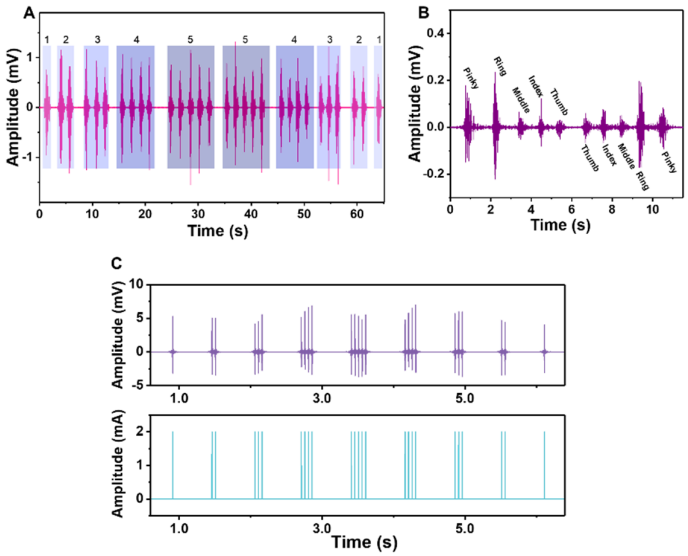


Figure 2.17. On-body evaluations of the LSM-based EMG sensor and electrical stimulator. EMG signals recording from the forearm (flexor carpi radialis muscle) of a human volunteer using the LSM-based electrophysiological sensors when the volunteer bent his wrist for different times (**A**) and bent his different figures (**B**). **C**, EMG signals measured from the flexor carpi radialis muscle (top) during the programmed electrical stimulations (bottom; monophasic square pulse of 2 mA with pulse duration of 50 ms).

Sweat biochemical sensing can provide insights of the health status from the molecular level (*39*, *40*). In this work, we have developed LSM-based sweat biochemical sensors for glucose, UA and CAF detections, which can be further extended for monitoring other sweat biochemicals via additional functionalizations of LSM basis electrodes. The glucose sensors include Ag/AgCl ink fabricated reference electrode, LSM counter electrode and work electrodes. The glucose detection is based on the glucose oxidation by the glucose oxidase on the LSM working electrode (coated with carbon inks, Au nanoparticles, Prussian blue, and glucose oxidase), which is accompanied with hydrogen peroxide production. The current produced by oxidizing hydrogen peroxide is linearly proportional to the glucose concentration. Thus, glucose concentrations can be determined by monitoring the response currents.

The palpable dynamic current to glucose concentration at the range of 0-600 μM is observed (**Figure 2.18A**) and the fitted linear equation exhibit a sensitivity of 15.7 nA μM^{-1} with limit of detection (LOD) of 1.44 μM. (**Figure 2.18 B**) Also, **Figure 2.18C-E** indicates that the LSM-based glucose sensor exhibits high repeatability, long-term stability, and high selectivity. For example, as shown in **Figure 2.18E**, the interferential sweat analytes of lactate, UA and CAF have negligible effect on glucose monitoring.

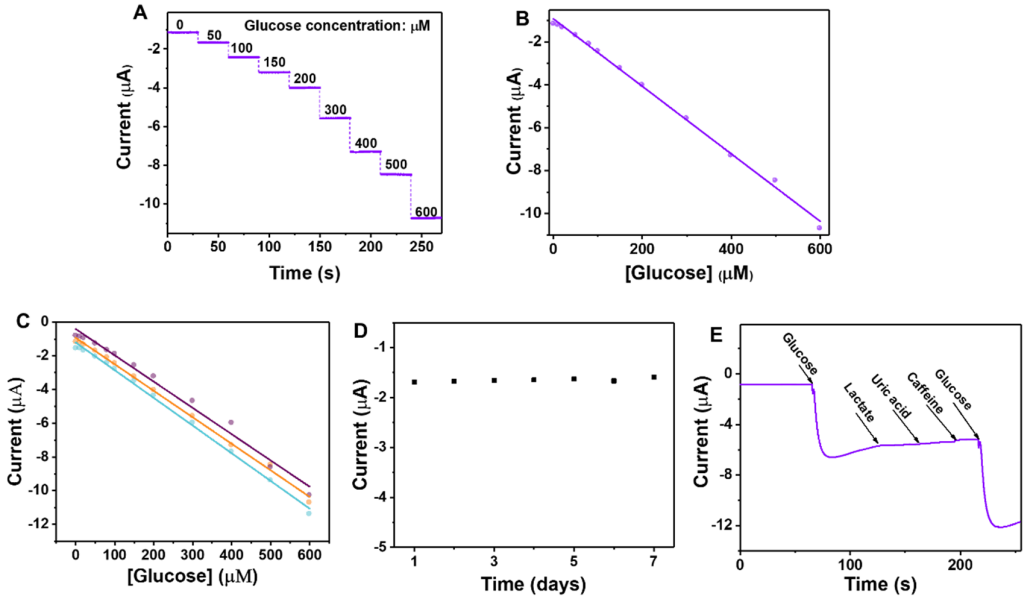


Figure 2.18. Characterizations of the LSM-based glucose sensor. Dynamic current responses to different glucose concentrations from 0 to 600 μM (**A**), calibration plot (**B**), repeatability test (**C**), stability test (**D**), and selectivity test (**E**) of LSM-based glucose sensors. All the tests were conducted in 0.1 M phosphate buffer solution (pH: 6.0). The stability test was performed with the glucose concentration at 50 μM. R^2 is 0.997 for the line fit in (**B**). The sensitivity is ~15.7 nA μM^{-1} and the limit of detection is ~1.44 μM.

We use a sensor containing Ag/AgCl ink-based reference electrode, LSM counter electrode and carbon ink decorated work electrode to simultaneously detect the concentration of UA and CAF with DPV method. With the existence of 20 μM CAF,

the peak currents at ~0.15 V caused by the selective oxide of UA display a linear increase at the UA range of 0-300 μM, and the achieved sensitivity is 63.9 nA μM^{-1} with the LOD of 0.9 μM (**Figure 2.19 A** and **B**). Additionally, the sensor exhibits good repeatability (**Figure 2.19 C**), long-term stability (**Figure 2.19 D**), and high selectivity among various chemicals, including lactate, UA and CAF (**Figure 2.19 E**), demonstrating its robust performances under practical applications.

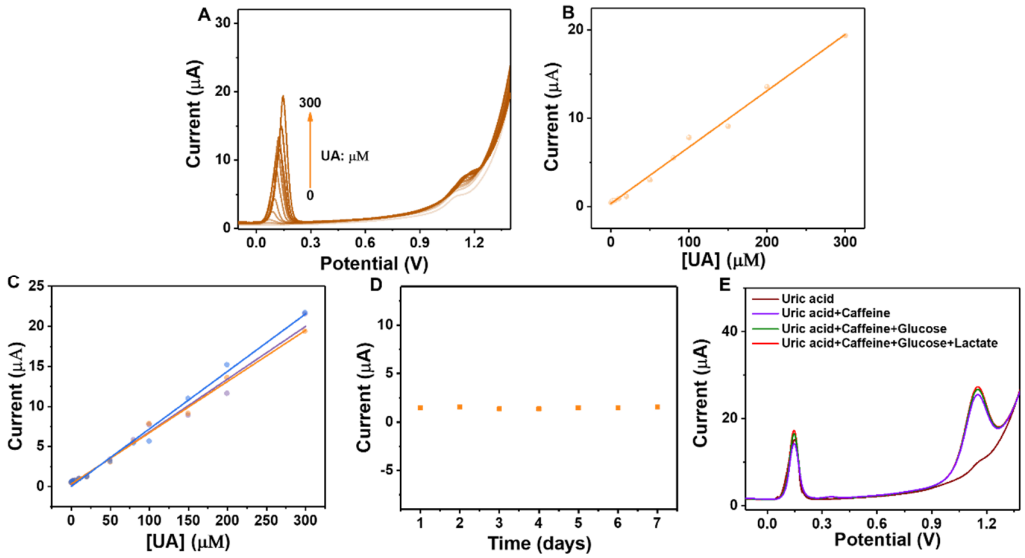


Figure 2.19. Characterizations of the LSM-based uric acid sensor. Differential pulse voltammetry (DPV) responses to different UA concentrations from 0 to 300 μM (**A**), calibration plot (**B**), repeatability test (**C**), and stability test (**D**), and selectivity test (**E**) of LSM-based UA sensors. All the tests were conducted in 0.1 M buffer solution (pH: 6.0) with existence of 20 μM caffeine. The stability test was performed with the UA concentration at 25 μM. R^2 is 0.993 for the line fit in (**B**).

Similarly, the calibration of CAF is conducted under the existence of 10 μM UA and the peak currents at ~1.11 V ascribed to the oxide of CAF also manifest a good linear relationship with CAF concentration with a sensitivity of 47.3 nA μM^{-1} and a LOD of 0.35 μM (**Figure 2.20 A** and **B**). The repeatability, long-term stability selectivity among other chemical are tested and obtained good results as shown in **Figure 2.20 C-E**.

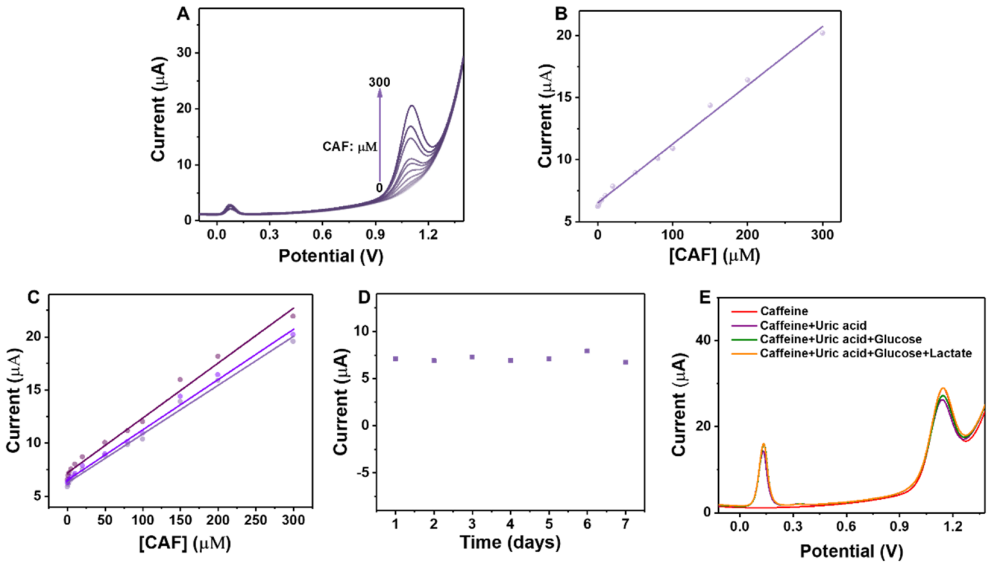


Figure 2.20. Characterizations of the LSM-based caffeine sensor. DPV responses to different CAF concentrations from 0 to 300 μM (**A**), calibration plot (**B**), repeatability test (**C**), stability test (**D**), and selectivity test **(E)** of LSM-based CAF sensors. All the tests were conducted in 0.1 M buffer solution (pH: 6.0) with existence of 10 μM uric acid. The stability test was performed with the CAF concentration at 50 μM. R^2 is 0.993 for the line fit in (**B**). The sensitivity is ~47.3 nA/μM and the limit of detection is ~0.35 μM.

LSM-based representative bioelectronic devices that are exposed to air (i.e., devices on the top side of the Janus wearable), which are useful in health and environmental monitoring. For example, excessive exposure to UV radiation has associated risks with various medical conditions (e.g., skin cancer, skin aging) (*41*). The fabricated UV sensor is based on the LSM electrode decorated with ZnO nanowires (*42*). The performances of UV sensor are presented in **Figure 2.21.** The I-V curves displayed in **Figure 2.21**A illustrate the increasing current with the UV intensity increasing from 0 to 1000 μW cm^{-2}. The linear relationship between the current at the applied voltage of 1 V and $\log_{10}$(UV) is presented in **Figure 2.21**B. The average sensitivity of 0.73 μA for 1 μW cm^{-2} UV increase from 100-1000 μW cm^{-2} can be achieved. The on-off ratio of the sensor at the UV intensity of 50 μW/cm^{-2} is around 10^4. The response time to

the dynamic change of the UV light illumination is ~22 s. (The response time was defined as the time taken to reach 90% of the maximum resistance response after the UV is on) as shown in **Figure 2.21C** and **D**.

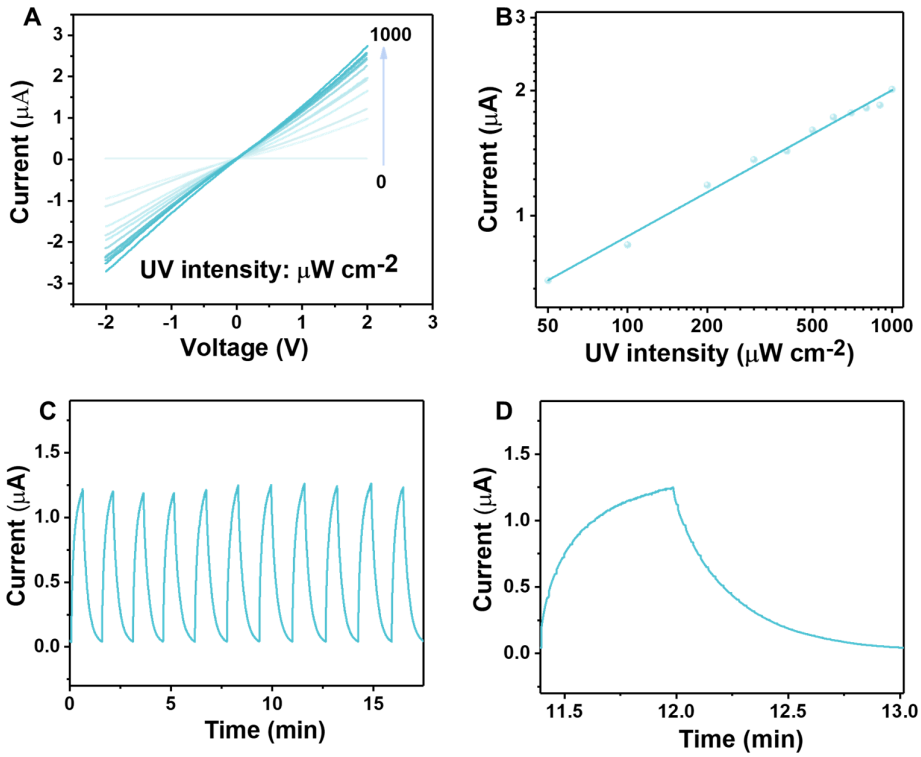


Figure 2.21. Characterizations of the LSM-based UV sensor**.** I-V curves of the LSM-based UV sensor measured under various UV illumination intensities from 0 to1000 μW cm^{-2} (**A**) and the calibration plot (**B**). Here, R^2 is 0.991 for the line fit and the produced photocurrent follows a power-law relationship with the incident UV intensity ($I \propto P^{0.35}$). Current responses of the LSM-based UV sensor under cyclic UV illumination with the illumination intensity at 1000 μW/cm^2 and with the bias voltage at 1.5 V (**C**) and the magnified response profile (**D**). Here, the wavelength of the UV light is 365 nm. The diameters of ZnO nanowires, coated on the LSM interdigital electrodes, are around 50-120 nm.

In addition, the humidity in the air and human breath can be detected based on the water absorption and desorption on GO (*43*) coated on the LSM interdigital electrode (**Figure 2.22**), which can lead to the capacitance change. It can be observed that the capacitances increase significantly with the increasing relative humidity (RH) at

various frequency (**Figure 2.22A**) and at the frequency of 100 Hz (**Figure 2.22B**), RH and the $\log_{10}$(capacitances) exhibit a good linear relationship with the slope of 0.03. The average sensitivity of 475 pF per % RH can be calculated (**Figure 2.22C**). We also employ the sensor to conduct respiratory detection (**Figure 2.22D**). When the volunteer breathes out, the sensors can capture the water vapor and the capacitance increases.

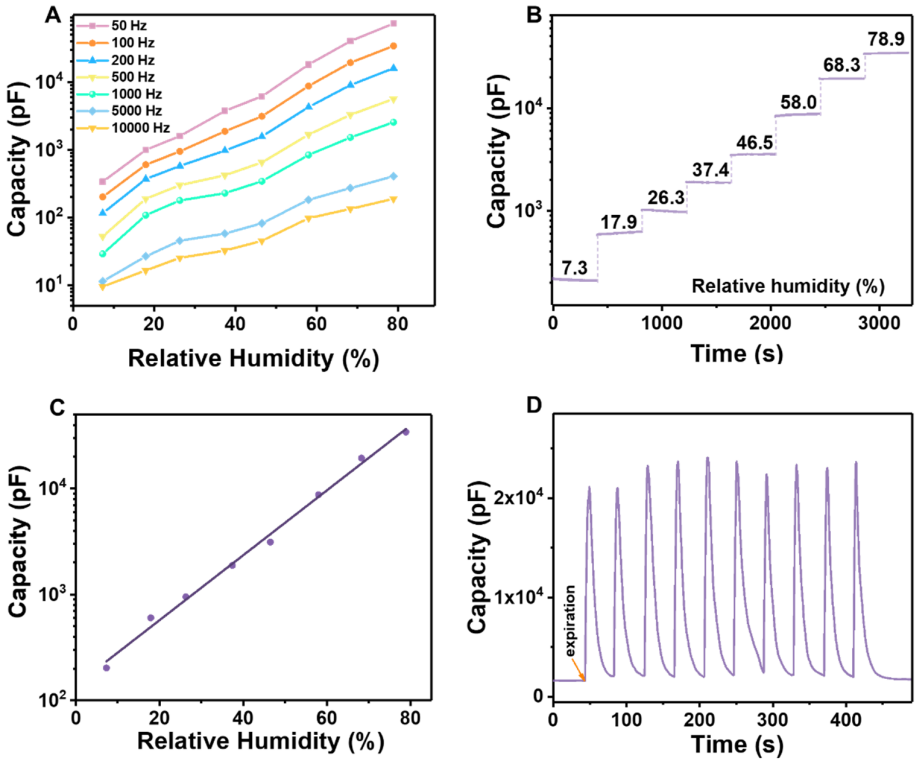


Figure 2.22. Characterizations of the LSM-based humidity sensor. (**A**) Capacitance responses of the LSM-based humidity sensor at various frequencies and relative humidity under the bias voltage of 0.5 V. Dynamic capacitance changes of the LSM-based humidity sensor under the stepwise changed humidity (**B**) and the corresponding calibration plot (**C**). Here, R^2 is 0.994 for the line fit. (**D**) Capacitance responses of the LSM-based humidity sensor to human breath. The results in (**B-D**) are measured at the frequency of 100 Hz and the bias voltage of 0.5 V.

The alcohol gas sensor, consisting of LSM interdigital electrodes coated with WSe_2 nanoflakes, can detect alcohol gas concentrations in the human breath samples (**Figure**

2.23) because the absorbed alcohol molecules on WSe_2 can reduce the depletion layer formed by O_2 absorption, attributing to more electron release, and leading to decreased resistance (*44*). From **Figure 2.23A** and **B**, a positive increase of resistance to alcohol vapor concentration is displayed. And at the range of alcohol vapor concentrations from 100 to1000 ppm, the resistance variations show a good linear relationship with the concentrations with the sensitivity of 1.44 % per100 ppm (**Figure 2.23C**). The dynamic response of the resistance variation to 10 ppm alcohol vapor are shown in **Figure 2.23D** and **E** and the sensor exhibits a faster response than recovery. We also test the selectivity of the sensors to different molecules as presented in **Figure 2.23F**.

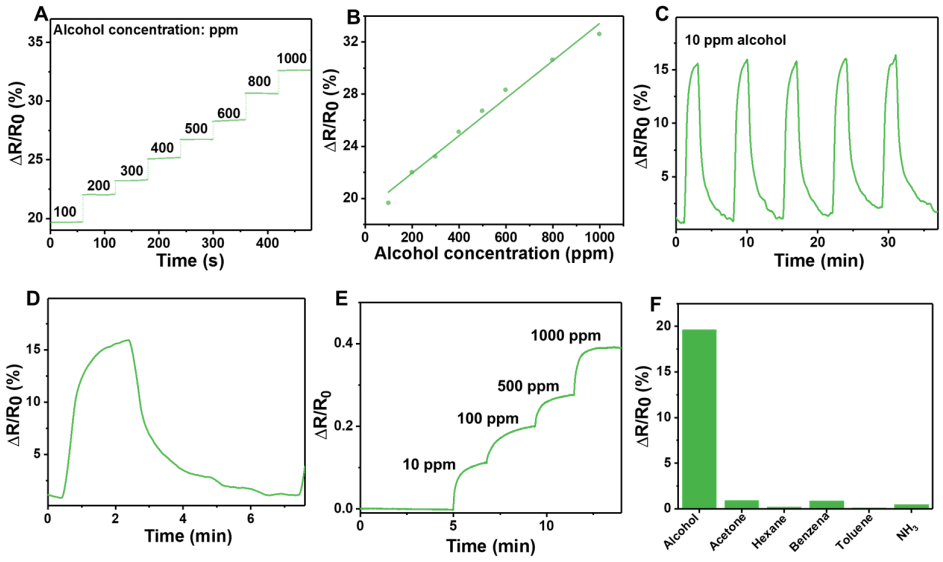


Figure 2.23. Characterizations of the LSM-based alcohol gas sensor. Dynamic resistance responses of the LSM-based alcohol gas sensor to various alcohol concentrations from 100 to 1000 ppm (**A**) and the calibration plot (**B**). Here, R^2 is 0.982 for the line fit. Dynamic resistance responses of the LSM-based alcohol gas sensor to on and off of 10 ppm alcohol (**C**) and the magnified response profile (**D**). **E**, Cyclic dynamic resistance responses of the LSM-based alcohol gas sensor to the human breath samples of a healthy subject, which was dosed with alcohol gases at the concentrations of 10 ppm, 100 ppm, 500 ppm and 1000 ppm. **F**, Selectivity test of the LSM-based alcohol gas sensor by exposing the device to various volatile organic compounds (concentrations: 100 ppm).

Additionally, detecting amine gases (e.g., ammonia, putrescine, cadaverine) are achieved on the p-toluene sulfonate hexahydrate doped polyaniline (PTS-PANI)-coated LSM interdigital electrodes because the amine groups of absorbed gas molecules can donate lone electrons to PTS-PANI, resulting in the dedoping and increasing the resistance of PANI (*45*). As shown in **Figure 2.24**, the obtained NH_3 gas sensor exhibits an obvious response toward different NH_3 concentrations. The resistance variations increase notably with the increasing NH_3 concentration from 0 to 400 ppm. Good linear relationship between the resistance response and NH_3 concentration can be found with the sensitivity of 7.3 % per ppm NH_3 at the range of 0-50 ppm (**Figure 2.24 A** and **B**) and the sensitivity of 33% per ppm NH_3 at the range of 50-400 ppm (**Figure 2.24 C** and **D**).

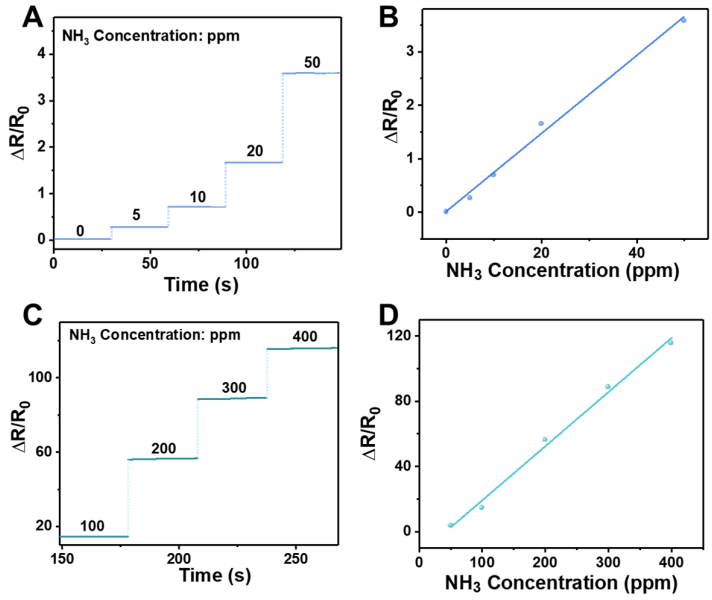


Figure 2.24. Characterizations of the LSM-based NH_3 gas sensor. Dynamic resistance responses of the LSM-based NH_3 gas sensor to various NH_3 concentrations from 0 to 50 ppm (**A**) and the calibration plot (**B**). Dynamic resistance responses of the LSM-based NH_3 gas sensor to various NH_3 concentrations from 100 to 400 ppm (**C**) and the calibration plot **(D)**.

Bedsides the detection of NH_3, the obtained sensor also responds to biogenic amine

gases (e.g., putrescine, cadaverine), which can be used for monitoring food spoilage (*45*). As shown in **Figure 2.25A-D**, there is a good linear relationship between the resistance responses and different biogenic amine gases of putrescine and cadaverine. Additionally, cyclic dynamic resistance response of the LSM-based NH_3 sensor to on and off of 60 ppm NH_3 (**Figure 2.25E**) demonstrates the good stability of the sensors. The dynamic response of the sensor to breath gas samples, infused with NH_3 gas at various concentrations, has also been evaluated, revealing significant responses (**Figure 2.25F**), which underscores the sensor's potential in monitoring certain diseases, such as liver failure (*46*). The responses of the LSM-based NH_3 sensor to other volatile organic compounds besides NH_3 and biogenic amine are also tested and negligible influence are observed (**Figure 2.25G**).

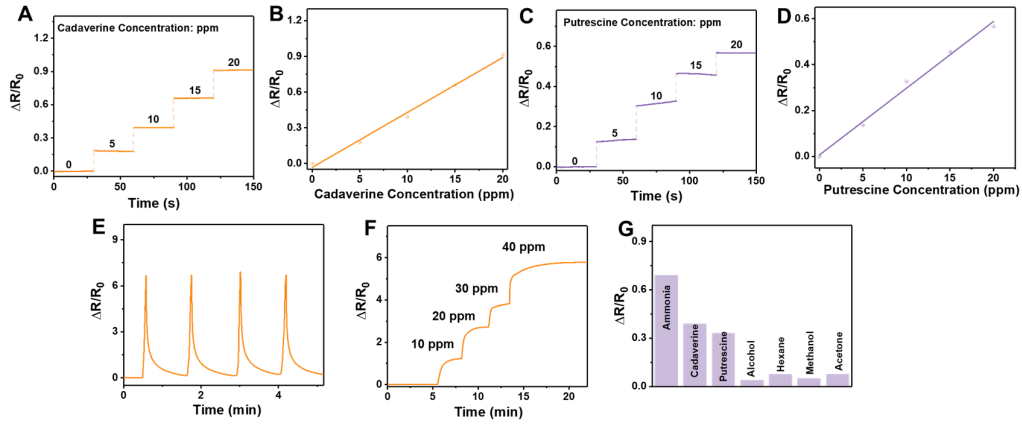


Figure 2.25. Dynamic resistance responses of the LSM-based NH_3 gas sensor to various cadaverine concentrations from 0 to 20 ppm (**A**) and the calibration plot (**B**). Dynamic resistance responses of the LSM-based NH_3 sensor to various putrescine concentrations from 0 to 20 ppm (**C**) and the calibration plot (**D**). Cyclic dynamic resistance changes of the LSM-based NH_3 gas sensor to on and off of 60 ppm NH_3 (**E**). Cyclic dynamic resistance changes of the LSM-based NH_3 gas sensor to the breath gas samples of a healthy subject, which was dosed with NH_3 gases at the concentrations of 10 ppm, 20 ppm, 30 ppm and 40 ppm (**F**). (**G**) Selectivity test of the LSM-based NH_3 gas sensor by exposing the device to various volatile organic compounds (concentrations: 10 ppm).

2.6 Demonstration of Janus on-skin wearables in daily-life activities

Here, the Janus wearable device is interfaced with the mobile data acquisition circuit for in-situ data processing and wireless data transmission by Bluetooth Low Energy to realize the real-time and continuous daily-life activities monitoring. The mobile data acquisition circuit is assembled on a flexible printed circuit board (FPCB) with the off-the-shelf electronic components (**Figure 2.26A**). The simplified block diagram is shown in **Figure 2.26B.** And the recorded biosignals can display on the smartphone installed with a customized mobile software application (**Figure 2.26C**). **Figure 2.26D** shows the optical image of the Janus on-skin wearable device connected with the mobile data acquisition circuit. And the detailed used off-the-shelf electronic components are shown in **Figure 2.26E**.

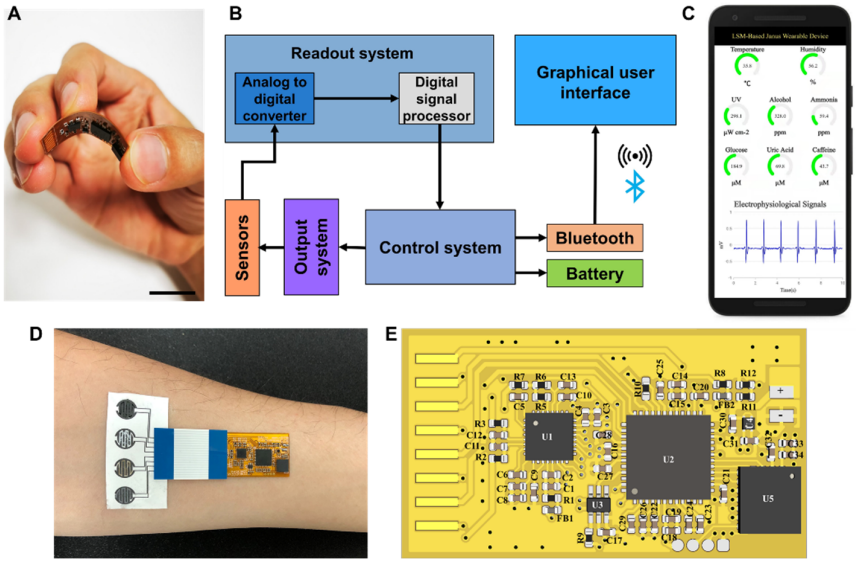


Figure 2.26. A, Photograph of the flexible printed circuit board assembled with off-the-shelf electronic components for in-situ data processing and Bluetooth-enabled wireless data transmission. Scale bars: 1 cm**. B,** System-level block diagram of the mobile data acquisition circuit. **C**, Illustration of graphic data display on the smartphone installed with a customized software application. **D**, Optical image of the Janus on-skin wearable device connected with the mobile data acquisition circuit and **E**, Schematic illustration of the flexible printed circuit board assembled with the off-the-shelf electronic components.

In addition to potential applications in healthcare enabled by physiological monitoring and programmed stimulations, we have further demonstrated the potential applications of LSM-based Janus wearables in daily activities. In the first scenario, a human volunteer took a walk on the campus playground where a high UV intensity (~321 μW cm^{-2}) and a low relative humidity (~20%) were detected. Thus, the volunteer went to a nearby trail for a walk (**Figure 2.27**), which is surrounded by trees and a rivulet and has a healthy environment (UV intensity: ~45 μW cm^{-2} humidity: ~45%).

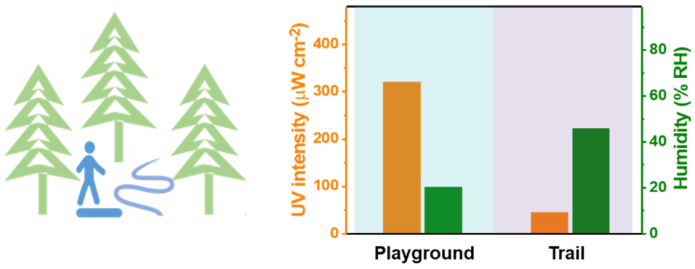


Figure 2.27. Illustration (left) and the UV light density and relative humidity on the campus playground and a nearby trail (right) measured with the LSM-based Janus wearable.

In the second scenario, the volunteer had beef, fish and coffee for his brunch. Before cooking beef and fish, the volunteer checked the food spoilage using LSM-based Janus wearables (**Figure 2.28A**). After finishing brunch, the glucose, UA and CAF in the sweat of the volunteer were tracked using LSM-based Janus wearables. **Figure 2.28B** shows that the sweat concentrations of these biochemicals first dramatically increased and then returned to their normal levels after about eight hours due to metabolism.

In the second day, the volunteer drank white wine [~0.5 g white wine (56% alcohol by volume) per 1 kg body weight of the volunteer]. It is known that alcohol intake has both short-term and long-term effects on the human body and behavior. Here, LSM-

based Janus wearables can track the brain and heart activities and breath alcohol

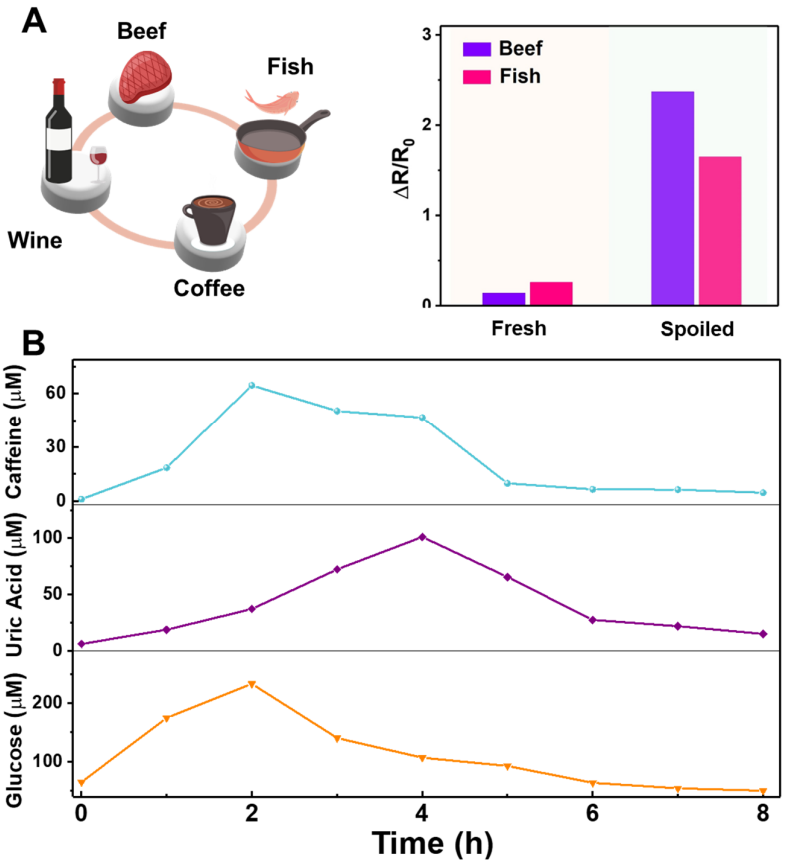


Figure 2.28. A, Illustration (left) and electrical resistance responses of the LSM-based ammonia sensor to the fresh and spoiled fish and beef (right). **B**, Dynamic concentration changes of the caffeine, uric acid and glucose in human sweat before and after eating bruch (including beef, fish and coffee) over an 8-hour period. Here, exercise was used to produce sweat.

concentrations of the volunteer (**Figure 2.29A**), showing potential applications in alcoholism studies. In specific, slow alpha activity ($\Delta S/S_0$) rapidly increased at the beginning 15 mins of wine drinking, associated with episodes of subjective euphoria caused by alcohol intake, and then relatively slowly increased to the peak value in the following two hours, consistent with a more relaxed but awake mental state induced by alcohol intake (*47*). Here, S_0 is the integral area of slow alpha rhythm (~7.5-10 Hz) before alcohol intake. And ΔS is calculated by subtracting S_0 from the integral area of

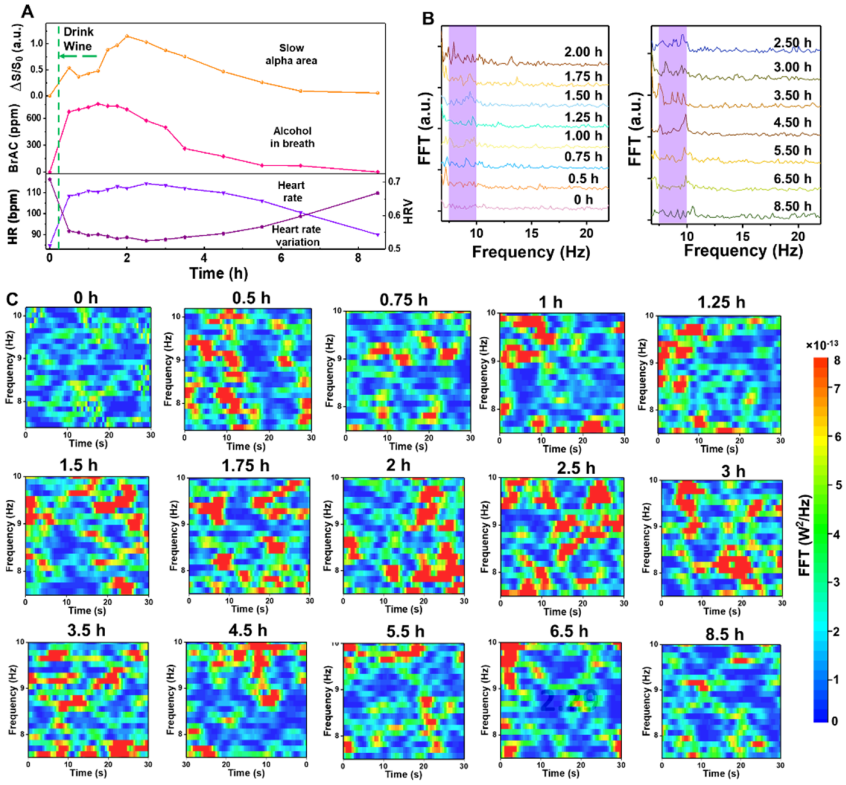


Figure 2.29. A, Dynamic changes of the relative changes of slow alpha area ($\Delta S/S_0$), breath alcohol concentration (BrAC), heart rate (HR), and heart rate variation (HRV) before and after drinking wine over an 8.5-hour period. **B**, FFT-processed frequency distributions of recorded EEG signals and Time-frequency spectrograms of recorded EEG signals within slow alpha band (7.5-10 Hz) (**C**) before and after the volunteer drank white wine over an 8.5-hour period.

slow alpha rhythm recorded at different time after alcohol intake (**Figure 2.29B** and **C**). Besides, the concentration of breath alcohol was tracked by LSM-based alcohol gas sensors, which reached the peak value after about two hours of wine drinking and returned to the normal value after around eight hours (**Figure 2.30**). Notably, the heart rate (HR) and heart rate variation (HRV) can be determined from the ECG signals recorded by LSM-based electrophysiological sensors. After drinking white wine, the volunteer's HR increased and his HRV decreased, indicating decreased efficiency of autonomic control (*48*). It needed about eight hours for his HR and HRV to return to their normal values.

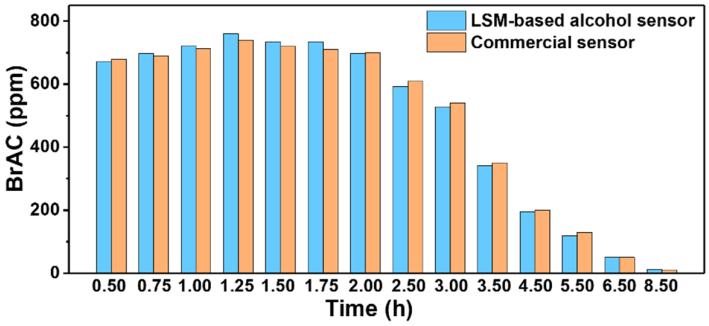


Figure 2.30. Breath alcohol concentrations (BrAC) measured by the LSM-based alcohol gas sensor and a commercial breath alcohol tester (BT-S80, BACtrack) after the volunteer drank white wine over an 8.5-hour period, indicating good alignment.

2.7 Light-driven soft actuator based on laser-scribed MoO_2

Soft actuator is the basic building block of some emerging complex functional devices and can find broad applications in reconfigurable 3D structures, reshapable bioelectronics, soft robots, responsive metamaterials, tunable optics, and many others (*13, 49*). In this section, we have developed LSM-based light-driven soft actuators by taking advantage of its outstanding photothermal effect (*20, 21*). As shown in. **Figure 2.31A**, the soft actuator consists of PI, LSM, and PDMS trilayer structures. Here, LSM serves as pliable photothermal heater. Upon infrared illumination (Phillips, BR40 Infrared Lamp), the actuator can bend to the PI side due to the stress caused by the significant thermal expansion difference between PI and PDMS.

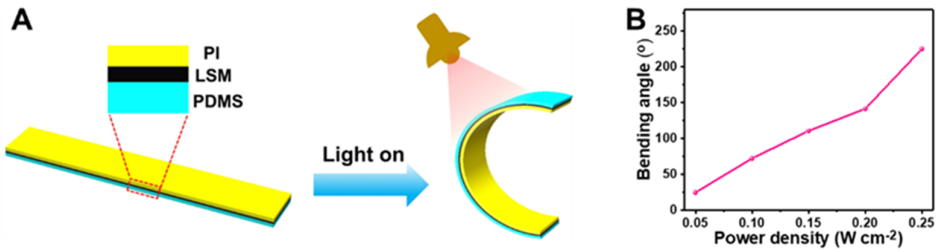


Figure 2.31. A, Schematic illustration of LSM-based light-driven soft actuator. **B**, Maximum bending angles of LSM-based soft actuator as a function of the power density of the infrared lamp (Phillips, BR40 Infrared Lamp)

The maximum bending angle can be controlled by the power density of the infrared lamp (**Figure 2.31B** and. **Figure 2.32**). The soft actuator takes about 7 s to bend from

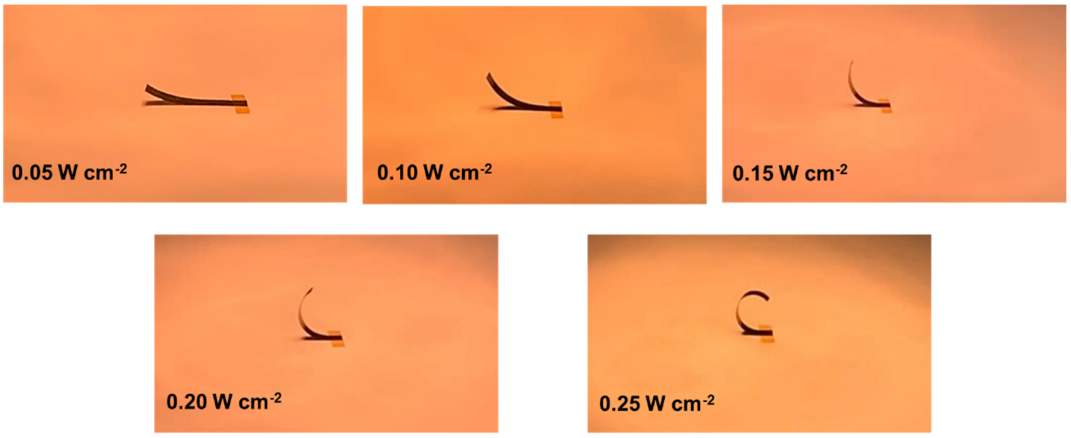


Figure 2.32. A, Optical images of LSM-based soft actuators under bending, triggered by the infrared illumination with different power densities. Scale bars: 0.5 cm.

0° to 225° and needs about 9 s to recover. **Figure 2.33** and **Figure 2.34** illustrate reconfigurable 3D structures made of LSM-based soft actuators. The demonstration

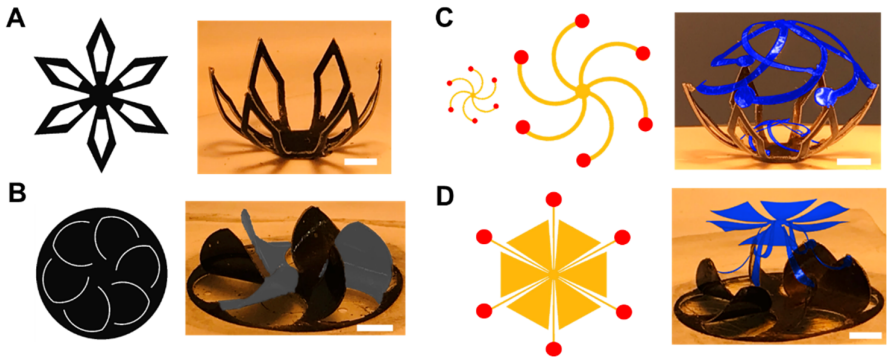


Figure 2.33. Flower-like (**A**) and windmill-like (**B**) reconfigurable 3D structures (right) and their corresponding 2D patterns (left). Reconfigurable multilayer 3D architectures (right) formed by combining LSM-based soft actuator with the mechanically assembled bilayer cage (**C**) and umbrella (**D**) and the corresponding 2D patterns of the cage and umbrella (left). Here, red dots in 2D patterns indicate bonding sites. Scale bar: 0.5cm for A-D.

examples include flower-like 3D structures and windmill-like 3D structures and integrations with mechanically assembled 3D structures to form complicated,

multilayer 3D architectures (*50, 51*). The reconfigurations between 2D and 3D shapes can be achieved reversibly by turning off and on infrared illumination.

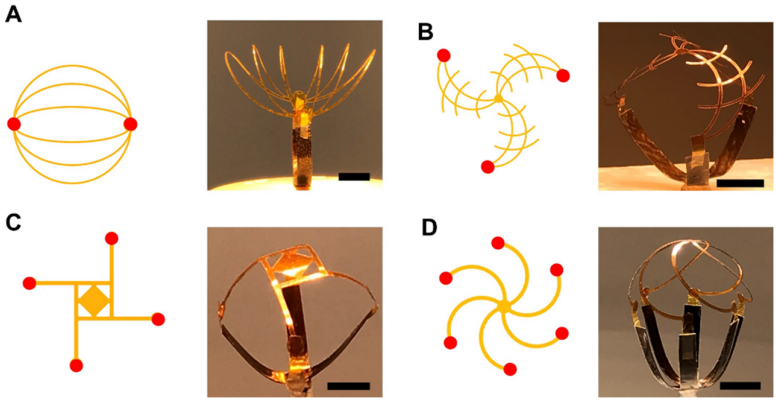


Figure 2.34. Four reconfigurable multilayer 3D architectures formed by combining LSM soft actuators with mechanically assembled 3D structures. The corresponding 2D patterns of mechanically assembled 3D structures are provided on the left panels in (**A-D**). And red dots indicate the bonding sites. Scale bars: 1 cm.

Taking advantage of the 2D-to-3D reconfiguration, a reshapable wearable airflow sensor has been developed (**Figure 2.35 A** and **B**). The sensor consists of six petal-like LSM-based soft actuators. And each of them is integrated with a strain gauge made of

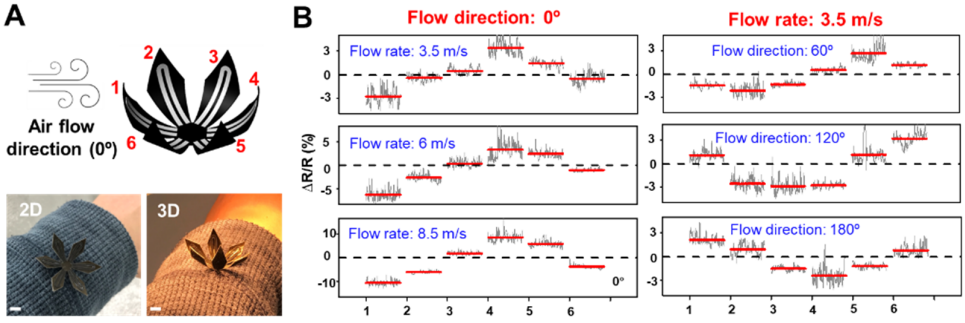


Figure 2.35. A, Schematic illustrationand optical images of the reshapable wearable airflow sensor. The airflow sensor consists of six petal-like LSM soft actuators. And each of them is integrated with a strain gauge made of laser-induced graphene, classified as sensing channels 1-6. Scale bars: 0.5 cm. **B**, Electrical resistance responses of the six sensing channels of the reshapable airflow sensor under different flow rates (left) and flow directions (right).

laser-induced graphene, classified as six sensing channels. These sensing channels are separately addressable. When not in use, the sensor is in its 2D configuration to save space. During operation, the sensor reconfigures into 3D structure, which can not only provide high sensitivity (**Figure 2.36**) but also detect the direction of airflow by measuring resistance changes in the six sensing channels. developed

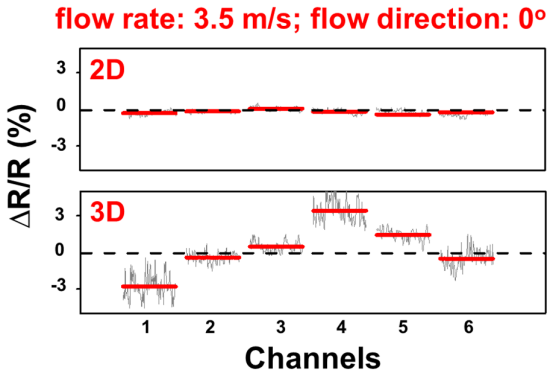


Figure 2.36. Dynamic resistance responses of six sensing channels of the reshapable wearable airflow sensor at the 2D configuration (top) and 3D configuration (bottom).

Furthermore, we have an LSM-based worm-like smart soft robot (**Figure 2.37**). The smart soft robotic worm, integrated with the ammonia sensor, can perform controlled motions driven through on and off of infrared illumination and can detect the ammonia leakage in the environment, indicating potential applications in environmental monitoring and homeland security.

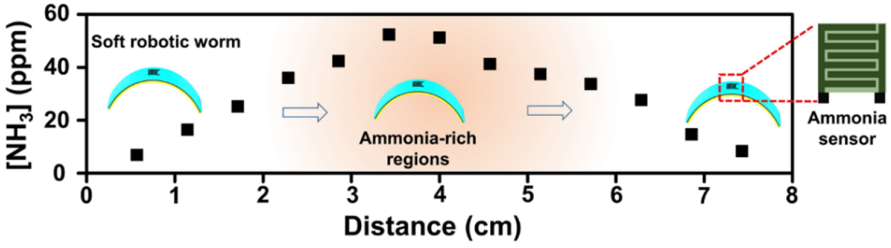


Figure 2.37. Ammonia gas concentrations at different locations of an 8 cm-length trail, measured by a smart robotic worm integrated with an ammonia gas sensor. Here, an open bottle with the ammonium hydroxide solution (~30% by weight) was placed in the middle of the trail.

2.8 Conclusion

In summary, we developed a laser-assisted, universal fabrication approach to scribe MoO_2 with arbitrary patterns on soft elastomers and other substrates. LSM demonstrates high electrical conductivity, biocompatibility, chemical stability, MRI-compatibility, and photothermal effects. Furthermore, we have developed LSM-based on-skin wearable devices which have the Janus device layouts and can link with mobile data acquisition circuits for in-situ data processing, wireless data transmission and graphic data display on the smartphone. The obtained Janus on-skin wearables can not only monitor a rich variety of physiological signals from human skin but also collect useful information from both human breath and surrounding environments. Additionally, we have developed LSM-based light-driven soft actuator and demonstrated its applications in reconfigurable 3D architectures, reshapable wearable airflow meters, and smart soft robotic worms integrated with bioelectronics.

2.9 Materials and methods

Materials. Molybdenum chloride, ethanol, phosphate buffered saline (PBS), ammonium hydroxide, aniline, carbon ink (E3449) and Ag/AgCl ink (E2414) were purchased from Thermo Fisher. Lactate, uric acid, glucose, caffeine, putrescine, cadaverine, glucose oxidase, iron (III) p-toluene sulfonate hexahydrate, and graphite flakes were purchased from Sigma-Aldrich. ZnO nanowires (NWZO01A5) were purchased from ACS Material. PDMS（Sylgard 184) was purchased from Dow. PI (Kapton®100HN) was received from Dupont. SEBS (H1062) was received from Asahi Kasei. Nafion solutions and WSe_2 were purchased from Alfa Aesar.

LSM and device fabrication. The fabrication of LSM begins with the preparation of the precursor solutions [1 M $MoCl_5$ in deionized water (DI-water) and ethanol with

the volume ratio of 1:4]. Next, the precursor is spray-coated on the targeted substrate using a commercial airbrush (G222; Master Airbrush). Here, the amount of spray-coated $MoCl_5$ can be controlled by the volume of spray-coated precursor solutions. Subsequently, CO_2 laser scribing of MoO_2 is performed using a VLS2.30 universal laser system (wavelength: 10.6 μm, beam size: 120 μm, pulse duration:14 μs, maximum power: 30 W, and maximum scanning speed: 23 inch/s) at ambient conditions. If not particularly indicated, the setting of the CO_2 laser system is fixed at the 7% of the maximum power, 15% of the maximum scanning speed, a raster mode, 5 for the image density, and 1000 for the pulse per inch. Here, the 15% of the maximum laser scanning speed is chosen based on the balance between the production efficiency and production stability. 5 for the image density means 500 lines per inch for our CO_2 laser system (VLS2.30). Finally, washing away unexposed precursors using DI-water and drying the samples in the air complete the LSM fabrication process. And SEBS porous were prepared following our published procedures.

There were no additional modifications on LSM patterns for electrophysiological sensors and temperature sensors. For sweat sensors, carbon ink- and Ag/AgCl ink-modified LSM electrodes were utilized as the UA/CAF sensing electrode and reference electrode, respectively. The glucose sensing electrode was prepared by functionalizing the carbon ink-modified LSM electrode with Au nanoparticles, Prussian blue, and glucose oxidase following our previously published procedures. The UV sensor, humidity sensor, alcohol gas sensor and NH_3 gas sensor were prepared by adding 30 μl of ZnO nanowires solution (3 mg ml^{-1} in DI-water), 30 μl of GO (3.75 mg ml^{-1} in DI-water), 50 μl of WSe_2 solution (10 mg ml^{-1} in 0.5 % Nafion solution), and 30 μl of PTS-PANI solution (3 mg ml^{-1} in DI-water) onto LSM interdigital electrodes, respectively. Here, GO and PTS-PANI were prepared following

the published procedures (*45, 53*). The soft actuator was prepared by first making LSM on PI (25 μm thick), followed by coating of PDMS (~250 μm thick) on LSM. Then CO_2 laser was used to cut samples into pre-designed shapes for 3D reconfigurations. For laser cutting, the setting of the CO_2 laser system was fixed at 100% of the maximum power, 100% of the maximum scanning speed, a vector mode, 5 for the image density, and 1000 for the pulse per inch.

Characterizations and measurements. X-ray diffraction patterns were taken using a Philips X'Pert Materials Research diffractometer equipped with a CuKα radiation source. Raman spectra were obtained on a Renishaw Raman microscope. SEM and TEM images were taken with an FEI Quanta 600F Environmental SEM and FEI Tecnai F30 G2 Twin Transmission Electron Microscope, respectively. EDS data were obtained by a Bruker Quantax 200 EDS. FT-IR and UV-VIS spectra were collected using a Nicolet 4700 FT-IR spectrophotometer and UV-VIS spectrophotometer (UV-2401, Shimadzu), respectively. Fluorescence images were taken with a Zeiss Axiovert 40 CFL trinocular inverted fluorescence phase contrast microscope. Magnetic susceptibility of LSM was measured by a superconducting quantum interference device (MPMS3, Quantum Design North America, USA). A 3T Siemens Prisma scanner with a 20-channel head coil was used for MRI scanning. Infrared images were collected using a commercial thermal camera (FLIR E6). Mechanical properties were characterized on a Mark-10 ESM303 tensile tester.

For mobile data acquisition, the alcohol, temperature, UV and NH_3 were detected by monitoring the resistance changes under specific voltages with a source meter module, consisting of a direct current/alternating current generator, an output Buffer, and a multiplexer. The humidity was detected by the capacitance measurement with the source meter module. The differential pulse voltammetry module was used for UA

and CAF monitoring. And chronoamperometry was employed for glucose monitoring. Electrophysiological signals were recorded by the physiological potentiometric module consisting of the programmable gain amplifier and digital filter. The signals were smoothed by a low-pass filter and converted by the analog-to-digital converter for further processing in the digital signal processor. The processed data were transmitted to the smartphone wirelessly by Bluetooth Low Energy. The mobile data acquisition circuit was connected to LSM-based wearable devices using the flexible flat cable (FFC, Premo-Flex, Molex) and the Z-axis conductive tape (Adafruit).

Temperature measurements were validated and calibrated using thermocouples (SA1-K, OMEGA Engineering) with a thermometer (HH309A, OMEGA Engineering). Humidity measurements were validated and calibrated using a traceable hygrometer (Fisher Scientific). Electrophysiological measurements were validated and conducted using PowerLab T26 (AD Instruments) and electrical stimulations were performed using the same instrument. UV light was produced by a commercial UV light source with (AI-2UV20DC) and the UV intensity was determined by a UV Meter (General Tools, UV513AB, 280-400 nm). Alcohol measurements were validated and calibrated by a breath alcohol tester (BT-S80, BACtrack). Electrochemical characterizations were conducted using an electrochemical station (CHI660E, CH Instruments, Inc.) The airflow rates were measured using a digital Anemometer (BT-856-A, BTMETER). The resistance, impedance, and capacitance were measured with an LCR Meter (IM3523, HIOKI) and Dual Channel Source Meter (2604B, Keithley Instruments). The Electronic components used in the mobile data acquisition circuit Mobile wireless data acquisition modules are shown in Tabel **2.1**.

In vitro cytotoxicity assay. The cytotoxicity of LSM was studied following a contact mode protocol using HaCaT, U937 and HDF-α (*54*). The LSM samples were

cut into disks with 1 cm diameter and sterilized with 70% ethanol, followed by rinsing with sterilized PBS. Cells (5×10^4 cells cm^{-2}) were cultured in 24-well culture plate using Dulbecco's Modified Eagle's Medium (Thermo Fisher) supplemented with 10% fetal bovine serum (Thermo Fisher). After six hours for cell attachment on the culturing plate, the pre-sterilized LSM samples were carefully transferred to the wells containing cells, ensuring the samples to contact with the cells. Then, the plate containing both cells and LSM samples were cultured for five days, and the culture medium was changed every two days. On day one, three and five, the viability of the cells contacting with LSM samples were determined both qualitatively and quantitatively using an Alamar Blue assay (Thermo Fisher) and a LIVE/DEAD assay. The Alamar Blue assay was implemented following the protocol provided by the manufacturer. The cells were also stained with a LIVE/DEAD cell viability kit (Thermo Fisher) and then examined using an inverted fluorescence microscope (Zeiss, White Plains, NY, USA).

Experiments on human subjects. All experiments were conducted under approval from the Institutional Review Board at the University of Missouri at Columbia (number: 2010272). All human subjects gave written and informed consent before participation in the studies.

Table 2.1 Electronic components used in the mobile data acquisition circuit

Part	Model/Value	Description
C1, C3	1 μF	Signal filter capacitor
C31	1 μF	Power output capacitor
C9, C10, C23	1 μF	Reference buffer capacitor
C11, C12, C13	1.5 nF	Signal filter capacitor
C8, C14, C18, C33,	10 μF	Power filter capacitor
C30	10 μF	Power input capacitor
C2, C4, C7, C15, C16, C17, C19, C20, C24, C32, C34	0.1 μF	Power filter capacitor
C21, C22, C25, C26	0.47 μF	Reference buffer capacitor
C27	4.7 μF	Reference buffer capacitor
C28, C29	10 nF	Signal filter capacitor
C5, C6	4.7 μF	Signal filter capacitor
FB1, FB2	Ferrite bead	Power line filter
R1, R8	2.2 Ω	Power line filter
R10	10 KΩ	Calibration resistor
R2, R3	51.1 KΩ	Filter resistor
R5, R7	100 KΩ	Protection resistor
R6	1 MΩ	Feedback resistor
R9	10 KΩ	Protection resistor
R11, R12	10 KΩ	Bias resistor
U1	ADS1292RIRSMT	Electrophysiology front end IC
U2	AD5941BCPZ	Impedance and electrochemistry front end IC
U3	ADG839YKSZ-REEL7	Multiplexer IC
U4	LP5907SNX-3.3_NOPB	Power regulator IC
U5	HJ-180MH	Bluetooth and controller IC

IC: integrated circuit

2.10 References

1. G. Zhao, Y. Ling, Y. Su, Z. Chen,; C. Mathai,; O. Emeje, A. Brown, D. Alla, J. Huang,C. Kim, Q. Chen, X. He, D. Stalla; Y. Xu, Z. Chen, P. Chen, S. Gangopadhyay, J. Xie, Z. Yan, Laser-Scribed Conductive, Photoactive Transition Metal Oxide on Soft Elastomers for Janus On-Skin Electronics and Soft Actuators. *Sci. Adv.* **8**, eabp9734

(2022).

2. J. Lin, Z. Peng, Y. Liu, F. Ruiz-Zepeda, R. Ye, E. L. G. Samuel, M. J. Yacaman, B. I. Yakobson, J. M. Tour, Laser-induced porous graphene films from commercial polymers. *Nat. Commun*. **5**, 5714 (2014).

3. K. W. Tan, B. Jung, J. G. Werner, E. R. Rhoades, M. O. Thompson, U. Wiesner, Transient laser heating induced hierarchical porous structures from block copolymer-directed self-assembly. *Science* **349**, 54-58 (2015).

4. W. Gao, N. Singh, L. Song, Z. Liu, A. L. M. Reddy, L. Ci, R. Vajtai, Q. Zhang, B. Wei, P. A. Ajayan, Direct laser writing of micro-supercapacitors on hydrated graphite oxide films. *Nat. Nanotechnol*. **6**, 496-500 (2011).

5. M. F. El-Kady, V. Strong, S. Dubin, R. B. Kaner, Laser scribing of high-performance and flexible graphene-based electrochemical capacitors. *Science* **335**, 1326-1330 (2012).

6.X. Zang, C. Jian, T. Zhu, Z. Fan, W. Wang, M. Wei, B. Li, M. F. Diaz, F. Ashby, Z. Lu, Y. Chu, Z. Wang, X. Ding, Y. Xie, J. Chen, J. N. Hohman, M. Sanghadasa, J. C. Grossman, L. Lin, Laser-sculptured ultrathin transition metal carbide layers for energy storage and energy harvesting applications. *Nat. Commun*. **10**, 3112 (2019).

7. R. Ye, D. K. James, J. M. Tour, Laser-induced graphene: from discovery to translation. *Adv. Mater.* **31**, 1803621 (2019).

8. R. You, Y. Q. Liu, Y. L. Hao, D. D. Han, Y. L. Zhang, Z. You, Laser fabrication of graphene-based flexible electronics. *Adv. Mater*. **32**, 1901981 (2020).

9. Y. Xu, Q, Fei, M. Page, G. Zhao, Y. Ling, D. Chen, Z. Yan, Laser-induced graphene for bioelectronics and soft actuators. *Nano Res*. **14**, 3033-3050 (2021).

10. Y. Yang, Y. Song, X. Bo, J. Min, O. S. Pak, L. Zhu, M. Wang, J. Tu, A. Kogan, H. Zhang, T. K. Hsiai, Z. Li, W. Gao, A laser-engraved wearable sensor for sensitive detection of uric acid and tyrosine in sweat. *Nat. Biotechnol*. **38**, 217-224 (2020).

11. D. H. Kim, N. Lu, R. Ma, Y. S. Kim, R. H. Kim, S. Wang, J. Wu, S. M. Won, H. Tao, A. Islam, K. J. Yu, T. I. Kim, R. Chowdhury, M. Ying, L. Xu, M. Li, H. J. Chung, H. Keum, M. Mccormick, P. Liu,Y. W. Zhang, F. G. Omenetto, Y. Huang, T. Coleman, J. A. Rogers, Epidermal electronics. *Science* **333**, 838-843 (2011).

12. D. C. Kim, H. J. Shim, W. Lee, J. H. Koo, D. H. Kim, Material-based approaches for the fabrication of stretchable electronics. *Adv. Mater*. **32**, 1902743 (2020).

13. Y. Ling, W. Pang, X. Li, S. Goswami, Z. Xu, D. Stroman, Y. Liu, Y. Xu, G. Zhao, B. Sun, J. Xie, G. Huang, Y. Zhang, Z. Yan, Laser-induced graphene for

electrothermally controlled, mechanically guided, 3D assembly and human-soft actuators interaction. *Adv. Mater*. **32**, 1908475 (2020).

14. B. Sun, R. N. McCay, S. Goswami, Y. Xu, C. Zhang, Y. Ling, J. Lin, Z. Yan, Gas-permeable, multifunctional on-skin electronics based on laser-induced porous graphene and sugar-templated elastomer sponges. *Adv*. *Mater*. **30**, 1804327 (2018).

15. Y. Gao, Q. Li, R. Wu, J. Sha, Y. Lu, F. Xuan, Laser direct writing of ultrahigh sensitive SiC-based strain sensor arrays on elastomer toward electronic skins. *Adv*. *Funct*. *Mater*. **29**, 1806786 (2019).

16. V. Nair, J. Yi, D. Isheim, M. Rotenberg, L. Meng, F. Shi, X. Chen, X. Gao, A. Prominski, Y. Jiang, J. Yue, C. T. Gallagher, D. N. Seidman, B. Tian, Laser writing of nitrogen-doped silicon carbide for biological modulation. *Sci*. *Adv*. **6**, eaaz2743 (2020).

17. D. B. Rogers, R. D. Shannon, A. W. Sleight, J. L. Gillson, Crystal chemistry of metal dioxides with rutile-related structures. *Inorg. Chem*. **8**, 841-849 (1969).

18. T. Lüdtke, D. Wiedemann, I. Efthimiopoulos, N. Becker, S. Seidel, O. Janka, R. Pöttgen, R. Dronskowski, M. Koch-Müller, M. Lerch, HP-MoO2: a high-pressure polymorph of molybdenum dioxide. *Inorg. Chem*. **56**, 2321-2327 (2017).

19. K. Dou, W. Zhu, Y. Zou, Y. Gu, J. Li, S. Zhang, Z. Liu, H. Zeng, Metallic oxide nanocrystals with near-infrared plasmon resonance for efficient, stable and biocompatible photothermal cancer therapy. J. *Mater. Chem. B* **5**, 7393-7402 (2017).

20. Y. Zhan, Y. Liu, H. Zu, Y. Guo, S. Wu, H. Yang, Z. Liu, B. Lei, J. Zhuang, X. Zhang, D. Huang, C. Hu, Phase-controlled synthesis of molybdenum oxide nanoparticles for surface enhanced Raman scattering and photothermal therapy. *Nanoscale* **10**, 5997-6004 (2018).

21. C. Hao, C. Wei, Y. Wang, Z. Sun, H. Liu, R. Dai, M. Huang, S. He, W. Liu, C. Zhu, Thermal/near-infrared light dual-responsive reversible two-way shape memory cEVA/2D-MoO_2 composite for multifunctional applications. *Macromol*. *Rapid*. *Commun* **42**, 2100056 (2021).

22. Y. Shi, B. Guo, S. A. Corr, Q. Shi, Y. S. Hu, K. R. Heier, L. Chen, R. Seshadri, G. D. Stucky, Ordered mesoporous metallic MoO_2 materials with highly reversible lithium storage capacity. *Nano Lett*. **9**, 4215-4220 (2009).

23. Y. Jin, H. Wang, J. Li, X. Yue, Y. Han, P. K. Shen, Y. Cui, Porous MoO_2 nanosheets as non-noble bifunctional electrocatalysts for overall water splitting. *Adv. Mater*. **28**, 3785-3790 (2016).

24. Q. Zhang, X. Li, Q. Ma, Q. Zhang, H. Bai, W. Yi, J. Liu, J. Han, G. Xi, A metallic molybdenum dioxide with high stability for surface enhanced Raman spectroscopy. *Nat*. *Commun*. **8**, 14903 (2017).

25. C. K. N. Patel, Continuous-wave laser action on vibrational-rotational transitions of CO_2. *Phys. Rev*. **136**, A1187-A1193 (1964).

26. Y. Xu, B. Sun, Y. Ling, Q. Fei, Z. Chen, X. Li, P. Guo, N. Jeon, S. Goswami, Y. Liao, S. Ding, Q. Yu, J. Lin, G. Huang, Z. Yan, Multiscale porous elastomer substrates for multifunctional on-skin electronics with passive-cooling capabilities. *Proc. Natl. Acad. Sci. U. S. A*. **117**, 205-213 (2020).

27. B. Hu, L. Mai, W. Chen, F. Yang, From MoO_3 nanobelts to MoO_2 nanorods: structure transformation and electrical transport. *ACS Nano* **3**, 478-482 (2009).

28. Y. Chyan, R. Ye, Y. Li, S. P. Singh, C. J. Arnusch, J. M. Tour, Laser-induced graphene by multiple lasing: toward electronics on cloth, paper, and food. ACS *Nano* **12**, 2176-2183 (2018).

29. L. Tian, B. Zimmerman, A. Akhtar, K. J. Yu, M. Moore, J. Wu, R. J. Larsen, J. W. Lee, J. Li, Y. Liu, B. Metzger, S. Qu, X. Guo, K. E. Mathewson, J. A. Fan, J. Cornman, M. Fatina, Z. Xie, Y. Ma, J. Zhang, Y. Zhang, F. Dolcos, M. Fabiani, G. Gratton, T. Bretl, L. J. Hargrove, P. V. Braun, Y. Huang, J. A. Rogers, Large-area MRI-compatible epidermal electronic interfaces for prosthetic control and cognitive monitoring. *Nat*. *Biomed*. *Eng*. **3**, 194-205 (2019).

30. N. Driscoll, B. Erickson, B. B. Murphy, A. G. Richardson, G. Robbins, N. V. Apollo, G. Mentzelopoulos, T. Mathis, K. Hantanasirisakul, P. Bagga, S. E. Gullbrand, M. Sergison, R. Reddy, J. A. Wolf, H. I. Chen, T. H. Lucas, T. R. Dillingham, K. A. Davis, Y. Gogotsi, J. D. Medaglia, F. Vitale, MXene-infused bioelectronic interfaces for multiscale electrophysiology and stimulation. *Sci*. *Transl*. *Med*. **13**, eabf8629 (2021).

31. J. F. Schenck, The role of magnetic susceptibility in magnetic resonance imaging: MRI magnetic compatibility of the first and second kinds. *Med*. *Phys*. **23**, 815-850 (1996).

32. K. Muraleedharan, C. K. Subramaniam, N. Venkataramani, T. K. G. Rao, C. M. Srivastava, V. Sankaranarayanan, R. Srinivasan, On the magnetic-susceptibility of CuOx. *Solid State Commun*. **76**, 727-730 (1990).

33. T. R. Ray, J. Choi, A. J. Bandodkar, S. Krishnan, P. Gutruf, L. Tian, R. Ghaffari, J. A. Rogers, Bio-integrated wearable systems: a comprehensive review. *Chem*. *Rev*.

119, 5461-5533 (2019).

34. T. Someya, M. Amagai, Toward a new generation of smart skins. *Nat. Biotechnol.* **37**, 382-388 (2019).

35. S. Xu, A. Jayaraman, J. A. Rogers, Skin sensors are the future of health care. *Nature* **571**, 319-321 (2019).

36. L. C. Kloth, Electrical stimulation for wound healing: a review of evidence from in vitro studies, animal experiments, and clinical trials. *Int. J. Low. Extrem. Wounds* **4**, 23-44 (2005).

37. Y. Hosobuchi, J. E. Adams, R. Linchitz, Pain relief by electrical stimulation of the central gray matter in humans and its reversal by naloxone. *Science* **197**, 183-186 (1977).

38. G. Alon, A. F. Levitt, P. A. McCarthy, Functional electrical stimulation enhancement of upper extremity functional recovery during stroke rehabilitation: a pilot study. *Neurorehabil. Neural Repair* **21**, 207-215 (2007).

39. J. Kim, A. S. Campbell, B. E. F. de Ávila, J. Wang, Wearable biosensors for healthcare monitoring. *Nat. Biotechnol.* **37**, 389-406 (2019).

40. M. Bariya, H. Y. Y. Nyein, A. Javey, Wearable sweat sensors. *Nat. Electron.* **1**, 160-171 (2018).

41. K. Kwon, S. Y. Heo, I. Yoo, A. Banks, M. Chan, J. Y. Lee, J. B. Park, J. Kim, J. A. Rogers, Miniaturized, light-adaptive, wireless dosimeters autonomously monitor exposure to electromagnetic radiation. *Sci. Adv.* **5**, eaay2462 (2019).

42. Y. Jin, J. Wang, B. Sun, J. C. Blakesley, N. C. Greenham, Solution-processed ultraviolet photodetectors based on colloidal ZnO nanoparticles. *Nano Lett.* **8**, 1649-1653 (2008).

43. L. Lan, X. Le, H. Dong, J. Xie, Y. Ying, J. Ping, One-step and large-scale fabrication of flexible and wearable humidity sensor based on laser-induced graphene for real-time tracking of plant transpiration at bio-interface. *Biosens. Bioelectron.* **165**, 112360 (2020).

44. W. J. Pan, Y. Zhang, D. Z. Zhang, Self-assembly fabrication of titanium dioxide nanospheres-decorated tungsten diselenide hexagonal nanosheets for ethanol gas sensing application. *Appl. Surf. Sci.* **527**, 146781 (2020).

45. Z. Ma, P. Chen, W. Cheng, K. Yan, L. Pan, Y. Shi, G. Yu, Highly sensitive, printable nanostructured conductive polymer wireless sensor for food spoilage detection. *Nano Lett.* **18**, 4570-4575 (2018).

46. C. Shimamoto, I. Hirata, K. Katsu, Breath and blood ammonia in liver cirrhosis. *Hepatogastroenterology* **47**, 443-445 (2000).

47. S. E. Lukas, J. H. Mendelson, R. A. Benedikt, B. Jones, EEG alpha activity increases during transient episodes of ethanol-induced euphoria. *Pharmacol. Biochem. Behav*. **25**, 889-895 (1986).

48. V. M. Karpyak, M. Romanowicz, J. E. Schmidt, K. A. Lewis, J. M. Bostwick, Characteristics of heart rate variability in alcohol-dependent subjects and nondependent chronic alcohol users. *Alcohol. Clin. Exp. Res*. **38**, 9-26 (2014).

49. S. I. Rich, R. J. Wood, C. Majidi, Untethered soft robotics. *Nat. Electron*. **1**, 102-112 (2018).

50. Z. Yan, F. Zhang, F. Liu, M. Han, D. Ou, Y. Liu, Q. Lin, X. Guo, H. Fu, Z. Xie, M. Gao, Y. Huang, J. H. Kim, Y. Qiu, K. Nan, J. Y. Kim, P. Gutruf, H. Luo, A. Zhao, K. C. Hwang, Y. Huang, Y. Zhang, J. A. Rogers, Mechanical assembly of complex, 3D mesostructures from releasable multilayers of advanced materials. *Sci. Adv*. **2**, e1601014 (2016).

51. Y. Zhang, Z. Yan, K. Nan, D. Xiao, Y. Liu, H. Luan, H. Fu, X. Wang, Q. Yang, J. Wang, W. Ren, H. Si, F. Liu, L. Yang, H. Li, J. Wang, X. Guo, H. Luo, L. Wang, Y. Huang, J. A. Rogers, A mechanically driven form of Kirigami as a route to 3D mesostructures in micro/nanomembranes. *Proc. Natl. Acad. Sci. U. S. A*. **112**, 11757-11764 (2015).

52. Y. Xu, G. Zhao, L. Zhu, Q. Fei, Z. Zhang, Z. Chen, F. An, Y. Chen, Y. Ling, P. Guo, S. Ding, G. Huang, P. Y. Chen, Q. Cao, Z. Yan, Pencil-paper on-skin electronics. *Proc. Natl. Acad. Sci. U. S. A*. **117**, 18292-18301 (2020).

53. D. C. Marcano, D. V. Kosynkin, J. M. Berlin, A. Sinitskii, Z. Sun, A. Slesarev, L. B. Alemany, W. Lu, J. M. Tour, Improved synthesis of graphene oxide. *ACS Nano* **4**, 4806-4814 (2010).

54. P. Li, Y. F. Poon, W. Li, H. Y. Zhu, S. H. Yeap, Y. Cao, X. Qi, C. Zhou, M. Lamrani, R. W. Beuerman, E. T. Kang, Y. Mu, C. M. Li, M. W. Chang, S. S. J. Leong, M. B. Chan-Park, A polycationic antimicrobial and biocompatible hydrogel with microbe membrane suctioning ability. *Nat. Mater*. **10**, 149-156 (2011).

Chapter 3. Phase-Separated Porous Nanocomposite with Ultralow Percolation Threshold Enables Strain-Resilient Wireless Stretchable Bioelectronics

This chapter is copied and reformatted from a paper published in *Nature Nanotechnology,* doi.org/10.1038/s41565-024-01658-6 (2024) (*1*).

Abstract: Realizing the full potential of stretchable bioelectronics in wearables, biomedical implants and soft robotics necessitates the development of conductive elastic composites that are intrinsically soft, highly conductive, and strain resilient. However, existing conductive elastic composites usually face compromises in electrical durability and performance owing to disruptions in conductive paths under strain. Additionally, they often contain large portions of conductive fillers to achieve desirable electrical conductivity as a result of high percolation thresholds. In this work, we present an in-situ phase separation method, which can facilitate microscale silver nanowire assembly and create self-organized percolation networks on pore surfaces. The resultant phase-separated porous nanocomposites are highly conductive, strain-insensitive, fatigue-tolerant, and economize on conductive filler use. Their resilience is rooted in multiscale porous polymer matrices that dissipate stress and rigid conductive fillers that adapt to strain-induced geometry changes during stretching. Notably, the presence of porous microstructures reduces the percolation threshold (V_c=0.00062) by 48-fold and suppresses electrical degradation even under strains exceeding 600%. Theoretical calculations yield quantitatively consistent results with experimental findings. By pairing this composite material with near-field communication technologies, we have demonstrated stretchable wireless power and data transmission solutions that are ideal for both skin-interfaced and implanted

bioelectronics. The systems enable battery-free wireless powering and sensing of a breadth of sweat biomarkers-with less than 10% performance variation even at 50% strain. Ultimately, our strategy minimizes conductive filler use, enhances stretchability, and offers expansive material options for diverse applications.

3.1 Introduction

Soft elastic conductive composite materials that exhibit high electrical conductivity (*2, 3*), strain-insensitive performance (*4-6*), and skin-like mechanical compliance (*7-10*) are essential for next-generation soft robotics, skin-mounted and implanted devices (*11, 12*). They are pivotal in biomedical diagnostics, electronic skins, and human-machine interfaces (*13-16*). System-level bioelectronic devices, composed of soft sensors and rigid electronic components (*11, 17*), demand breathable sensors and strain-resilient conductors that offer exceptional mechanical tolerance. Present enabling technologies utilize conductive fillers dispersed in elastomer matrices, spanning from zero-dimensional nanoparticles, one-dimensional nanowires/nanotubes, to two-dimensional nanosheets (*13, 14*). While liquid metal particle-based composites established a viable solution, their susceptibility to leakage under external deformations, necessity of high loadings, and inevitable interface corrosion of electronic components over prolonged exposure pose challenges (*18, 19*).

Given percolation theory, metal nanowires with high aspect ratio are preferred over other fillers to achieve highly conductive composites because they considerably reduce the percolation threshold (*13*). Recent endeavors span from the fabrication of silver nanowires (Ag NWs) nanocomposites with notable electrical conductivity to ultrathin nanomembrane with facile patternability (*2, 3*). Nonetheless, persistent challenges remain, including the pronounced coupling between electrical resistance and tensile stretching, rapid degradation in cyclic fatigue test, tedious ligand exchange process, and the necessity for a substantial filler loading (60-80% by weight) to achieve desired electrical conductivity. Minimizing the metallic filler use is essential to achieve cost-effectiveness, reduce macroscopic stiffness, and enhance stretchability. In addition, macroscale stretching of nanocomposites generally results in diminished overlap of

conductive percolation pathways, thereby compromising their electrical performance. Strain-induced self-organization and rearrangement of the conductive fillers within the polymer matrices represents a promising strategy (*20-22*), yet the synthesis and separation of fillers from the polymer at microscale level are fundamentally challenging.

Porous elastomer conductors, characterized by high breathability, ultra-softness, and large surface area, can find wide applications in stretchable electronics, energy storage, and separation, among others (*10, 23-25*). Various techniques, such as hard-templating, freeze-drying, emulsion, breath figure methods, and electrospinning, have been employed to introduce porous structures into polymer matrices (*25, 26*). Porous Ag NWs elastomer composites with notable breathability has also been achieved (*27-28*). However, these methods often yield materials with significant electrical-mechanical coupling (i.e., strain-induced electrical conductance change), limiting their applications in strain-resilient stretchable electronics. In addition, phase-separation-based methods have gained considerable attention due to their ability to generate interconnected and tunable porous structures in polymers without the requirement of templates, while also being simple, cost-effective, and scalable (*29, 30*). Recently, this technique has been applied to prepare porous elastomeric materials for various applications, including thermal management, sensing, catalysis, energy storage, and water purification (*24, 29, 31*). Furthermore, phase separation has been applied to produce porous conductors by embedding conductive fillers within polymer matrices. However, these materials usually lack the necessary properties for stretchable bioelectronics, such as strain-insensitive features (*24, 32*).

Here, we report a one-step, in situ phase separation of Ag NWs from porous polyurethane (PU) matrices (**Figure 3.1**). Phase separation facilitates microscale

assembly of Ag NWs, forming self-organized percolation networks on pore surfaces. This results in an electrically conductive phase-separated porous Ag NWs nanocomposite (PSPN) with extremely low percolation thresholds and strain-insensitive electrical properties.

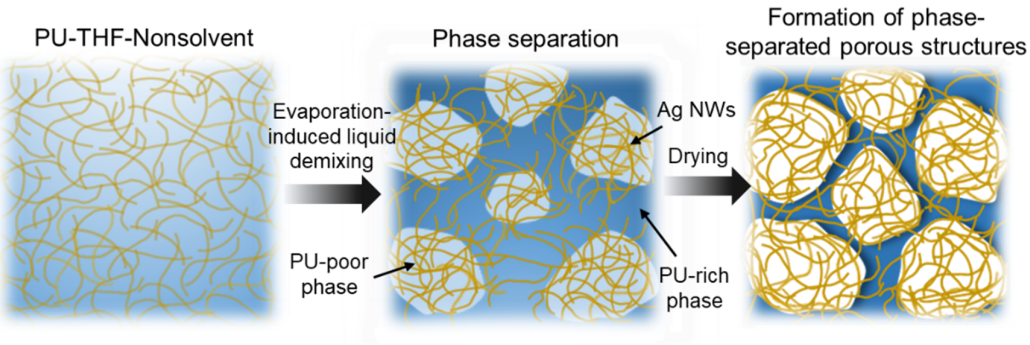


Figure 3.1. Schematic illustration of a cross-sectional view of the phase-separation process. The initial casting solution, composed of the solvent, nonsolvent, and polymer, forms a homogeneous solution (left). Subsequently, phase separation initiates due to the evaporation of the volatile solvent and nonsolvent, which results in the separation of the PU-rich and PU-poor (Ag NWs rich) phase (middle). Finally, liquid-liquid demixing process generates co-continuous phases in three dimensions, completed by coarsening that creates continuous porous structures within the PU matrices (right).

The stable electrical conductivity arises from the synergy of energy-dissipative porous PU microstructures and adaptable Ag NWs conductive pathways, maintaining effective electron transport even under significant macroscopic strain (**Figure 3.2 B, C**). We demonstrate simultaneous accomplishment of electrical-mechanical decoupling, ultralow percolation thresholds, and remarkable electrical conductivity despite the low Ag NWs volume fractions. This strategy also eliminates the ligand-exchange process typically required for the fabrication of Ag NWs-based elastomer composites due to its inherent immiscibility with these elastomers. Leveraging these unique attributes, we pair our PSPN with near field communication (NFC)-based technologies to achieve wireless power delivery and data transmission for skin-

interfaced and implantable bioelectronic devices.

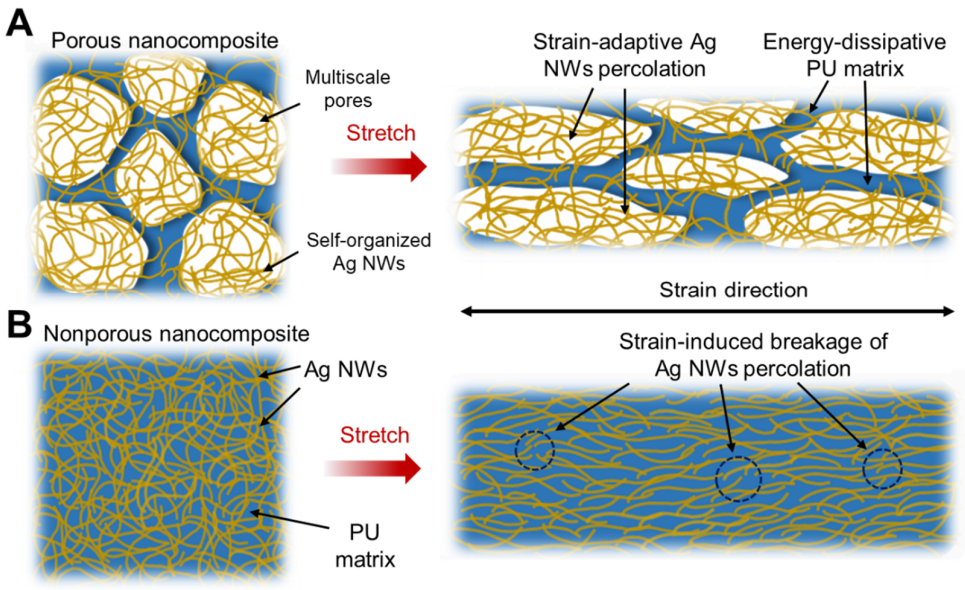


Figure 3.2. Schematic illustration of porous (**A**) and nonporous (**B**) Ag NWs nanocomposites at original (left) and stretched (right) states.

3.2 Fabrication of PSPN and theoretical prediction

The fabrication of PSPN begins with the preparation of a precursor solution containing polymer solution (PU in tetrahydrofuran, THF) and conductive filler solution (Ag NWs in ethanol). During the subsequent dry-casting process, phase separation initiates due to the evaporation of the volatile solvent (THF) and nonsolvent (ethanol). This results in the separation of the PU-rich and PU-poor phase. Ag NWs with amphiphilic ligands (e.g., polyvinyl pyrrolidone) reside in the PU-poor phase due to immiscibility between Ag NWs and PU solution. The liquid-liquid demixing process generates co-continuous phases in three dimensions, completed by coarsening that creates continuous porous structures within the PU matrices. **Figure 3.1** presents a 2D cross-sectional view of the phase separation process. This process can be elucidated by examining the trajectory of the compositional path of the nanocomposite

solution within the phase diagram (**Figure 3.3**) (*29, 30, 33, 34*). In brief, the initial casting solution, composed of the solvent, nonsolvent, and polymer, forms a homogeneous solution. Upon the evaporation of solvent and nonsolvent, the trajectory of the composition path crosses the binodal and spinodal, entering the unstable region where liquid-liquid demixing occurs (two phases). The spinodal decomposition reduces the free energy of the system through diffusion and fluid flow or convection. Such mass transfer leads to the formation of bicontinuous porous structures.

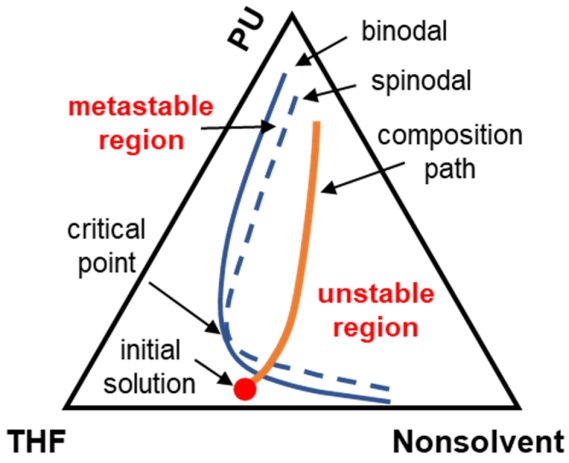


Figure 3.3. Schematic illustration of the isothermal ternary phase diagram of polymer, solvent, and nonsolvent (i.e., PU, THF, and ethanol). The composition path in the phase diagram illustrates the trajectory of the multi-component system as it transitions across various phases due to the evaporation of the solvent and nonsolvent. The initial solution represents the composition of the original casting solution at the outset of this process.

The pore sizes are therefore tunable by changing the nonsolvent content (**Figure 3.4** and **Figure 3.5**). Throughout this process, Ag NWs initially self-organize closely on the pore surfaces, gradually forming strain-adaptive percolation networks as characterized by an increasing number of nanowires. The microscopic-level self-assembly of Ag NWs, guided by the presence of micro-sized pores, is driven by minimizing the free energy to stabilize the system (i.e., Pickering effect) (*35*).

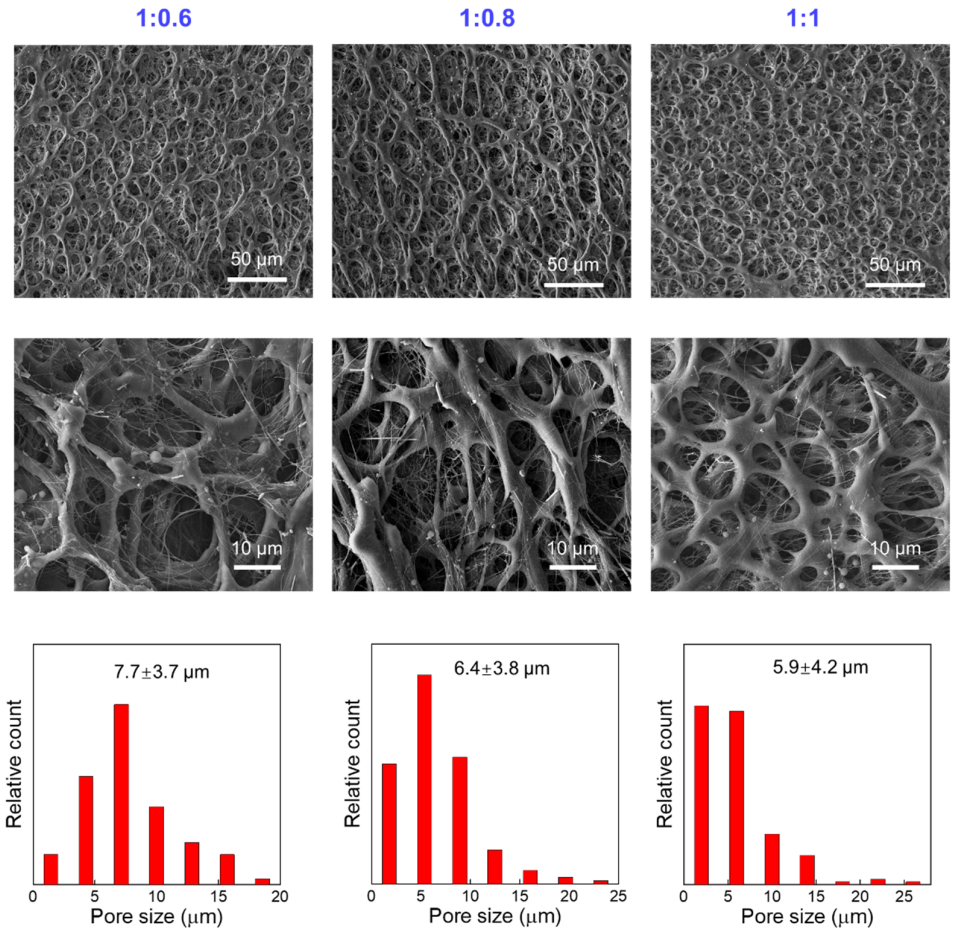


Figure 3.4. SEM images and corresponding particle size distributions of PSPN. Here, 1 ml of PU solution (70 mg ml^{-1} in THF) and 0.4 ml of Ag NWs solution (20 mg ml^{-1} in ethanol) were first mixed, followed by the addition of ethanol (0.2, 0.4, and 0.6 ml) to vary the nonsolvent content. Quantitative analysis indicates that the pore size slightly decreases with the increase of ethanol volume content.

Conductive nanocomposites are generally made by uniformly dispersing conductive filler materials within soft elastomer matrices, where these nanomaterials establish conductive percolation networks (i.e., multiple continuous electron transport paths) once a critical density is reached (*13*). For example, strain-induced rupture of Ag NWs percolation networks typically occurs upon macroscopic stretching (*20*) (**Figure 3.2B**). In the presence of an energy dissipative porous microstructures, on the contrary, soft polymer matrices alter the deformation, accommodate the mechanical strain, and

dissipate local stress, whereas strain-adaptive Ag NWs percolation pathways adapt to such structural change due to significant mechanical mismatch and therefore preserve interconnected conductive networks (**Figure 3.2A**).

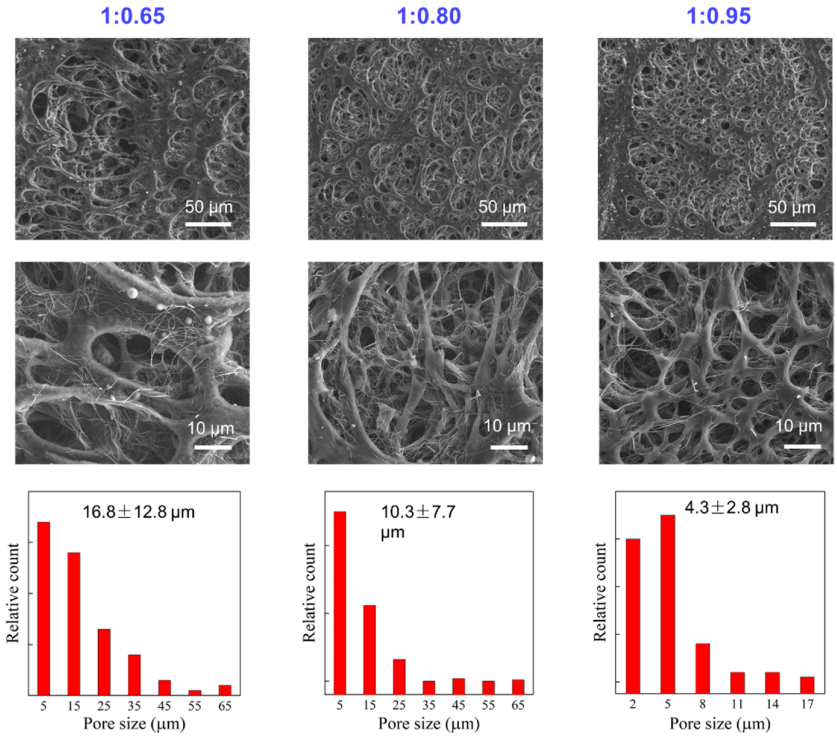


Figure 3.5. SEM images and corresponding particle size distributions of PSPN with 1-butanol. Here, we introduced 1-butanol as co-nonsolvent to tune the pore size. Specifically, 1 ml of PU solution (70 mg ml^{-1} in THF) and 0.4 ml of Ag NWs solution (20 mg ml^{-1} in ethanol) were first mixed, followed by the additions of 1-butanol (0.25, 0.4, and 0.55 ml). Quantitative analysis indicates that the pore size decreases while porosity increases (49.3%, 63.2%, 64.8%) with the increase of co-nonsolvent volume content.

Figure 3.6A, PSPN exhibits a marginal increase in electrical resistance across a broad range of uniaxial strains, whereas conventional nonporous nanocomposite experiences a rapid resistance increase, followed by an abrupt electrical failure owing to the development and propagation of microscopic cracks within conductive Ag NWs networks. This noticeable disparity signifies a considerably improved stretchability in the porous nanocomposites, showcasing exceptional electrical-mechanical decoupling.

Furthermore, we apply theoretical calculation based on three-dimensional (3D) percolation theory (*36*) to correlate the percolation threshold V_c (i.e., minimum number

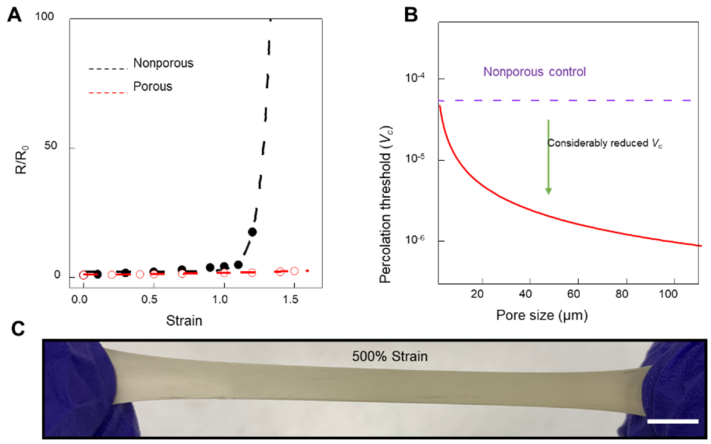


Figure 3.6. A, Numerical calculation of evolutions of electrical resistances as a function of applied strain on nonporous (black) and porous (red) nanocomposites. Dashed lines depict the exponentially fitted data. **B**, Theoretical calculation of percolation thresholds for nonporous (purple) and porous (red) Ag NWs nanocomposites, demonstrating its dependency on pore sizes. **C**, Optical photograph of a 500% stretched, free-standing PSPN. Scale bar, 1 cm.

of conductive fillers required to create conductive pathways) with pore size D_p of the polymer matrix when Ag NWs are homogeneously distributed on the pore surface,

$$V_{P,c} = \frac{1.4093\pi d^2}{Vl} f(D_p)$$

where d and l are the diameter and length of the nanowire, V is the volume of the nanocomposite, $f(D_p)$ is the surface area of the porous microstructure as a function of pore size D_p. The presence of microscale porous structure results in a percolation threshold order of magnitude lower than that observed in nonporous nanocomposites (**Figure 3.6B**). Besides, the pore size D_p also influences the electrical conductivity of the porous composites. Despite the low volume fractions of conductive fillers, the PSPN obtained with high electrical conductivity and stretchability consistently aligns with the results of these numerical examinations (**Figure 3.6C**).

3.3 Strain-insensitive characteristics with ultralow percolation threshold

We experimentally demonstrated the self-assembly of Ag NWs at the interface of a continuous "solid-gas" phase as the concentration of Ag NWs increases (**Figure 3.6 A**,). Such selective distribution substantially reduces the volume fraction of conductive fillers required for continuous electron transport, in contrast to conventional nonporous nanocomposite where filler materials are nearly homogeneously distributed throughout the polymer. To understand the impact of porous microstructures on electrical properties, we quantitatively evaluated the electrical conductivity of PSPN and nonporous nanocomposite as a function of Ag NWs volume fractions. The data in **Figure. 3.7B** were fitted using 3D percolation theory (*37*). We observed a notable reduction in percolation threshold (V_c) from 0.02971 to 0.00131 (a factor of ~22) with the existence of porous microstructures (mean pore size, ~6.4 μm).

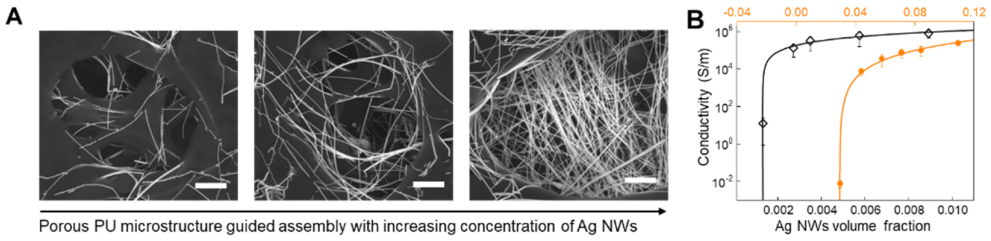


Figure 3.7. A, scanning electron microscope (SEM) micrographs of PSPN with increased Ag NWs concentrations, highlighting the PU microstructure-guided self-assembly of Ag NWs. Scale bars, 2 μm. **B**, Electrical conductivities of nonporous composite (orange) and PSPN (black, pore size, ~6.4 μm) as a function of Ag NWs volume fractions. Error bars represent standard deviations of six samples. Data are fitted using the 3D percolation theory.

Based on our theoretical analysis presented in **Figure 3.6B**, we empirically validated that the percolation threshold is influenced by pore size. We note that the addition of 1-butanol as co-nonsolvent allows broader control over pore sizes

compared with the porous nanocomposite made with ethanol, when varying the volumetric ratios between PU solution and Ag NWs solution (**Figure 3.4** and **Figure 3.5**). Furthermore, there was a 48-fold decrease in the threshold (V_c=0.00062) with an increase in pore size to ~16.8 μm (**Figure 3.8**) compared to nonporous nanocomposites. To the best of our knowledge, this is the lowest value ever reported. The electrical conductivity differs depending on Ag NWs volume fractions, reaching an optimum value of ~642,000 S m^{-1} ($V_{Ag\ NWs}$= ~0.007) after cold welding with saturated sodium chloride or sodium borohydride solution.

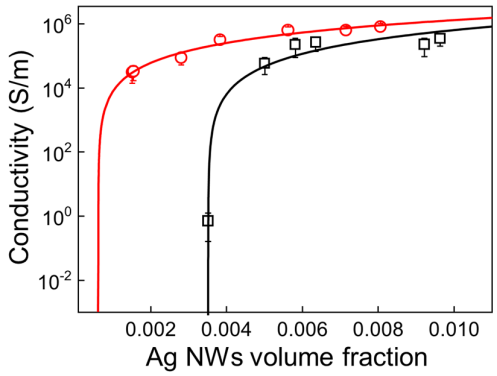


Figure 3.8. Percolation thresholds of PSPN with 1-butanol. Electrical conductivities of PSPN with 1-butanol with tunable pore sizes (red circle, ~16.8 μm; black square, ~4.3 μm) as a function of Ag NWs volume fractions. Error bars represent standard deviations of six samples. Data are fitted using the 3D percolation theory. This experimental observation aligns with our theoretical analysis presented in Fig. 1f, indicating that the percolation threshold is influenced by pore size. Specifically, there were a 48-fold (V_c=0.00062) and 8.5-fold (V_c=0.00351) decrease in the threshold compared with nonporous nanocomposite (**Figure 3.7B**) when the pore size was changed to ~16.8 and ~4.3 μm.

The PSPN comprises randomly distributed Ag NWs confined within the porous polymer matrices. The Ag NWs establish conductive percolation networks, effectively bridging interconnected pores across multiple scales (**Figure 3.9A**, left). The significant mechanical mismatch in Young's modulus between soft PU elastomer (~16 MPa) and rigid Ag NWs (~83 GPa) generates anisotropic regions with different

elasticity. Upon stretching, local stress dissipation is achieved through autonomous structural alternation of the soft PU elastomer, while the strain-adaptive Ag NWs retain the original percolation networks with minimally altered orientation due to their intrinsic rigidity (**Figure 3.9A**, middle and right). As a result, this enables delayed electrical failure (>600%), and notably stabilized electrical resistance under large uniaxial (R/R_0=1.5 at 100% and 20.2 at 500%; **Figure 3.9B**, and **Figure 3.9C**), biaxial strains, and bending (**Figure 3.9D, E**).

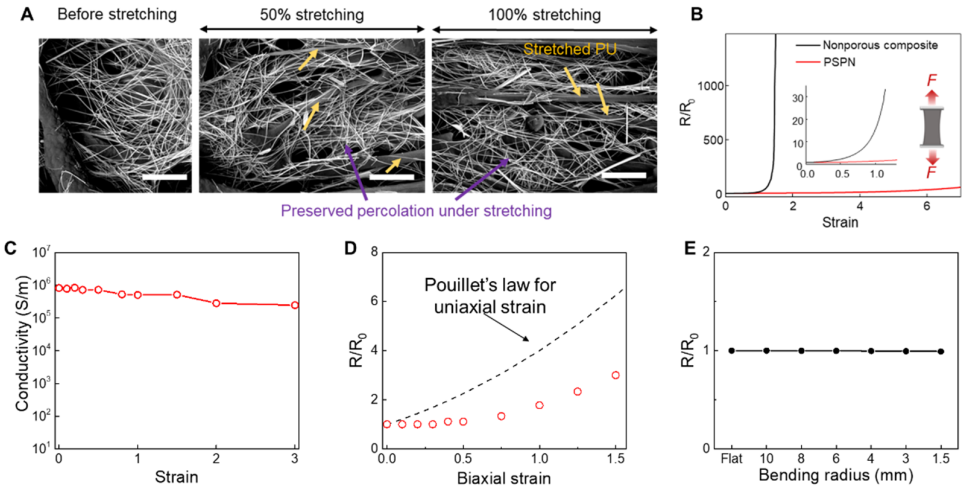


Figure 3.9. A, SEM images of PSPN before (left) and after stretching (middle, 50%; right, 100%). Upon stretching, local stress is dissipated through autonomous structural alternation (yellow arrow) of the porous PU matrices, while strain-adaptive Ag NWs retain the original percolation networks with minimally altered orientation (purple arrow) due to their intrinsic rigidity. Scale bars, 5 μm. **B**, Relative resistance change (R/R_0) of nonporous (black) and porous (red) Ag NWs nanocomposites as a function of uniaxial strains. **C**, Conductivity-strain characteristics of the phase-separated porous Ag NWs nanocomposite. Electromechanical performance of PSPN under biaxial stretching (**D**) and bending (**E**). Pouillet's law [$R/R_0 = (1+\varepsilon)^2$] that assumes a classical incompressible, constant-conductivity bulk conductor under strain was plotted as a comparison.

In contrast, electrical failure in nonporous nanocomposites occurs at an early stage (~100%), primarily because they lack energy-dissipative porous microstructures,

resulting in the rupture of percolation pathways (**Figure 3.10**).

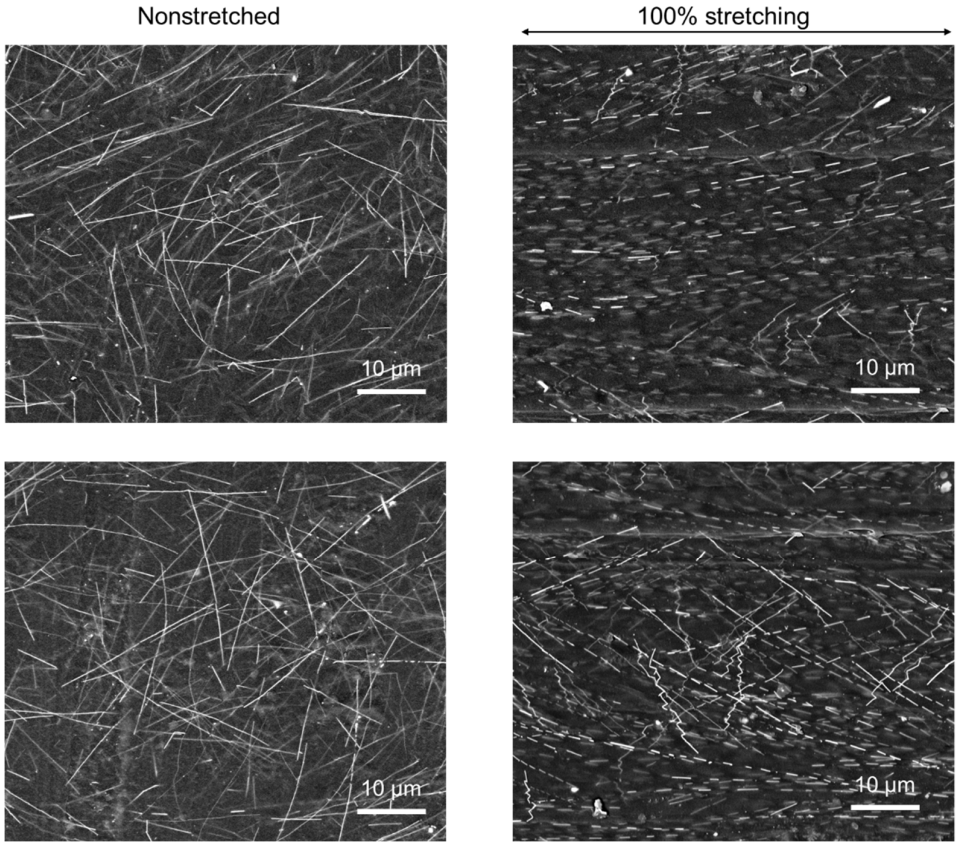


Figure 3.10. SEM images of nonporous Ag NWs nanocomposite before (left) and after (right) 100% strain. The stretched sample exhibits evident breakage of Ag NWs percolation networks and therefore leads to substantially reduced electrical conductivity.

In **Figure 3.11A**, we compared the evolution of electrical resistance of PSPN with other representative materials. Remarkably, our porous conductor exhibits substantially smaller variations in resistance compared to a variety of porous and nonporous composites. Furthermore, our porous conductor exhibits outstanding durability and reliability, as evidenced by a slight resistance change (R/R_0 =5.4) after cyclic stretching of 50% for 10,000 cycles, in evident contrast to that of the nonporous control (R/R_0 =262, **Figure 3.11B**). The susceptibility to fatigue-induced electrical performance degradation in the nonporous nanocomposite aligns with previous

findings on Ag flakes/nanoparticles, which deteriorates abruptly with increased stretching cycles (*5*). Such exceptionally durable performance of the porous nanocomposite can also be extended to larger strains (**Figure 3.11C**).

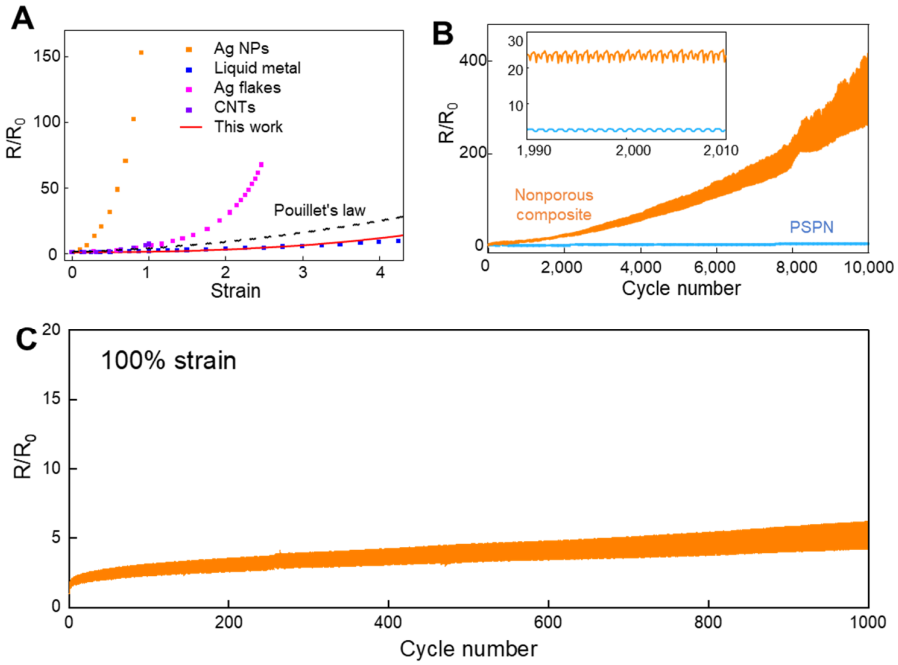


Figure 3.11. A, Comparison of electromechanical characteristics with other reported elastic conductors (38-41). **B**, Relative resistance changes of nonporous (orange) and porous (blue) nanocomposites subjected to cyclic stretching (50% maximum strain) for 10000 cycles. Inset shows magnified resistance variations over a 20-cycle period. **C**, Relative resistance changes of the phase-separated porous Ag NWs nanocomposites subjected to cyclic stretching (100% maximum strain) for 1000 cycles.

We also demonstrate its resilience to various damage scenarios, including puncturing with a scalpel knife, impact loading from a hammer strike, twisting and bending (**Figure 3.12A**) and multiple washing cycles (**Figure 3.12B**). This outstanding performance can be attributed to the energy-dissipating porous PU microstructures, which dampen external mechanical impacts, and the robust interface formed by hydrogen bonding between Ag NWs and PU (**Figure 3.12C, D**) (10). Besides, the multiscale interconnected cellular structure enables enhanced porosity and

breathability to facilitate skin perspiration and improve long-term biocompatibility. We note a substantial increase in water vapor transmission rate (WVTR) from ~615 to ~4,424 g m^{-2} day^{-1} and reduction in Young's modulus from ~9.1 to ~1.6 MPa when the

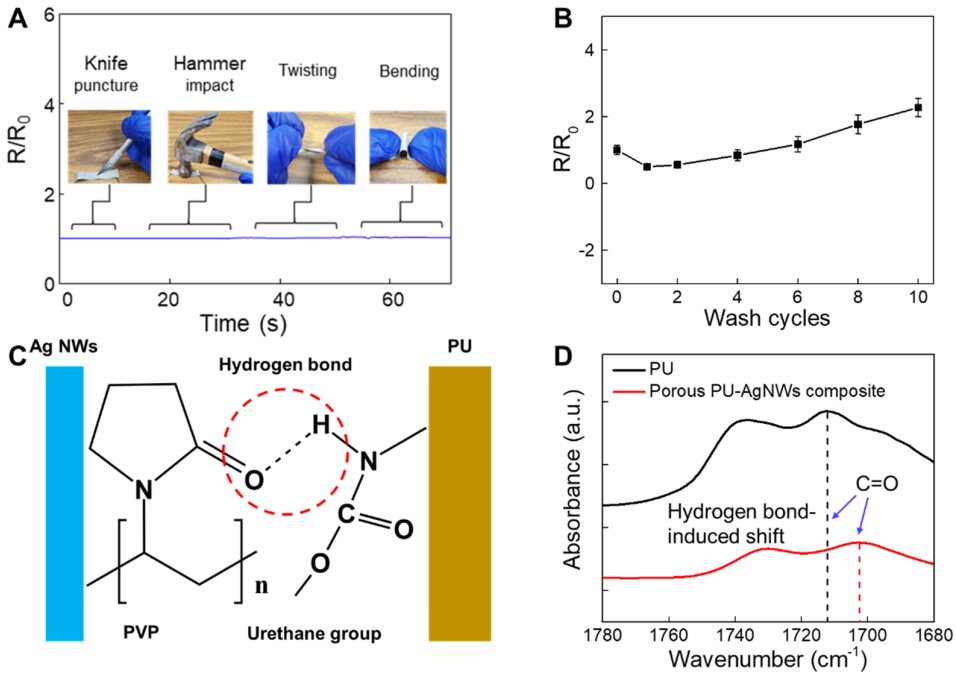


Figure 3.12. A, Demonstration of PSPN resilience to punctures from a scalpel knife, hammer impact, twisting, and bending and washing cycles (**B**). The decrease of resistance in the first cycle is attributed to the soap added in the solution, which resulted in autocatalytic addition of dissolved silver ions to the nanowire junction (*42*) (Error bars represent standard deviations of three samples). **C**, Schematic of hydrogen bonding between the amphiphilic ligand (PVP) and PU. **D**, A comparison of Fourier-transform infrared spectroscopy (FTIR) spectra on PU matrix (black), and PSPN (red). The peak of the carbonyl group shifted to smaller wavenumbers, indicating the formation of hydrogen bonding (*10*).

phase-separated microscale porosity is present in the polymer matrices (**Figure 3.13**). Given that the material's elastic modulus E scales with its density ρ, $E/E_s \propto (\rho/\rho_s)^n$ (*43*), where the power (n) is associated with the porous material's nano/microstructures, we attribute the increased softness to the multiscale nano- and microstructures. This feature promotes a compliant interface with biological tissues (*44*).

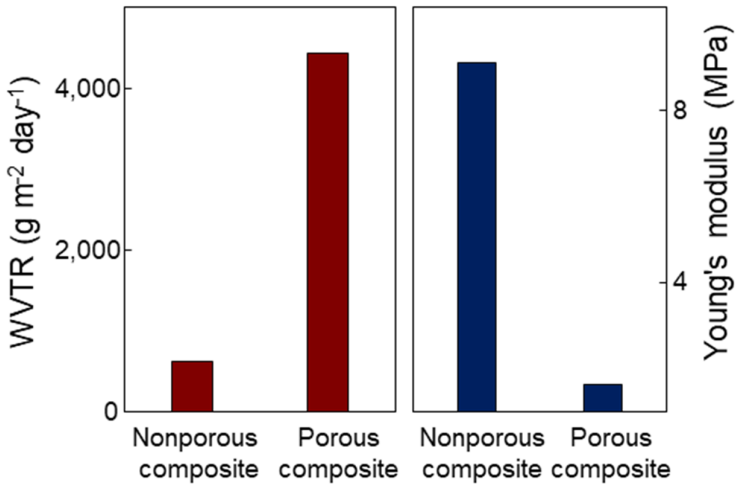


Figure 3.13. Demonstration of water vapor transmission rate (WVTR, left) and Young's modulus (right) of nonporous nanocomposites and PSPN, illustrating substantial increase in breathability and reduction in modulus with the presence of porous microstructures.

3.4 Radiofrequency properties of PSPN spiral coils under tensile strain

Wireless power delivery is emerging in the realm of wearable and soft electronics, as it makes it possible to wirelessly power wearable and implantable devices, eliminating the use of batteries (*45-47*). However, providing a stable and sustainable power supply that doesn't interfere with dynamic human motions or cause discomfort remains challenging. Taking advantage of the outstanding electrical conductivity and strain-insensitive feature, we fabricate stretchable spiral coils using our PSPN and implement in a radiofrequency (RF) wireless power transfer (WPT) system. **Figure 3.14A** shows the two-port network model of the WPT system, as well as the magnetic field distribution of the transmitter and receiver coils under RF excitation. The power transfer efficiency η is given by:

$$\eta = \frac{|S_{21}|^2}{1 - |S_{11}|^2}$$

where S_{21} and S_{11} are the transmission and reflection coefficients of the two-port

network. To evaluate the applicability of the PSPN coils in stretchable wireless communication technology, we first theoretically examined the magnetic field distribution using Ansys Maxwell simulation (**Figure 3.14B**). Given their identical dimensions and electrical resistances, the two spiral coils made of porous and nonporous nanocomposites exhibit comparable performances in unstretched states.

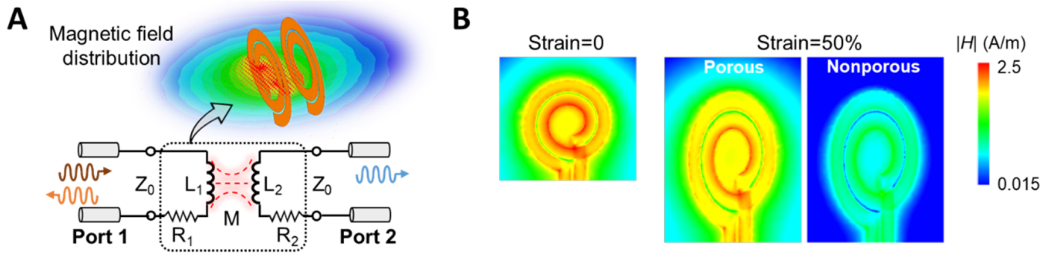


Figure 3.14. A, Two-port network model of the stretchable wireless power transfer system with the corresponding magnetic field distribution. **B**, Numeric simulations of magnetic field distributions of the porous and nonporous nanocomposites under 50% strain.

While being stretched at 50% strain, there is negligible change in our porous nanocomposites, in sharp contrast to the significant reduction of the magnetic field in the nonporous one. This is ascribed to the stable electrical resistance and inductance of PSPN coils under strain (**Figure 3.15A** and **B**,) stemming from the energy-dissipative porous PU microstructures.

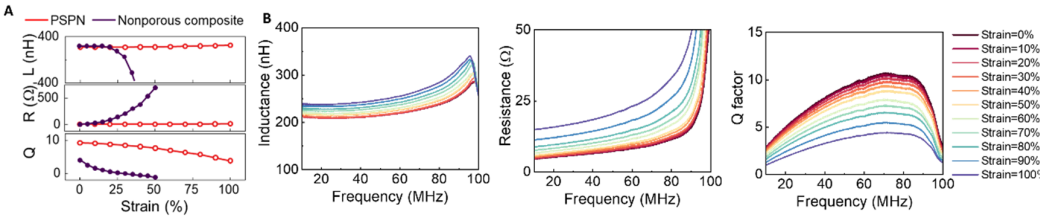


Figure 3.15. A, Two Inductance L, resistance R, and quality factor Q of porous (red circle) and nonporous (naval solid) nanocomposites at 50 MHz as functions of uniaxial tensile strains. **B**, Evolutions of inductance (left), resistance (middle), and Q factor (right) of the PSPN coil as functions of frequency under various strain.

Additionally, shown in **Figure 3.16**, the PSPN coil also presented a stable electrical resistance and inductance of coils under various bending radii.

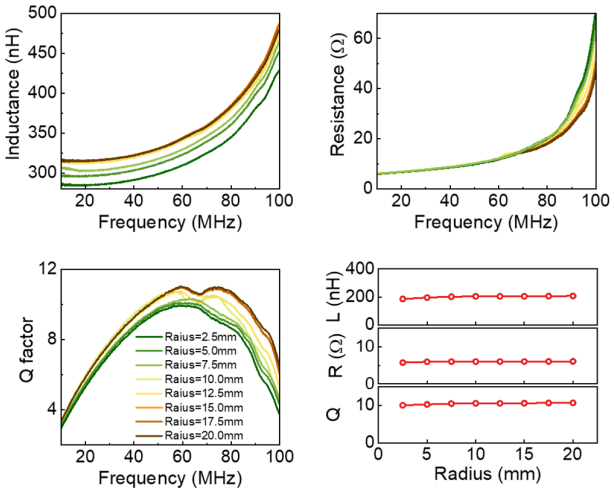


Figure 3.16. Variations of inductance, resistance, and Q factor of the PSPN coil under various bending radii.

Accordingly, we experimentally measured the variations of scattering parameters S_{11}, S_{21}, and the transfer efficiency η of the stretchable WPT system across uniaxial strains (**Figure 3.17A-C**). We note slight change in these parameters for up to 100% strain. Also, Advanced Design System (ADS) simulation indicates the strain-insensitive feature of the induced voltage on the stretchable PSPN coil (**Figure 3.17C** inset).

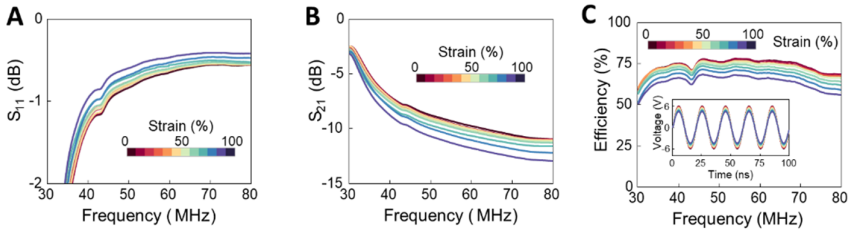


Figure 3.17. Scattering parameters S_{11} (**A**), S_{21} (**B**), and power transfer efficiency η (**C**) of the two-port wireless power transfer system comprising a primary transmitter coil and a stretchable receiver coil made from PSPN under strain. Inset in **C**, theoretical calculations of induced voltage on the stretchable receiver coil at 50 MHz under strain.

As shown in **Figure 3.18A**, the extracted transfer efficiency of the stretchable WPT system at 50 MHz reduces slightly from 76.0% to 74.8% at 50% strain and further to 66.6% at 100% strain. This arises primarily from the altered coupling strength caused by geometry changes between the two coils. Notably, our device outperformed Ag NWs nanofiber-based antenna, which drops from 35% to 15% at 100% strain (*48*). Conversely, the coils' efficiency for nonporous composite dropped sharply to 23.1% at 25% strain, with a total loss of power transfer capability by 50% strain (**Figure 3.18A-C**). As anticipated, a shorter distance between the coils notably boosts transfer efficiency due to an enhanced magnetic coupling (**Figure 3.18D**).

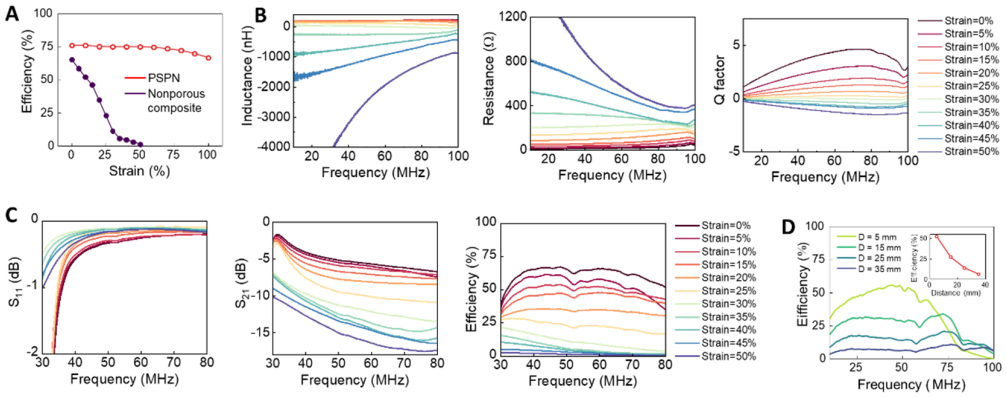


Figure 3.18. A, The evolutions of power transfer efficiency at 50 MHz of the PSPN (red circle) and nonporous nanocomposites (naval solid) as a function of tensile strain. **B,** Evolutions of inductance (left), resistance (middle), and *Q* factor (right) of the nonporous Ag NWs coil as functions of frequency under various strains. **C**, Scattering parameters S_{11} (left), S_{21} (middle), and efficiency (right) of the WPT system with conventional nonporous Ag NWs coil under various strains. **D**, Power transfer efficiency between the primary transmitter and porous nanocomposite receiver coils at various vertical distances. Extracted data at 50 MHz appears in the inset.

3.5 Strain-insensitive stretchable wireless powering system

NFC-based wireless powering and data transmission systems enable a myriad of new applications for wearable and implantable bioelectronic devices. Examples

include recordings of neurophysiological activity, biochemical sensing, neuromodulation, and pain management (*46, 49, 50*). These devices, however, rely on intrinsically rigid materials with limited stretchability (<30%), which falls short of meeting the strain tolerance requirement for certain skin-interfaced devices (>80%) (*51*). Given the exceptional electrical conductivity and electrically resilient property, we used our PSPN to fabricate wearable wireless power transmitters and implantable receivers. We first theoretically evaluated the transmitter coil's performance to power a device implanted in a body phantom, constructed from a glass cylinder filled with 1% agarose gel (**Figure 3.19A** and **B**). The phantoms with radii of 1.5, 3.5, or 5.5 cm simulate different body parts. Electromagnetic (EM) simulations reveal that the inherently soft and stretchable nanocomposite coil seamlessly adapts to curved body contours. This adaptability facilitates deeper penetration of EM power into the body, resulting in superior power delivery compared to its rigid counterparts (**Figure 3.19C** and **D**).

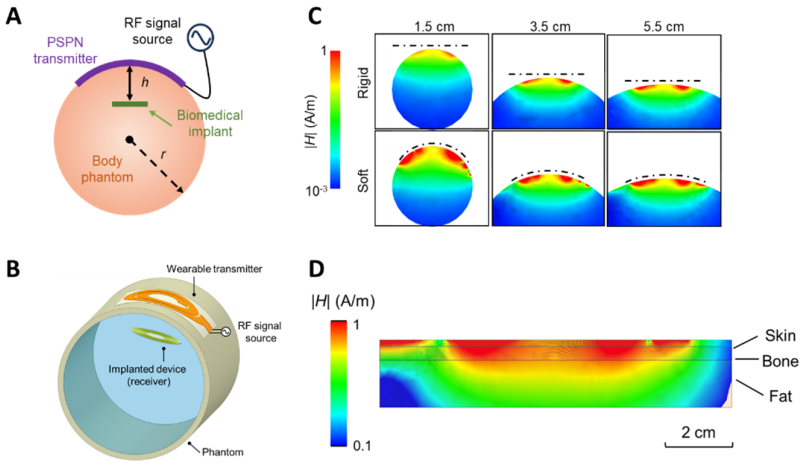


Figure 3.19. Schematic of a simplified structure (**A**) and setup phantom (**B**) used for measurements of coupling coefficient and transfer efficiency under strain. Maxwell simulations of magnetic field generated by a rigid (top) and soft transmitter (bottom) placed on body parts with various diameters (**C**) and Maxwell simulation of the magnetic field generated by a soft transmitter placed on flat human skin (**D**).

The coupling coefficient, κ, representing the fraction of magnetic flux between the transmitter and receiver coils, is given by

$$\kappa = \frac{M}{\sqrt{L_1 L_2}} = \frac{Im(Z_{12})}{\sqrt{Im(Z_{11})\, Im(Z_{22})}},$$

where M is the mutual inductance between the two coils, $Im(Z_{11})$, $Im(Z_{12})$, and $Im(Z_{22})$ are the imaginary components of the two-port network's impedance parameters. Experiments reveal that the coupling coefficient κ diminishes with increasing lateral and vertical separation between the coils (**Figure 3.20A**). As shown

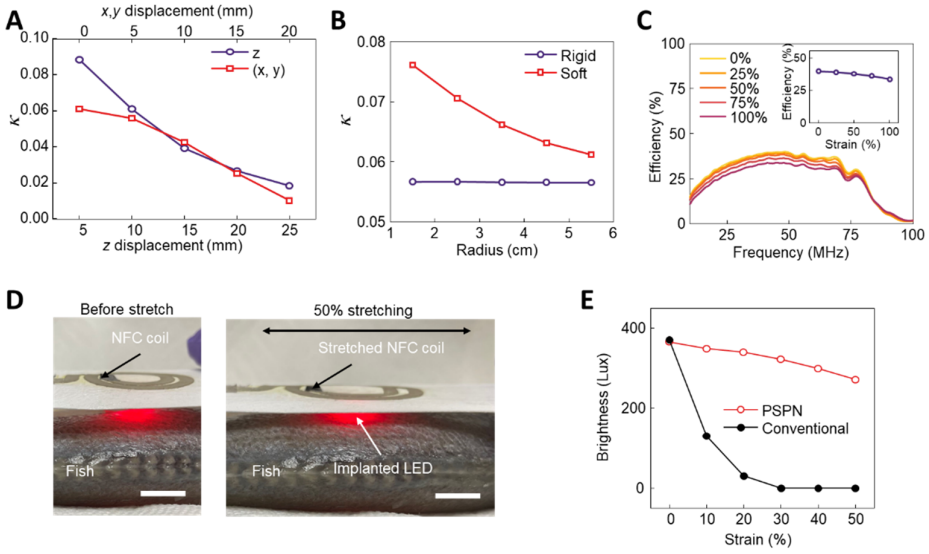


Figure 3.20. A, Coupling coefficient between the soft transmitter and implanted receiver coils with varied lateral (red) and vertical (naval) distances. **B,** Coupling coefficient between the soft PSPN (red) or rigid (naval) transmitter coil and the implanted receiver coil with varied phantom radii (h=1 cm). **C**, Transfer efficiency of the WPT system comprising the stretchable PSPN transmitter and implanted receiver, as a function of tensile strain. Extracted efficiency at 50 MHz appear in the inset, indicating the strain-insensitive performance for up to 50% strain. Here, the phantom radius is 5.5 cm, and the implantation depth is 1 cm. **D**, Photographs of a stretchable wireless powering system. A stretchable transmitter coil made of PSPN was used to power a red LED device implanted in fish, demonstrating robust and reliable operation when stretched at 50% strain. Scale bars, 2 cm. **E**, Quantitative brightness of the LED wirelessly powered by the transmitter made of the PSPN and conventional Ag NWs under strain.

in **Figure 3.20B**, the soft conformal coil exhibits higher coupling coefficients than conventional rigid coil at all radii. In addition, we note that the transfer efficiency (radius, 5.5 cm; implantation depth, 1 cm) remains stable (>33%) at 50 MHz within 100% tensile strain (**Figure 3.20C**). To evaluate the stretchable wireless powering further, we used the porous nanocomposite transmitter coil to power an implanted red light-emitting diode (LED) in fish (**Figure 3.20D**). Quantitative analysis of the LED brightness suggests reliable and stable operation of the PSPN coil at 50% strain. In contrast, the conventional Ag NWs coil degrades rapidly upon stretching, failing electrically at just 20% strain (**Figure 3.20E**).

We also show the porous nanocomposite's potential as an implantable receiver coil for optoelectronics. The inherently soft and stretchable device with low-modulus mechanics allows for their implantation and dynamic deformations (e.g., bending and stretching) within the animal model. We developed a wireless optoelectronic system comprising an implantable energy harvesting device that captures RF signal from an external transmitter, processes the signal through voltage multiplier, and subsequently routes the generated direct current (DC) voltage to illuminate a red LED. **Figure 3.21A-C** demonstrated the schematic illustration, optical image and working mechanism of the implantable optoelectronic device. The RF power is wirelessly transferred to the receiver coil through inductive coupling, rectified and multiplied by the voltage multiplier, and delivered to the load and LED. We encapsulated the device with silicone elastomer (Smooth-on, Inc.) and deployed between the skin and muscle (subcutaneously) on the ventral side of a mouse while under isoflurane anesthesia (**Figure 3.21D**). There were negligible degradations when stored in phosphate-buffered saline (PBS, pH 7.4) and artificial perspiration (pH 4.3, Pickering Laboratories) for nine days at room temperature (**Figure 3.21E**). The wireless

powering system thus enables real-time, precise control of illumination for freely moving mice (**Figure 3.21F**).

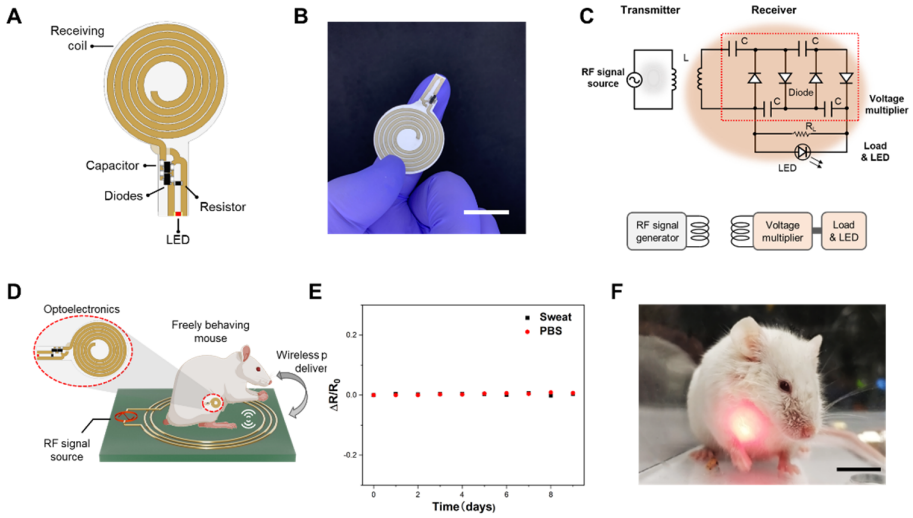


Figure 3.21. Schematic (**A**), photograph (**B**), and working mechanism (**C**) of the implantable optoelectronic device. **D**, Schematic illustration of the *in vivo* demonstration for the implantable wireless power transfer system. An implantable optoelectronic device is subcutaneously implanted between the skin and muscle on the ventral side of the animal. The transmitter wirelessly delivers RF power to the implanted optoelectronic device with precise control over its operation, while allowing for unrestricted movement of the animal. **E**, Stability tests of the optoelectronic device encapsulated with silicone in PBS and artificial sweat. **F**, Photograph of an implanted mouse freely behaving in an NFC-powered setup. Scale bar, 2 cm.

3.6 Wireless stretchable bioelectronics for multiplexed biochemical sensing

To further probe our PSPN's capability for NFC applications, we fabricated a fully stretchable wireless bioelectronic system for multiplexed biochemical sensing. Our battery-free bioelectronic platform comprises a stretchable biochemical sensing interface (i.e., various biochemical sensors) and a spiral coil as the coupling unit for wireless data transmission (**Figure 3.22A**). The design principle relies on a modularized inductor-capacitor (*LC*) resonance circuit model where varactors convert

electrical potential variations into capacitance modulations (**Figure 3.22B**). These modulations directly correspond with the resonance frequency f_s of the *LC* circuit, as described by:

$$f_s = \frac{1}{2\pi\sqrt{LC}}$$

where L and C are the equivalent inductance and capacitance of the resonance circuit, respectively. When targeted analytes are present, the potential difference between the working and reference electrodes of the biochemical sensors corresponds to a frequency shift. Since f_s is an intrinsic property of the resonance circuit, it allows for robust and reliable wireless data transmission. This was exemplified by high-fidelity measurement of a wealth of ions, including Na^+, K^+, NH_4^+, and H^+ (**Figure 3.22C-F**). The obtained readouts exhibit linear relationship with high sensitivities of 0.66 MHz per decade, 0.61 MHz per decade, 0.67 MHz per decade, and 1.04 MHz per decade, respectively.

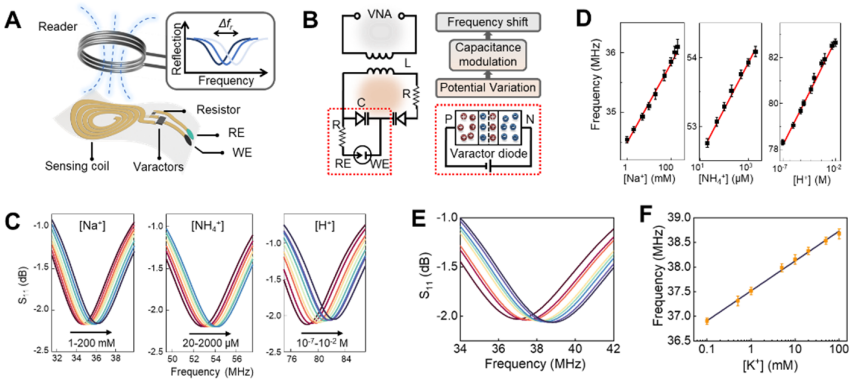


Figure 3.22. A, Schematic illustration of the stretchable, battery-free, and wireless *LC* circuit-based bioelectronics for biochemical sensing. RE, reference electrode; WE, working electrode. B, Equivalent circuit, and operation principle of the wireless sensing system. **C,** Reflection coefficients and frequency shifts (**D**) for wireless Na^+ (1-200 mM), NH_4^+ (20-2000 μM), and H^+ (10^{-7}-10^{-2} M) sensors. **E**, measured reflection spectrum and frequency shifts of wireless K^+ sensor in response to various analyte concentrations in the wireless systems and corresponding fitting line (**F**). Error bars represent standard deviations of three samples.

To achieve multiplexed sensing of biomarkers to capture biometric signature profiles with a minimum level of crosstalk, we carefully chose capacitors in the resonance circuit, producing distinct resonance dips at approximately 38, 55, and 80 MHz. Varying a single analyte in the solution primarily affects its corresponding f_s, with minimal shifts in other sensors, highlighting remarkable selectivity against interfering ions (**Figure 3.23**).

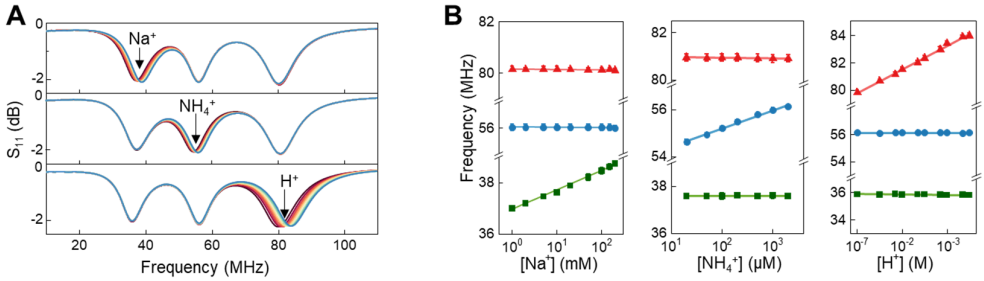


Figure 3.23. A, Reflection spectrum for multiplexed sensing. **B**, Cross-sensitivity extracted from (**A**), indicating negligible crosstalk among these sensors. Red, H^+; blue, NH_4^+; green, Na^+.

Our PSPN, exhibiting strain-insensitive characteristics, significantly enhances the stability of the wireless sensing system under strain. When the PSPN sensing device was subjected to uniaxial tensile stretch, a strain insensitivity of less than 10% performance variation is observed when stretched up to 50% strain, i.e., from 0.68 to 0.62 MHz/decade (**Figure 3.24A, B**). Such changes largely stem from alterations in device geometry, which weaken the coupling strength. Conversely, the device made of conventional nonporous Ag NWs exhibited stark instability under strain, causing a sensitivity reduction from 0.64 to 0.45 MHz/decade at 15% and becoming non-operational at 20% as shown in **Figure 3.24B** and **C**. Furthermore, the devices maintained their initial performance across repetitive strain cycles, with only ~3% and ~5% sensitivity changes after 1,000 cycles at 25% and 50% strains, respectively (**Figure 3.24D**).

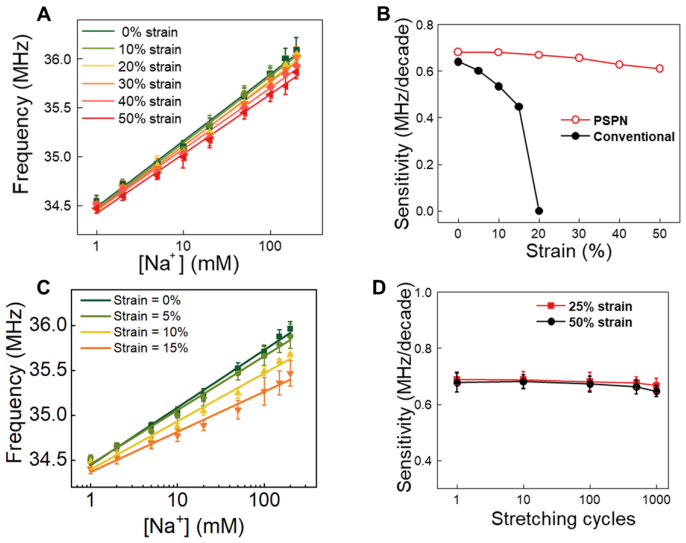


Figure 3.24. A, **B** Frequency shifts (**A**) and sensitivity (**B**) of the wireless Na^+ sensing system made of PSPN (red circle) and conventional Ag NWs (black solid) under strain. **C**, Frequency shifts of the Na^+ sensor integrated with wireless data transmission antenna made of conventional Ag NWs coil under strain. Extracted sensitivity under strain present in **B**. **D**, Alterations in sensitivity observed in the Na^+ sensing system after subjecting the PSPN device to 1,000 repetitive stretching cycles at strain levels of 25% and 50%.

We constructed a multiplexed wireless sensing system integrating glucose and alcohol sensors with high sensitivities of 1.79 MHz/mM and 0.014 MHz per mM respectively (**Figure 3.25A-C**). These developed sensors showcased minimal signal fluctuations even when introduced to a range of interfering biomarkers, underlining their robust selectivity in a physiological environment (**Figure 3.25D-F**). Notably, our wireless sensing system remains stable in physiologically relevant temperature range (**Figure 3.25G** and **H**). Our wireless sensor prototype forms intimate interface with human skin due to the absence of on-chip integrated circuits and intrinsically soft and stretchable form factor (**Figure 3.26A**). This battery-free device facilitates continuous, real-time perspiration monitoring during everyday activities (**Figure 3.26B**). As an example, we monitored the evolutions of glucose and ethanol concentrations in

perspiration over a course of eight hours. Sweat secretion was triggered by a 10-min session of constant-load stationary cycling. As illustrated in **Figure 3.26C** and **D**, we

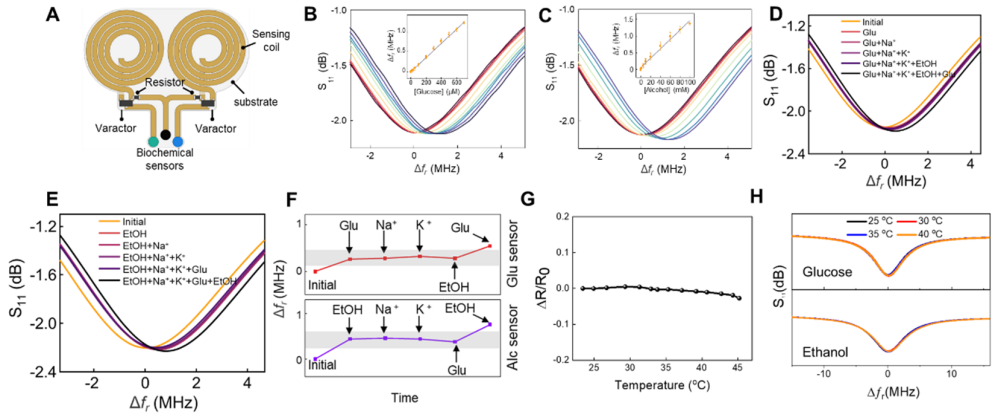


Figure 3.25. A, Schematic of wireless on-body stretchable bioelectronics for multiplexed biochemical sensing. **B**, **C**, Reflection coefficients for wireless on-body glucose (**B**) and alcohol (**C**) monitoring. Calibration plots appear in the inset. D, Glucose sensor responses to the addition of target molecules and interfering biomarkers, including glucose (150 μM), Na^+ (20 mM), K^+ (5 mM), ethanol (20 mM). **E**, Alcohol sensor responses to the addition of target molecules and interfering biomarkers, including ethanol (20 mM), Na^+ (20 mM), K^+ (5 mM), glucose (150 μM). **F**, Selectivity of the glucose and ethanol sensors. Real-time changes of the frequency are extracted from **D** and **E**. **G**, Resistance variations of the PSPN coil under various temperatures (23°C-45°C). **H**, Responses of wireless alcohol and glucose sensors based on PSPN to coil temperature variations at 25°C, 30°C, 35°C, and 40 °C, respectively.

observed a notable rise and subsequent rapid decline in glucose levels-with alcohol levels remaining largely unchanged-post the first meal between 0-3 h. Furthermore, the two biomarkers exhibited nearly synchronized variations following a combined intake of a meal and a drink (1.2 g of white wine (50% alcohol by volume) per 1 kg of the volunteer's body weight).

3.7 Conclusion

We achieved microscale self-assembly of Ag NWs, guided by multiscale porous

elastomer matrices, by leveraging a facile phase separation process under ambient conditions. The selective distribution of Ag NWs on pore surfaces remarkably reduces the percolation threshold (V_c=0.00062) and improves electrical conductivity. The phase-separated soft and porous PU microstructure deforms and enables efficient energy dissipation under large global strains, whereas the rigid Ag NWs conductive pathways adapt to the structural change and preserve its original percolation networks, yielding strain-insensitive conductivity. Harnessing this advanced electromechanical stability and conductivity, we have developed intrinsically soft, stretchable wireless sensing systems suitable for wearable and implantable applications. The systems enable battery-free wireless powering and sensing of a breadth of sweat biomarkers—with less than 10% performance variation even at 50% strain. Furthermore, we note that the phase separation technique can be potentially extended to other conductive nanofillers, such as carbon nanotubes (Supplementary Fig. 30). Collectively, our findings hint at the phase separation approach heralding fresh opportunities for constituent materials across diverse domains.

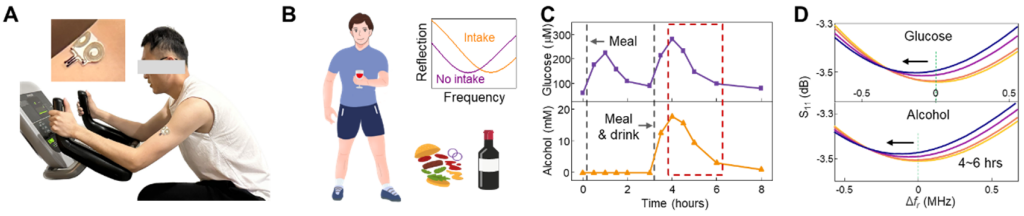


Figure 3.26. A, Photograph of a volunteer wearing a multiplexed wireless biochemical sensing system during cycling exercise. **B-D**, Illustration (**B**) and dynamic wireless analysis of sweat glucose and ethanol levels (**C**, **D**) with and without intake of food and drink over a course of 8 hours. Raw data from 4 to 6 hours in **C** is depicted in **D**.

3.8 Materials and methods

Materials. Bis(2-ethylehexyl) sebacate (DOS), 1-butanol, sodium tetrakis[3,5-

bis(trifluoromethyl)phenyl] borate (Na-TFPB), polyvinyl chloride (PVC), sodium tetraphenylborate (NaTPB), cyclohexanone, polyvinyl butyral（BUTVAR B-98, PVB), NH_4^+ ionophore (nonactin), alcohol oxidase, bovine serum albumin, NaCl, KCl, NH_4Cl were purchased from Sigma Aldrich. Polyaniline base, acetic acid, dimethyl sulfoxide (DMSO), THF, cyclohexanone, PBS solution, and dextrose (D-glucose) were obtained from Fisher Scientific. Glucose Oxidase was acquired from Toyobo Corp. Ag/AgCl ink was purchased from CH Instruments, Inc.

***Synthesis of PSPN and device fabrications*.** The phase-separated porous Ag NWs nanocomposites were prepared by mixing PU (Texin®RxT85A, Covestro) solution (in THF) with Ag NWs solution (20 mg ml^{-1} in ethanol; Ag NW-40, ACS Material) at various concentrations and volume ratios. Drop-casting the nanocomposite precursor solution on aluminum foils and drying under ambient conditions (~3 hours) completed the fabrication of highly conductive PSPN film. Note that the electrical conductivity, stretchability, and electrical-mechanical decoupling are tunable based on the concentrations and volume ratios of constituent materials. PSPN denotes PSPN made from ethanol-based Ag NWs solution, whereas PSPN with 1-butanol represents that made with the co-addition of 1-butanol to control pore sizes (Supplementary Fig. 3). The optimum porous nanocomposite was prepared by mixing 5 g of PU solution (90 mg ml^{-1}) with 4.5 ml of Ag NWs solution (20 mg ml^{-1}) and was used throughout the study unless otherwise stated. Similarly, porous PU substrates were also fabricated by mixing 50 ml of PU solution (70 mg ml^{-1} in THF) with 40 ml of 1-butanol and dried under ambient conditions. The nonporous Ag NWs nanocomposite was fabricated by mixing PU (HydroMed D3, AdvanSource Biomaterial) solution (ethanol:water=9:1) with Ag NWs solution (20 mg ml^{-1} in ethanol). Conventional Ag NWs was fabricated by spray-coating Ag NWs onto oxygen plasma-treated elastomeric PU substrate. Laser

cutting using a VLS2.30 universal laser system defines desired patterns. Stretchable wireless NFC antenna was obtained by transferring pre-designed spiral PSPN coils, assisted by Aquasol water-soluble tape, to the porous PU substrates. Waterborne PU adhesive (HydroMed D3, AdvanSource Biomaterial) allows for strong and robust interface under strain between PSPN and the substrate.

Fabrication of biochemical sensors. We first fabricated soft and stretchable sensors (3 mm diameter) by transfer-printing of laser-induced graphene (LIG) electrodes onto PU elastomer substrates. Specifically, the LIG electrodes were engraved on a polyimide (PI) film using a 30 W CO_2 laser cutter (power, 12%; speed, 15%; VLS2.30 universal laser systems). Next, PU solution (Texin®RxT85A, 40 mg ml^{-1} in THF) was applied and dried at room temperature. Careful transfer-printing from PI film to PU elastomer completed the process. Sodium ion sensor was prepared by drop-casting 10 µl of Na^+ selective membrane solution (1 mg of Na ionophore, 0.55 mg of Na-TFPB, 33 mg of PVC, and 65.45 mg of DOS in 660 µl of THF) on the graphene electrode. Potassium sensor was prepared by drop-casting 6 µl of K^+ selective membrane solution (2 mg of valinomycin, 0.5 mg of NATPB, 32.7 mg of PVC, and 64.7 mg of DOS in 350 µl of cyclohexanone) on each LIG electrode. The NH_4^+ sensor was fabricated by drop-casting 6 µl of NH_4^+ selective membrane solution [1 mg of NH_4^+ ionophore (nonactin), 33 mg of PVC and 66 mg of DOS in THF] on the LIG electrode. Next, pH sensor was prepared by drop-casting 10 µl of the polyaniline base solution (20 mg ml^{-1} in DMSO) on the LIG electrode and dried at 80 °C, followed by 15 min of incubation in 1.0 M HCl. To prepare enzyme-based sensors, gold nanoparticles (25 nm) was first sputter-coated on the LIG electrodes, 5 µl of cocktail (10 mg of Prussian blue and 5 mg of chitosan dissolved in 1 ml of 0.1 M acetic acid) was then drop-casted. Next, 5 µl of enzyme solution was added and dried

at 4 °C overnight, followed by addition of 3 μl of 0.5% Nafion solution. Here, the glucose oxidase solution was prepared by mixing glucose oxidase (10 mg ml^{-1} in PBS) with chitosan/CNT solution (1% chitosan and 5 mg ml^{-1} of MWCNT in 0.1 M acetic acid) at a volume ratio of 1:1. The alcohol oxidase solution was composed of alcohol oxidase, bovine serum albumin (10 mg ml^{-1} in PBS) and chitosan (1% in 0.1 M acetic acid) with a volume ratio of 8:1:1. Reference electrode was prepared by first applying a layer of Ag/AgCl paste onto the LIG electrode, followed by the addition of 3 μl of PVB solution (79.1 mg of PVB and 50 mg of NaCl in 1 ml of methanol).

Characterizations and measurements. SEM images were taken with a FEI Quanta 600 FEG Environmental SEM. Water vapor transmission rates were determined based on ASTM96 at 35 °C. Mechanical properties were characterized using a Mark-10 ESM303 tensile tester. Electrical conductance was measured by a digital source meter (2604B, Keithley Instruments). Fourier transform infrared spectra were obtained using a spectrometer (Nicolet 6700; Thermo Electron Corporation). Electrocardiogram signals were recorded with PowerLab T26 (AD Instruments).

Coil design and numerical simulations. The spiral coils for wearable WPT applications were custom-designed with 8-mm inner radius, 2 turns, 5-mm trace, and 1-mm spacing. The implantable receiver coils feature 5.5-mm inner radius, 5 turns, 1.5-mm trace, and 0.3-mm spacing. The sensing coils for monitoring ions and metabolites are characterized by a 4-mm inner radius, 4 turns, a 1.5-mm trace width, and a 0.3-mm spacing. The magnetic field distributions for the WPT system, the coil under strain, and the coil placed on human body were simulated by using Ansys Maxwell. Particularly, the human body was modeled by a stratified composition of a 1-mm skin layer with relative permittivity of 43 and relative permeability of 1, a 2-mm adipose layer with relative permittivity of 5.28 and relative permeability of 1, and a 7-

mm bone layer with relative permittivity of 11.4 and relative permeability of 1. Notably, due to the unit permeability of those materials, the presence of human tissue barely affects the performance of the WPT system. The RF system simulations were performed by Advanced Design System (ADS).

RF properties characterization and measurements. The equivalent inductance (L), resistance (R), and Q-factor of the coil were obtained by directly connecting the coil to a vector network analyzer (VNA; N5242B PNA-X Network Analyzer, Keysight) and measuring the input impedance Z_{in}. The L, R, and Q values could be extracted from Z_{in} according to the following equation:

$$L = \frac{Im(Z_{in})}{2\pi f}$$

$$R = Re(Z_{in})$$

$$Q = \frac{Im(Z_{in})}{Re(Z_{in})} = \frac{2\pi f L}{R}$$

where $Im(Z_{in})$ and $Re(Z_{in})$ are the imaginary and real parts of the input impedance Z_{in}, respectively, and f is the frequency. For WPT applications, the scattering parameters (S_{11} and S_{21}) and impedance parameters (Z_{11}, Z_{12}, and Z_{22}) of the two-port network were also measured by the Keysight PNA-X VNA. The power transfer efficiency η could be derived from the scattering parameters and the coupling coefficient κ could be obtained from the impedance parameters. The brightness of LED for demonstrating power transfer efficiency was measured by a light meter (ET130, Klein Tools). A portable VNA (LibreVNA) was used for continuous, real-time perspiration monitoring. Common-cathode varactors MAVR-000409-0287FT, MAVR-000405-0287FT, and MAVR-045441-0287AT from Macom were used for achieving resonances at around 38, 55, and 80 MHz, respectively.

Implantation of stretchable wireless optoelectronic device. Adult female Swiss Webster mice (Charles River) were used for surgical implantation of the device. All

animal procedures were performed in accordance with the National Institutes of Health Guide for the Care and Use of Laboratory Animals and approved by the University of Missouri Animal Care and Use Committee. Mice were group housed in cages on a 12:12-h light-dark cycle and fed a standard chow diet ad libitum. The whole device was first sterilized using ethanol, then the device was implanted between the skin and muscle (subcutaneously) on the ventral side of the animal while under isoflurane anesthesia. Prior to implantation, a small incision was made on the lateral side of the animal and the skin was separated from the abdominal muscle with blunt forceps. After implantation, the skin was closed with sutures and the animal was allowed to recover from anesthesia.

Experiments on human subjects. The on-body evaluations of skin-interfaced devices on human participants were conducted under approval from Institutional Review Board at the University of Missouri-Columbia (number 2010272). All human subjects gave written and informed consent before participation in the studies.

3.9 References

1. Y. Xu; Z. Ye,G. Zhao, Q. Fei, Z. Chen, J. Li; M. Yang, Y, Ren; B. Berigan, Y. Ling, X. Qian, L. Shi, I. Ozden, J. Xie, W. Gao, P. Chen, Z. Yan, Phase-Separated Porous Nanocomposite with Ultralow Percolation Threshold Enables Strain-Resilient Wireless Stretchable Bioelectronics. *Nat. Nanotechnol.* *Doi.org/10.1038/s41565-024-01658-6* (2024).

2. D. Jung, C. Lim, H. Shim, Y. Kim, C. Park, J. Jung, S. Han, S. Sunwoo, K. Cho, G.D. Cha, D.C. Kim, J. Koo, J. Kim, T. Hyeon, D.-H. Kim, Highly conductive and elastic nanomembrane for skin electronics. *Science* **373**, 1022-1026 (2021).

3. S. Choi, S.I. Han, D. Jung, H.J. Hwang, C. Lim, S. Bae, O.K. Park, C.M. Tschabrunn, M. Lee, S. Bae, J. Yu, J. Ryu, S. Lee, K. Park, P. Kang, W. Lee, R. Nezafat, T. Hyeon, D. Kim, Highly conductive, stretchable and biocompatible Ag-Au core-sheath nanowire composite for wearable and implantable bioelectronics. *Nat. Nanotechnol.* **13**, 1048-1056 (2018).

4. W. Lee, H. Kim, I. Kang, H. Park, J. Jung, H. Lee, H. Park, J. Park, J. Yuk, S. Ryu, J. Jeong, J. Kang, Universal assembly of liquid metal particles in polymers enables elastic printed circuit board. *Science* **378**, 637-641 (2022).

5. N. Matsuhisa, D. Inoue, P. Zalar, H. Jin, Y. Matsuba, A. Itoh, T. Yokota, D. Hashizume, T. Someya, Printable elastic conductors by in situ formation of silver nanoparticles from silver flakes. *Nat. Mater.* **16**, 834-840 (2017).

6. S. Veerapandian, W. Jang, J.B. Seol, H. Wang, M. Kong, K. Thiyagarajan, J. Kwak, G. Park, G. Lee, W. Suh, I. You, M.E. Kılıç, A. Giri, L. Beccai, A. Soon, Hydrogen-doped viscoplastic liquid metal microparticles for stretchable printed metal lines. *Nat. Mater.* **20**, 533-540 (2021).

7. Y. Hui, Y. Yao, Q. Qian, J. Luo, H. Chen, Z. Qiao, Y. Yu, L. Tao, N. Zhou, Three-dimensional printing of soft hydrogel electronics. *Nat. Electron.* **5**, 893–903 (2022).

8. Z. Jiang, N. Chen, Z. Yi, J. Zhong, F. Zhang, S. Ji, R. Liao, Y. Wang, H. Li, Z. Liu, Y. Wang, T. Yokota, X. Liu, K. Fukuda, X. Chen, T. Someya, A 1.3-micrometre-thick elastic conductor for seamless on-skin and implantable sensors. *Nat. Electron.* **5**, 784-793 (2022).

9. Y. Zhao, Y. Ohm, J. Liao, Y. Luo, H.-Y. Cheng, P. Won, P. Roberts, M.R. Carneiro, M.F. Islam, J.H. Ahn, A self-healing electrically conductive organogel composite. *Nat. Electron.* **6**, 206–215 (2023).

10. Z. Jiang, M.O.G. Nayeem, K. Fukuda, S. Ding, H. Jin, T. Yokota, D. Inoue, D. Hashizume, T. Someya, Highly stretchable metallic nanowire networks reinforced by the underlying randomly distributed elastic polymer nanofibers via interfacial adhesion improvement. *Adv. Mater.* **31**, 1903446 (2019).

11. Y. Luo, M.R. Abidian, J.-H. Ahn, D. Akinwande, A.M. Andrews, M. Antonietti, Z. Bao, M. Berggren, C.A. Berkey, C.J. Bettinger, Technology roadmap for flexible sensors. *ACS Nano* **17**, 5211-5295 (2023).

12. C. Wang, T. He, H. Zhou, Z. Zhang, C. Lee, Artificial intelligence enhanced sensors-enabling technologies to next-generation healthcare and biomedical platform. *Bioelectron. Med.* **9**, 17 (2023).

13. S. Choi, S. Han, D. Kim, T. Hyeon, D.-H. Kim, High-performance stretchable conductive nanocomposites: materials, processes, and device applications. *Chem. Soc. Rev.* **48**, 1566-1595 (2019).

14. K. Sim, Z. Rao, F. Ershad, C. Yu, C. Rubbery electronics fully made of stretchable elastomeric electronic materials. *Adv. Mater.* **32**, 1902417 (2020).

15. W. Gao, S. Emaminejad, H.Y.Y. Nyein, S. Challa, K. Chen, A. Peck, H.M. Fahad, H. Ota, H. Shiraki, D. Kiriya, Fully integrated wearable sensor arrays for multiplexed in situ perspiration analysis. *Nature* **529**, 509-514 (2016).

16. Y. Yang, W. Gao, W. Wearable and flexible electronics for continuous molecular monitoring. *Chem. Soc. Rev.* **48**, 1465-1491 (2019).

17. J. Kim, Y. Wang, H. Wang, S. Lee, T. Yokota, T. Someya, Skin electronics: next-generation device platform for virtual and augmented reality. *Adv. Funct. Mater.* **31**, 2009602 (2021).

18. K. Yamagishi, W. Zhou, T. Ching, S.Y. Huang, M. Hashimoto, Ultra-deformable and tissue-adhesive liquid metal antennas with high wireless powering efficiency. *Adv. Mater.* **33**, 2008062 (2021).

19. Q. Zhuang, K. Yao, M. Wu, Z. Lei, F. Chen, J. Li, Q. Mei, Y. Zhou, Q. Huang, X. Zhao, Wafer-patterned, permeable, and stretchable liquid metal microelectrodes for implantable bioelectronics with chronic biocompatibility. *Sci. Adv.* **9**, eadg8602 (2023).

20. D. Jung, C. Lim, C. Park, Y. Kim, M. Kim, S. Lee, H. Lee, J.H. Kim, T. Hyeon, D.H. Kim, Adaptive self-organization of nanomaterials enables strain-insensitive resistance of stretchable metallic nanocomposites. *Adv. Mater.* **34**, 2200980 (2022).

21. T. Wang, Q. Liu, H. Liu, B. Xu, H. Xu, Printable and highly stretchable viscoelastic conductors with kinematically reconstructed conductive pathways. *Adv. Mater.* **34**, 2202418 (2022).

22. S. Kim, H. Seo, J. Kang, J. Hong, D. Seong, H.-J. Kim, J. Kim, J. Mun, I. Youn, J. Kim, *ACS Nano* **13**, 6531-6539 (2019).

23. B. Sun, R.N. McCay, S. Goswami, Y. Xu, C. Zhang, Y. Ling, J. Lin, Z. Yan, Gas-permeable, multifunctional on-skin electronics based on laser-induced porous graphene and sugar-templated elastomer sponges. *Adv. Mater.* **30**, 1804327 (2018).

24. H. Yi, D. Li, Z. Lv, R. Li, M. Ling, H. Zhang, Q. Zheng, X. Li, Constructing high-performance 3D porous self-standing electrodes with various morphologies and shapes by a flexible phase separation-derived method. *J. Mater. Chem. A* **7**, 22550-22558 (2019).

25. Y. Wang, T. Yokota, T. Someya, Electrospun nanofiber-based soft electronics, Electrospun nanofiber-based soft electronics. *NPG Asia Mater.* **13**, 22 (2021).

26. D. Zhu, S. Handschuh-Wang, X. Zhou, Recent progress in fabrication and application of polydimethylsiloxane sponges. *J. Mater. Chem. A* **5**, 16467-16497

(2017).
27. S. Yao, W. Zhou, R. Hinson, P. Dong, S. Wu, J. Ives, X. Hu, H. Huang, Y. Zhu, Ultrasoft porous 3D conductive dry electrodes for electrophysiological sensing and myoelectric control. *Adv. Mater. Technol.* **7**, 2101637 (2022).
28. W. Zhou, S. Yao, H. Wang, Q. Du, Y. Ma, Y. Zhu, Gas-permeable, ultrathin, stretchable epidermal electronics with porous electrodes. *ACS Nano* **14**, 5798–5805 (2020).
29. F. Wang, P. Altschuh, L. Ratke, H. Zhang, M. Selzer, B. Nestler, Progress report on phase separation in polymer solutions. *Adv. Mater.* **31**, 1806733 (2019).
30. A. Hołda, I.F. Vankelecom, Understanding and guiding the phase inversion process for synthesis of solvent resistant nanofiltration membranes. *J. Appl. Polym. Sci.* **132**, 42130 (2015).
31. H. Zhu, H. Gao, H. Zhao, J. Ge, B. Hu, J. Huang, S. Yu, Hierarchically porous polymer coatings for highly efficient passive daytime radiative cooling. *Science* **362**, 315-319 (2018).
32. H. Zhu, H. Gao, H. Zhao, J. Ge, B. Hu, J. Huang, S. Yu, Printable elastic silver nanowire-based conductor for washable electronic textiles. *Nano Res.* **13**, 2879-2884 (2020).
33. H. Lee, B. Jung, Y. Kang, H. Lee, Phase separation of polymer casting solution by nonsolvent vapor. *J. Membr. Sci.* **245**, 103-112 (2004).
34. X. Sun, G. Sun, X. Wang, Morphology modeling for polymer monolith obtained by non-solvent-induced phase separation. *Polymer* **108**, 432-441 (2017).
35. B. Binks, S. Lumsdon, Pickering emulsions stabilized by monodisperse latex particles: effects of particle size. *Langmuir* **17**, 4540-4547 (2001).
36. M. Taya, W. Kim, K. Ono, Piezoresistivity of a short fiber/elastomer matrix composite. *Mech. Mater.* **28**, 53-59 (1998).
37. J. Li, P. Ma, W. Chow, C. To, B. Tang, J. Kim, Correlations between percolation threshold, dispersion state, and aspect ratio of carbon nanotubes. *Adv. Funct. Mater.* **17**, 3207-3215 (2007).
38. R. Ma, B. Kang, S. Cho, M. Choi, S. Baik, Extraordinarily high conductivity of stretchable fibers of polyurethane and silver nanoflowers. *ACS Nano* **9**, 10876-10886 (2015).
39. L. Tang, J. Shang, X. Jiang, Multilayered electronic transfer tattoo that can enable the crease amplification effect. *Sci. Adv.* **7**, eabe3778 (2021).

40. Y. Ohm, C. Pan, M. Ford, X. Huang, J. Liao, C. Majidi, An electrically conductive silver–polyacrylamide–alginate hydrogel composite for soft electronics. *Nat. Electron.* **4**, 185–192 (2021).

41. H. Kang, Y. Kim, S. Cheon, G.-R. Yi, J. Cho, An integrated self-healable electronic skin system fabricated via dynamic reconstruction of a nanostructured conducting network. *Nat. Nanotechnol.* **13**, 1057-1065 (2018).

42. Kang, H., Kim, Y., Cheon, S., Yi, G.-R. & Cho, J. H. Halide welding for silver nanowire network electrode. *ACS Appl. Mater. Interfaces* **9**, 30779-30785 (2017).

43. R. Taherian, R. Development of an equation to model electrical conductivity of polymer-based carbon nanocomposites. *ECS J. Solid State Sci. Technol.* **3**, M26 (2014).

44. Y. Liu, J. Zhang, H. Gao, Y. Wang, Q. Liu, S. Huang, C.F. Guo, Z. Ren, Capillary-force-induced cold welding in silver-nanowire-based flexible transparent electrodes. *Nano Lett.* **17**, 1090-1096 (2017).

45. H. Chung, B. Kim, J. Lee, J. Lee, Z. Xie, E.M. Ibler, K. Lee, A. Banks, J. Jeong, J. Kim, Binodal, Binodal, wireless epidermal electronic systems with in-sensor analytics for neonatal intensive care. *Science* **363**, eaau0780 (2019).

46. W. Ouyang, W. Lu, Y. Zhang, Y. Liu, J.U. Kim, H. Shen, Y. Wu, H. Luan, K. Kilner, S.P. Lee, A wireless and battery-less implant for multimodal closed-loop neuromodulation in small animals. *Nat. Biomed. Eng.* **7**, 1252–1269 (2023).

47. Y. Jiang, A. Trotsyuk, S. Niu, D. Henn, K. Chen, C. Shih, M.R. Larson, A. Mermin-Bunnell, S. Mittal, J. Lai, Wireless, closed-loop, smart bandage with integrated sensors and stimulators for advanced wound care and accelerated healing. *Nat. Biotechnol.* **41**, 652–662 (2023).

48. Y. Zhang, Z. Huo, X. Wang, X. Han, W. Wu, B. Wan, H. Wang, J. Zhai, J. Tao, C. Pan, High precision epidermal radio frequency antenna via nanofiber network for wireless stretchable multifunction electronics. *Nat. Commun.* **11**, 5629 (2020).

49. T. Liu, Y. Dong, S. Chen, J. Zhou, Z. Ma, J. Li, Battery-free, tuning circuit–inspired wireless sensor systems for detection of multiple biomarkers in bodily fluids. *Sci. Adv.* **8**, eabo7049 (2022).

50. S. Park, D. Brenner, G. Shin, C. Morgan, B. Copits, H. Chung, M. Pullen, K. Noh, S. Davidson, S. Oh, Soft, stretchable, Soft, stretchable, fully implantable miniaturized optoelectronic systems for wireless optogenetics. *Nat. Biotechnol.* **33**, 1280-1286 (2015).

51. T. Someya, Z. Bao, G. Malliaras, The rise of plastic bioelectronics. *Nature* **540**, 379–385 (2016).

Chapter 4. Multifunctional Cellulose Nanofibril Interfaces for High-Quality Printing, Strain Resilience, and Microfluidics in Porous Bioelectronics

The materials and contents in this chapter are reorganized to a paper named "Multifunctional Cellulose Nanofibril Interfaces for High-Quality Printing, Strain Resilience, and Microfluidics in Porous Bioelectronics", which is in preparation to submit to a research journal.

Abstract: Porous, soft bioelectronics have recently garnered broad interest due to their high breathability, long-term biocompatibility, and other characteristics inaccessible in nonporous counterparts. However, it remains a challenge to produce high-quality porous biophysical and biochemical sensors using scalable, easily customizable solution-printing approaches, largely owing to their coarse surface textures. Moreover, the demand for strain resilience to maintain operational stability under mechanical deformation, coupled with the need for integrated microfluidics for regulating biochemical sensing, adds to the complexity of developing advanced porous soft bioelectronics. In this work, we present multifunctional cellulose nanofibril (CNF) interfaces patterned on phase-separated multifunctional porous soft elastomers for enabling high-quality printing, strain resilience, and microfluidics in porous bioelectronics. Here, CNF interfaces substantially smoothen the surface roughness of porous elastomers from ~6.8 μm to ~0.2 μm, thereby enhancing solution-printing quality. Concurrently, they impart a robust strain-isolation effect, evidencing less than 0.1% device performance variation under 100% strain, attributable to mechanical heterogeneity and strong interfacial bonding between CNF interfaces and porous elastomers. CNF-based microfluidic channels enable continuous

collection, transportation, and discharge of sweat. In addition, a hybrid composite ink of silver nanowires and poly(3,4-ethylenedioxythiophene): poly (styrene sulfonate) has been formulated as a basis material for printing conductive pathways and sensing electrodes for electrophysiological and biochemical signals. A porous device was developed as an exemplary example, capable of simultaneously monitoring electrocardiograms and sweat glucose and beta-hydroxybutyrate for management of energy metabolism and consumption. This research provides a new blueprint for making high-quality, porous soft bioelectronics with customizable multimodalities to meet diverse and evolving healthcare needs.

4.1 Introduction

Next-generation soft bioelectronics should enable long-term and high-fidelity monitoring of vital biophysical and biochemical signals from human bodies throughout daily activities (*1-3*). In this context, porous soft bioelectronics have recently captured intense interest because of their high breathability, which can effectively minimize sweat accumulation-caused inflammation and device performance degradation, thus benefiting their long-term on-body operation (*4-6*). Also, porous devices can be endowed with additional features, such as self-cooling (*7*) and antimicrobial properties (*8*), through structural design and functional molecule incorporation. Typically, porous devices comprise customized bioelectronic components patterned on porous soft substrates. At present, porous soft substrates mainly include textiles (*9, 10*) and various porous materials made by electrospinning, phase separation (*8, 11, 12*), freeze drying (*13*), and other methods (*14, 15*). Bioelectronic fabrication on porous soft substrates can be achieved using lithograph-based approaches (*9, 16*). Compared to this traditional fabrication technique, mask-free solution printing (e.g., inkjet printing and extrusion printing) provides a promising avenue for the scalable, easily customizable manufacturing of both biophysical and biochemical sensors through appropriate ink formulations (*17-19*). However, it remains a great challenge to produce high-quality porous biophysical and biochemical sensors with solution printing, largely owing to the inherent roughness of porous surfaces (*20, 21*). Furthermore, ensuring that bioelectronics is strain-resistant to preserve stable function under deformation, along with integrating microfluidic channels for regulating biochemical analysis, complicates the fabrication of porous soft bioelectronics with customized multimodalities (*22-24*).

Cellulose, Earth's most abundant renewable biopolymer, is characterized by its

structured fibrous arrays with specific orientations (*25*). Employing a range of top-down methodologies, cellulose can be deconstructed into fibrils and further refined into cellulose nanofibrils (CNF) (*26, 27*). CNF boasts noteworthy mechanical properties for stiff engineering and strain regulation when interfaced with soft materials and, through chemical modification, can form strong bonds with other substances via the hydroxyl groups intrinsic to cellulose (*25, 27*). Furthermore, cellulose nanofibril interfaces (CNFI) usually possess a mesoporous structure that allows for breathability, improves ink absorption, and enhances printing quality, which makes them ideally suited for high-quality bioelectronics printing. Moreover, the intrinsic hydrophilicity renders CNF excellent for the development of microfluidic channels via hydrophilic interface engineering (*28, 29*).

Here, we explore the application of multifunctional cellulose CNFI in enhancing the printing quality, strain resilience, and microfluidic integration of porous soft bioelectronics. In this work, we use phase-separated porous styrene-ethylene-butylene-styrene (SEBS) as a model example of porous materials for CNFI integration and bioelectronic fabrication. As illustrated in **Figure 4.1**, biomass-derived CNF can be patterned onto porous SEBS for surface flatness and strain engineering, which are critical for achieving high-quality printing of bioelectronic components (such as biophysical and biochemical sensors and conductive traces) with outstanding strain resilience. Notably, a robust interfacial bonding is enabled between CNF and porous substrates because of the CNFs' partial infiltration into the porous matrix and the formation of hydrogen bonds with oxygen plasma-treated SEBS. Additionally, strategically engineered CNF patterns on porous SEBS can serve as microfluidic channels, capable of continuous collection, transportation, and discharge of sweat, essential for biochemical sensing. Also, a composite ink of silver nanowires (Ag NWs)

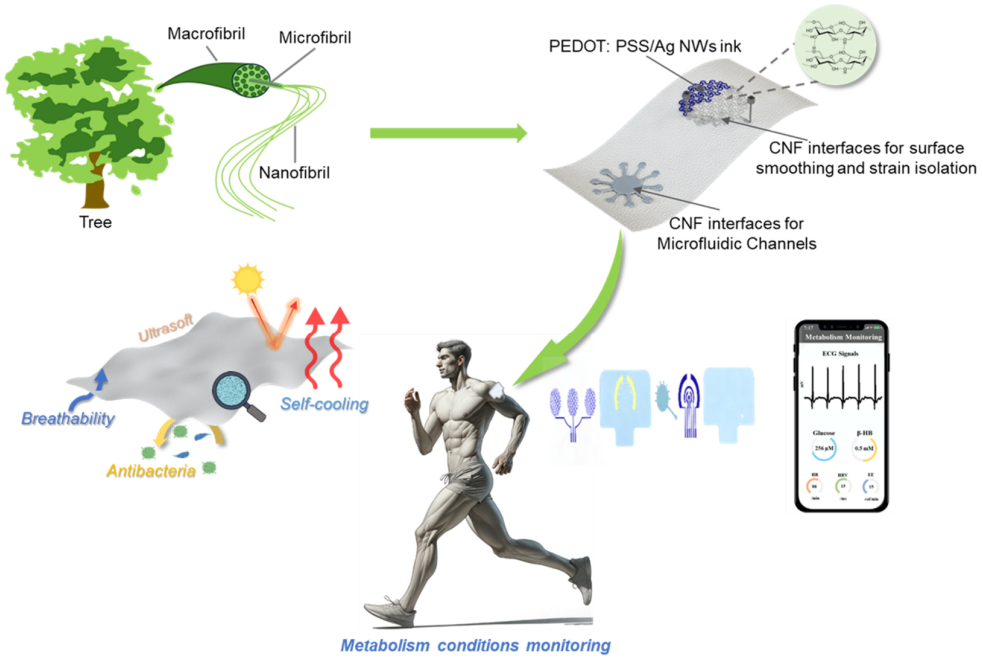


Figure 4.1. Illustration of multifunctional CNFI for high-quality printing, stain resilience, and microfluidics in porous soft bioelectronics. Here, phase-separated porous soft SEBS is used as the porous material example for CNFI integration and bioelectronics fabrication. Porous SEBS indicates desired multifunctionalities for soft bioelectronics, including ultrasoftness, high breathability, antibacterial properties, and self-cooling capabilities. Also, an exemplary example of a porous device has been developed that can simultaneously monitor ECG, glucose, and β-HB for the management of energy metabolism and consumption. HR, HRV, and EE can be determined from recorded ECG. The collected data can be in-situ processed and wirelessly transmitted for graphical display on a smartphone through flexible electronic circuits.

and poly(3,4-ethylenedioxythiophene): poly (styrene sulfonate) (PEDOT: PSS) has been formulated as a basis material for printing both conductive pathways and sensing electrodes for electrophysiological and biochemical signals. Furthermore, we present a prototype porous device capable of concurrently monitoring electrocardiogram (ECG) and sweat glucose and beta-hydroxybutyrate (β-HB), offering insights into energy metabolism and consumption. Parameters such as heart rate (HR), heart rate variability (HRV), and energy expenditure (EE) can be deduced from recorded ECG signals. The

collected data can be in-situ processed and wirelessly transmitted for graphical display on a smartphone through flexible electronic circuits.

4.2 Fabrication of CNF inks and engineering CNF interfaces on porous substrates

To prepare CNF, commercially sourced softwood pulp undergoes treatment with 2,2,6,6-tetramethylpiperidine-1-oxyl (TEMPO) to oxidize cellulose C6 hydroxyl groups to carboxyl groups, thus promoting the disintegration of elementary fibrils and facilitating the isolation of microfibrils, as depicted in **Figure 4.2**. These cellulose microfibrils are aggregates of CNF bundles, further elaborated upon TEM in **Figure 4.2A**. Following the process of ultrasonication, a homogeneous dispersion of CNF with an average diameter of approximately 6 nm and lengths extending into the hundreds of nanometers is obtained (**Figure 4.2B**). Additionally, long CNF (L-CNF) can also be obtained by low-power ultrasonication (**Figure 4.2C**)

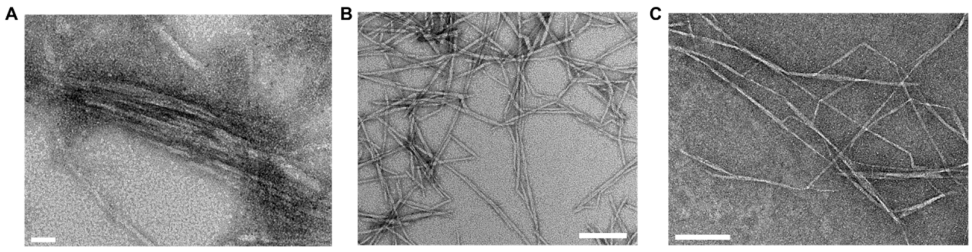


Figure 4.2. TEM image of CNF bundles (**A**) before treatment by tip ultrasonation and CNF (**B**). Scale bar 20 nm (**A**) and 100 nm (**B**).

In the pursuit of developing an ink formulation conducive to extrusion printing, we investigate the rheological behaviors of the derived CNF inks across varying concentrations. It was observed that with an increase in concentration from 1wt.% to 3wt.%, the viscosity of the CNF ink escalated from 0.1 to 10 Pa·s at the shear rate of 1 s^{-1}, which is suboptimal for printing purposes (*30*) (**Figure 4.3A**). Furthermore, the

viscoelastic characteristics of the CNF inks in **Figure 4.3B** revealed a yield stress below 10 Pa, which could potentially induce lateral spreading during the printing process. When we further increase the concentration of the ink, the ink exhibited a lack of homogeneity. To address this limitation, L-CNF was involved. Rheological evaluations in **Figure 4.3C** and **D**, indicate that the L-CNF ink possesses reduced viscosity and yield stress in comparison to the CNF inks at same concentrations. Our investigations further revealed that ink formulations comprising a blend of CNF and L-CNF exhibit superior viscosity and yield stress (**Figure 4.3E** and **F**) when compared to inks composed solely of L-CNF at equivalent concentrations because the mixture ink can form better network of fibrils interactions (*31, 32*).

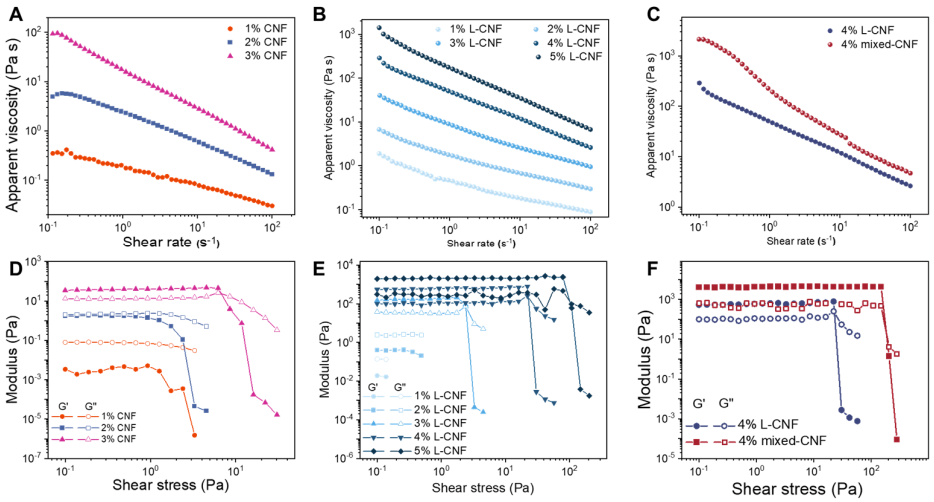


Figure 4.3. Rheological properties of the CNF inks **A**, apparent viscosity as a function of shear rate for CNF inks with various concentrations, long CNF inks with various concentrations (**B**) and 4% mixed CNF ink (**C**). **D**, The storage modulus, G′, and loss modulus, G″, as a function of shear stress for CNF inks with various concentrations, long CNF inks with various concentrations (**E**) and 4% mixed CNF ink (**F**).

Additionally, this hybrid ink demonstrates enhanced bonding forces to substrates as shown in **Figure 4.4A**. Opting for a balanced approach, we selected a mixed ink formulation containing 2% CNF and 2% L-CNF for subsequent CNFI construction,

aiming to harmonize printability with strong interfaces adhesion. As exposed in **Figure 4.4B-E**, the constructed CNFI notably reduces the surface roughness of porous SEBS from 6.79 μm to 0.18 μm. It's worth noting that the application of CNFI on the porous SEBS exerts minimal impact on its breathability (**Figure 4.4F**).

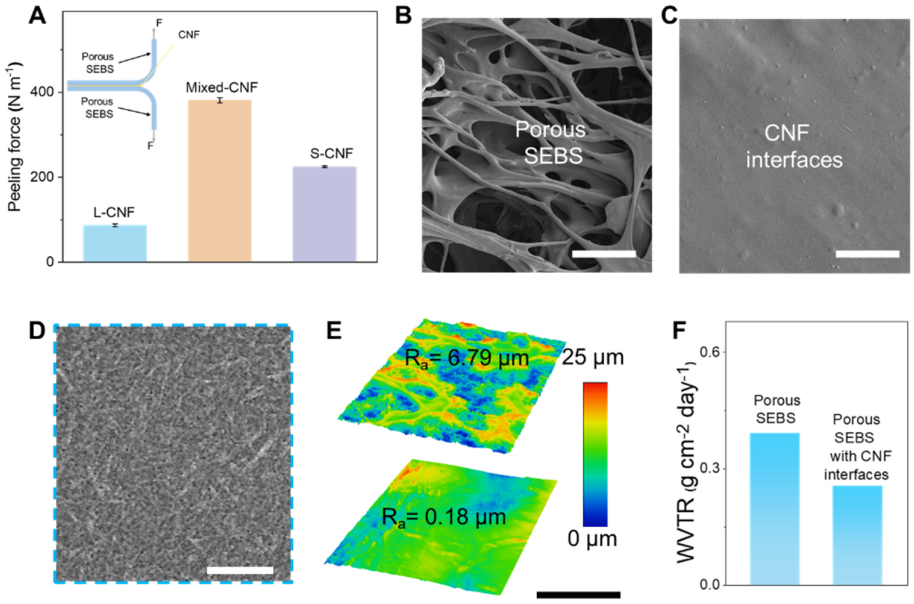


Figure 4.4. CNFI on porous SEBS. **A**, Peeling force test of the bonding force between the CNF and porous SEBS. **B**, SEM image of porous SEBS (**B**) and SEBS with CNFI (**C, D**). Scale bar: 20 μm (**B** and **C**) and 0.5 μm (**D**). **E**, 3D laser scanning microscope image of the porous SEBS without (top) and with CNFI construction. Scale bar: 300 μm. **F**, Water vapor transmission rates (WVTRs) of porous SBBS and porous SEBS with CNFI, showing the CNFI has small influence on the breathability of porous SEBS.

To print biosensors based on the constructed CNFI on porous SEBS, we developed composite inks composed of Ag NWs and PEDOT: PSS. (**Figure 4.5A** and **B)** for both biophysical and biochemical sensors fabrication. The engineered CNFI on porous SEBS notably improves the quality of both extrusion and inkjet printing. As the schematic illustration in **Figure 4.5C**, the uncontrolled capillary force arising from the nonuniform distribution of micrometer-sized pores in the porous SEBS causes the ink

droplets to spread randomly, leading to deformation of the printed patterns (*20, 21*) (**Figure 4.5C**, top**)**. In contrast, the low roughness of the CNFI leads to high-quality printing outcomes (**Figure 4.5C**, bottom).

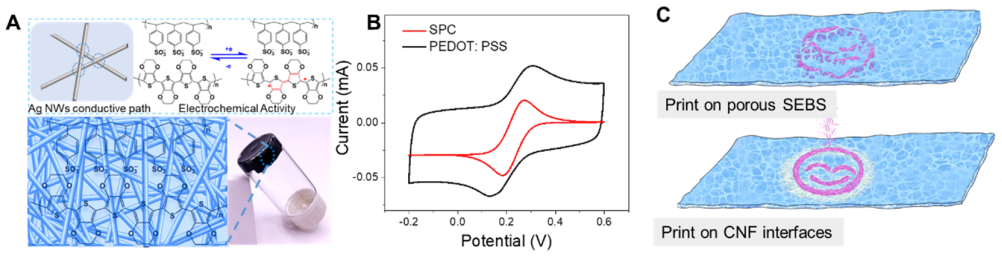


Figure 4.5. Bifunctional PEDOT: PSS/ Ag NWs inks for printing. **A**, Schematic illumination of bifunctional PEDOT: PSS/Ag NWs ink (**A**) and cyclic voltammograms curves comparison (**B**) of the PEDOT: PSS electrode and commercial SPCE tested in 0.1 M KCl solution containing 10 mM $[Fe(CN)_6]^{3-/4-}$. **C**, Schematic illumination depicting that the engineered CNFI on on porous SEBS contributed to the high-quality.

Figure 4.6 shows the high-quality printed patterns on CNF-interfaced porous SEBS. It is observed that both inkjet and extrusion printed lines on the CNF-interfaced porous SEBS exhibit sharp edges. In contrast, lines printed directly on porous SEBS show noticeable printing imperfections (**Figure 4.6**A and **B**). The efficacy of the CNF coating is further corroborated by the I-V curves in **Figure 4.6C**, which reveal a dramatic reduction in resistance by a factor of 10, 000,000 for lines 200 µm printed on CNF interfaced substrates compared to those printed on bare porous SEBS. High-quality patterns, including inkjet-printed hexagonal re-entrant honeycombs (**Figure 4.6D**, top) and serpentine structures (**Figure 4.6D**, bottom) of various sizes, as well as extrusion printed serpentine arrays (**Figure 4.6E**), were successfully fabricated on the CNF interfaced porous SEBS. This advancement underscores the critical role of CNFI in achieving precise and reliable printing on porous substrates, thereby enhancing the functional capabilities of the resulting biosensors and electronic devices.

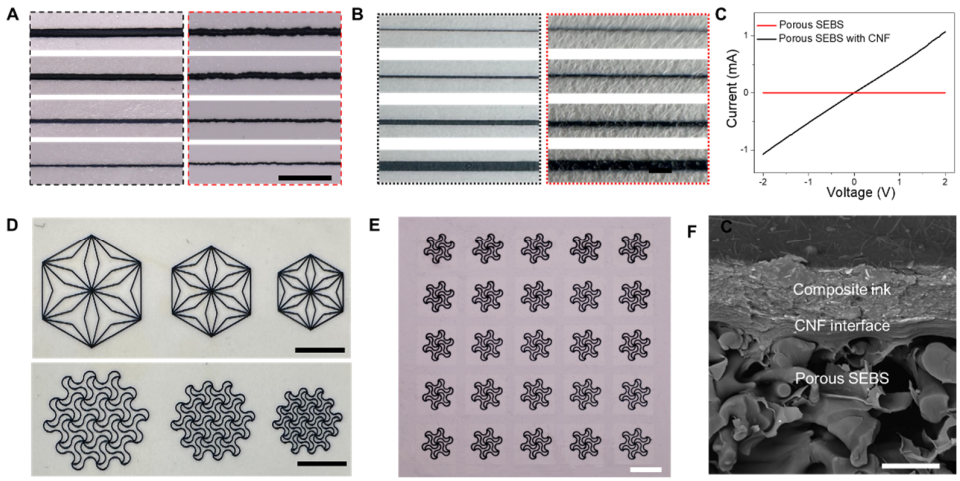


Figure 4.6. High quality printing on CNFI. **A**, Optical images of extrusion printed patterns on porous SEBS with (left) and CNF interfaced porous SEBS (right). Scale bar: 5 mm. **B**, Optical images of the inkjet printed PEDOT: PSS/Ag NWs lines with different width on CNF interfaced porous SEBS (left) and bare porous SEBS (right). Scale bar:1 mm. **C**, IV curves of the inkjet printed PEDOT: PSS/Ag NWs line (200 μm) on CNF interfaced porous SEBS (black) and bare porous SEBS (red). **D-E**, High quality printing of various complex patterns and arrays on CNF interfaced porous SEBS. **F**, SEM image of cross-section of the patterns. Scale bar, 2.5 mm (**D**), 1 cm (**E**) and 10 μm (**F**).

4.3 CNFI enabled strain resilient wearable bioelectronics

Given that CNF exhibits an obviously higher Young's modulus (up to 1 GPa) compared to porous SEBS (approximately 0.2 MPa) (*4, 25*), CNF interfaced on porous SEBS treated by oxygen plasma emerges as a strategy for constructing strain resilient bioelectronics beyond its role in decrease surface roughness. As illustrated in **Figure 4.7A**, the CNF pattern interfaced within the porous SEBS acts as a strain isolation unit, maintaining stability under mechanical stress, while the intrinsic stretchability of porous SEBS is preserved. Finite Element Analysis (FEA) simulations further corroborate the durability of the CNF islands under strain. A specific configuration is demonstrated to remain intact under 100% bi-axial strain, as shown in **Figure 4.7B,** left. This theoretical outcome aligns closely with experimental findings obtained

through digital image correlation (DIC) techniques (**Figure 4.7B**, right).

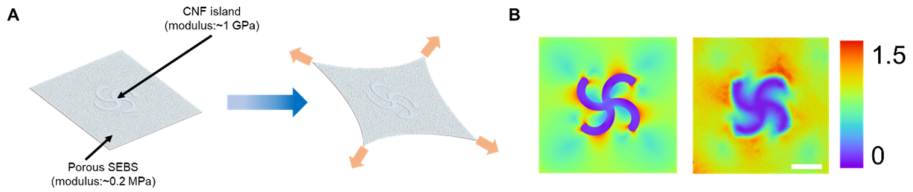


Figure 4.7. High quality printing on CNFI. **A**, Schematic illumination to show that the CNFI on porous SEBS can keep stable under stretch. **B**, FEA simulation of the strain isolation performances of CNFI on porous SEBS (left) under strain and corresponding experimental result (right). The color bar is the strain. Scale bar, 1cm.

The remarkable stability of the CNFI can be attributed to the porous structure of the SEBS, which not only mitigates stress concentration around the edges of CNFI, but also enhances the interfacial bond by increased contact areas between CNF and porous SEBS. Comparative stress analysis, detailed in **Figure 4.8**, reveals that the stress experienced at the edges of CNFI embedded in porous SEBS is significantly lower than that in non-porous SEBS substrates. This difference features the importance of the substrate's porous structure in enhancing the durability of the bonding interfaces.

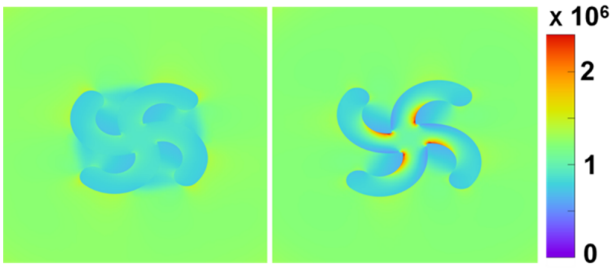


Figure 4.8. FEA simulation of the stress distribution for the CNFI on porous SEBS (left) and no porous SEBS (right) under 100% strain. Obvious stress concertation was observed on the edge of the pattern of no porous SEBS, demonstrating the porous SEBS can efficiently mitigate the stress concentration under strain.

The robustness of the interfacial bond between CNF and porous SEBS is further

demonstrated by molecular dynamics simulations that quantitatively assess the presence of hydrogen bonds. **Figure 4.9A-C** reveal a substantial number of hydrogen bonds at the interface between porous SEBS and CNF. In contrast, virtually no hydrogen bonds were observed at the interface between nonporous SEBS and CNF due to their poor contact distance being greater than the length of a hydrogen bond (2.8 Å) (*33*), as elaborated in **Figure 4.9D**. Further empirical evidence of the formidable bonding strength is provided by the results of the peeling test depicted in **Figure 4.4A**, which records a remarkable force of approximately 380 N m^{-1}.

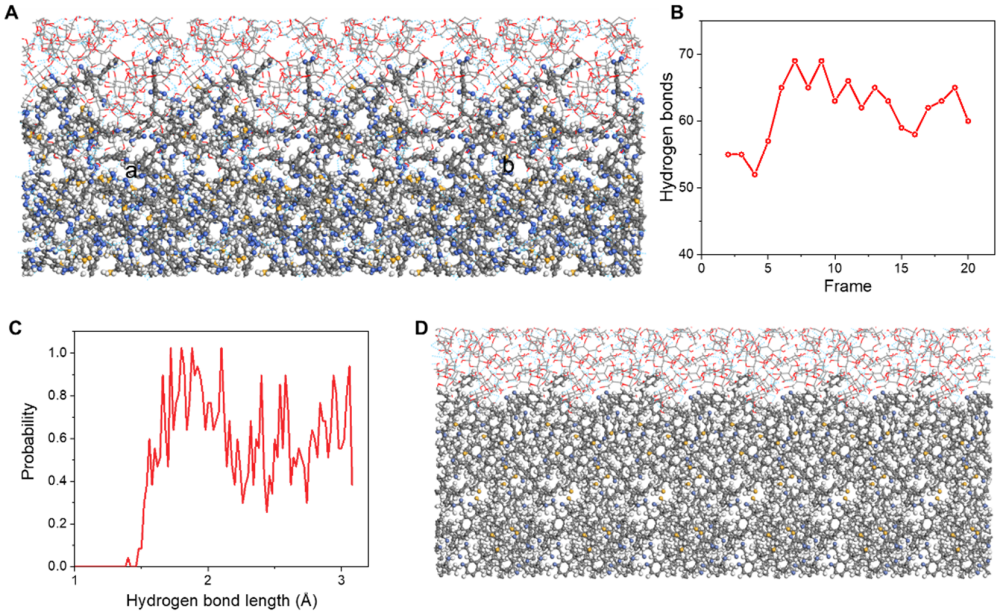


Figure 4.9. Molecular dynamics simulation of the interfaces between CNF and SEBS. **A**, Calculated bonding force of the interface between the CNF and porous SEBS. The amount of hydrogen bonds (**B**) and probability of various bond length (**C**) on the interface of CNF and porous SEBS. D, Calculated bonding force of the interface between the CNF and nonporous SEBS. The red represents the hydrogen bonds in A and D.

This level of adhesive strength is sufficient to support a weight of 500 grams (**Figure 4.10A**). The cross-section SEM image presented in **Figure 4.10B** reveals the diffusion of CNF into the porous SEBS substrate, resulting in the formation of robust

bond that underpins the composite's mechanical integrity. The exceptional capacity of the CNFI to serve as strain isolation units under mechanical stress is further evidenced by DIC and optical imaging **Figure 4.10C**. Those results showcase the CNFI' resilience and stability under applied strain, affirming its efficacy as strain isolation elements within the composite structure.

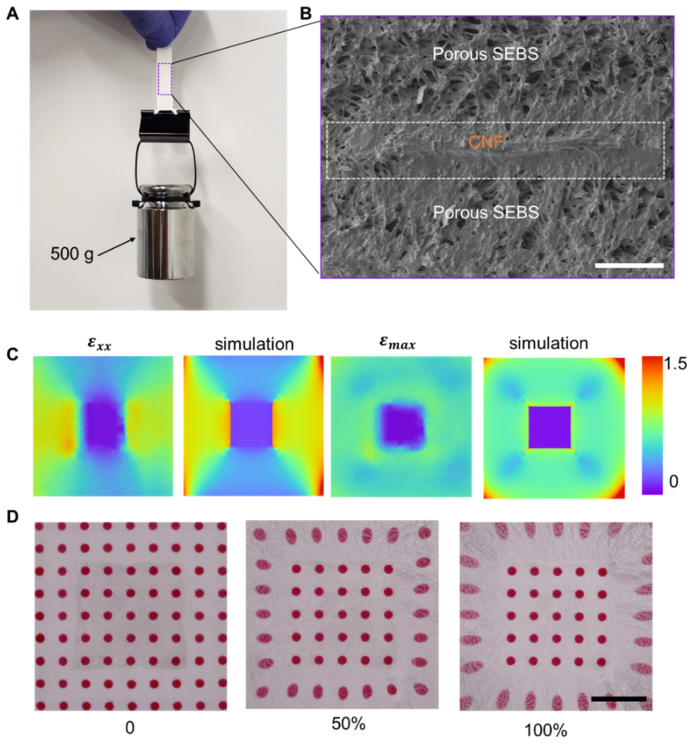


Figure 4.10. Strong interfaces between CNF and porous SEBS. **A**, The optical image of the CNF interfaced porous SEBS, which is capable for supporting a weight of 500 g. **B**, The cross-section SEM image of the sandwich structure interface (porous SEBS on both sides and CNF at the center). Scale bar: 100 µm. **C**, DIC results and correspond FEA simulation of the rectangle CNF strain island under strain and strain visualization of the red dots on CNFI on porous SEBS. The color bar represents the strain. **D**, The red dots remain stable under different strains, demonstrating the excellent performance of the CNFI for strain isolation. Scale bar: 1 cm.

The efficacy of the CNFI in enabling strain isolation functions across various wearable electronics scenarios has been rigorously assessed. **Figure 4.11A** and **B**

demonstrates that conductive patterns on the CNFI maintain stable electrical resistance under 100% strain for both uniaxial and biaxial stretching while a bitable resistance increase (more than 10, 000, 000-fold increase under 100% strain)) was observed for pattern on porous SEBS. Notably, optical images of these conductive patterns (**Figure 4.11A** inset) reveal no obvious deformation for the patterns on the CNFI (highlighted

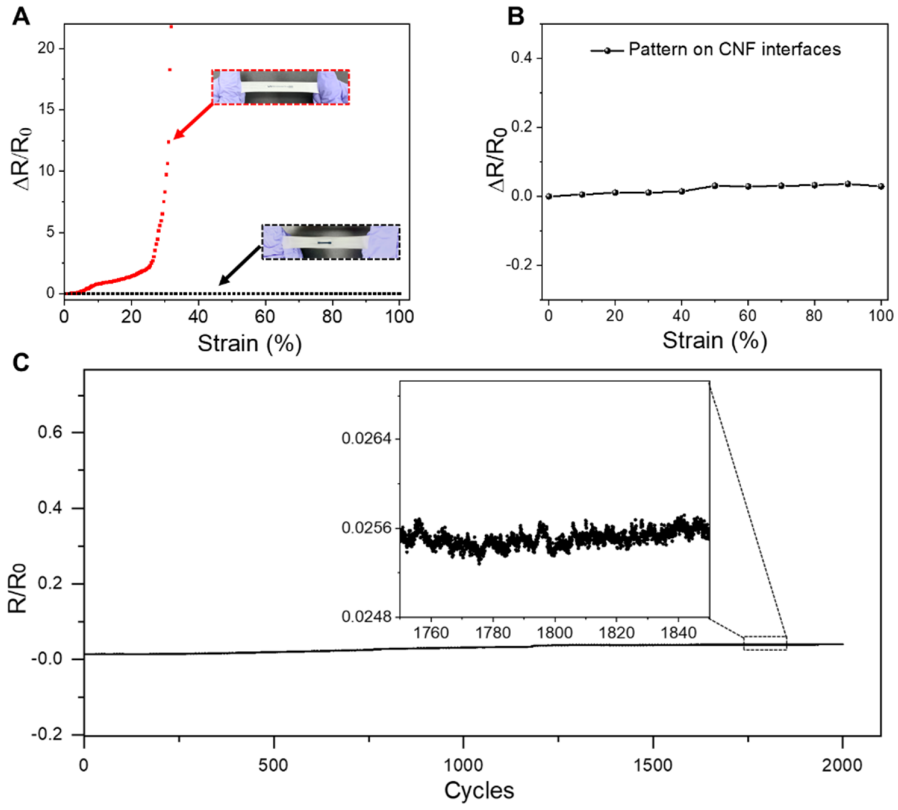


Figure 4.11. Electronmechanical performances of conductive patterns on CNFI. **A**, Relative resistance changes (R/R_0) of the printed conductive pattern on porous SEBS (red) and CNFI on porous SEBS substrate (black) as a function of uniaxial strains. The insets are the corresponding optical images of the patterns under stretch. **B**, Relative resistance changes (R/R_0) of conductive path on CNFI as a function of biaxial strains. **C,** Resistance changes of the conductive path on CNFI on porous SEBS to cyclic stretching under 50% strain.

in black), in stark contrast to patterns on porous SEBS, which exhibit apparent fractures (indicated in red). This observation underscores the superior durability and reliability of the conductive pattern on the CNFI, which shows a marginal resistance

change of approximately 2.55% even after undergoing 2000 stretching cycles at 50% strain, as presented in **Figure 4.11C**.

Furthermore, the impedance of the skin–electrode interface for the printed PEDOT: PSS/Ag NWs electrode on the CNFI remains almost unchanged (~1.5% change at 100 Hz) when subjected to 100% strain (**Figure 4.12A**), while an noticeable increase in impedance (over 500% at 100 Hz) was observed for the electrodes printed on porous SEBS (**Figure 4.12D**) The robustness of the interfaces in preserving the functionality

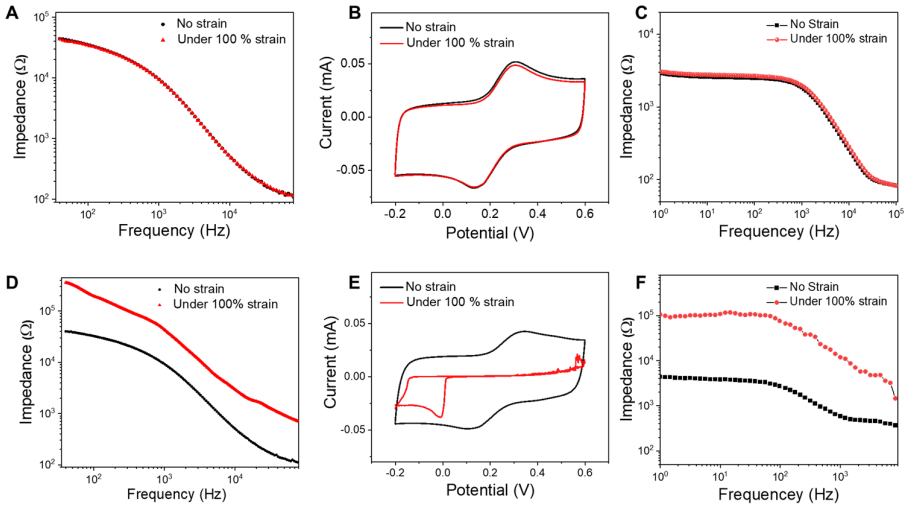


Figure 4.12. Performances comparison of various electrodes on CNFI and porous SEBS under strain. **A-C**, Skin impedance, cyclic voltammograms (**B**) and EIS (**C**) comparison of the PEDOT: PSS electrodes on CNFI: no strain(black) versus under 100% strain (red). **D-F**, Skin impedance (**D**), cyclic voltammograms (**E**) and EIS (**F**) comparison of the PEDOT: PSS electrodes on porous SEBS: no strain(black) versus under 100% strain (red). Electrochemical tests (B, C, E and F) are conducted in 0.1 M KCl solution containing 10 mM $[Fe(CN)_6]^{3-/4-}$.

of wearable electronics is further demonstrated by the cyclic voltammetry (CV) curves (**Figure 4.12B**) and electrochemical impedance spectroscopy (EIS) analyses (**Figure 4.12C**). These tests reveal that printed PEDOT: PSS electrodes on the CNFI maintain stable electrochemical activity even under 100% strain. While electrodes situated on porous SEBS exhibit compromised functionality under similar strain conditions, as

depicted in **Figure 4.12E** and **F**.

Leveraging the CNFI' strain isolation capabilities on porous SEBS matrix, various of stretchable electronic devices, including a wireless powering system, ECG sensors, and biochemical sensors, have been. A quantitative assessment of LED brightness powered by the wireless powering system validates the operational stability and reliability of antenna fabricated on the CNFI under 100% strain (**Figure 4.13A-C**). Conversely, antenna on porous SEBS exhibits rapid degradation and electrical failure under a mere 20% strain (**Figure 4.13A**, red).

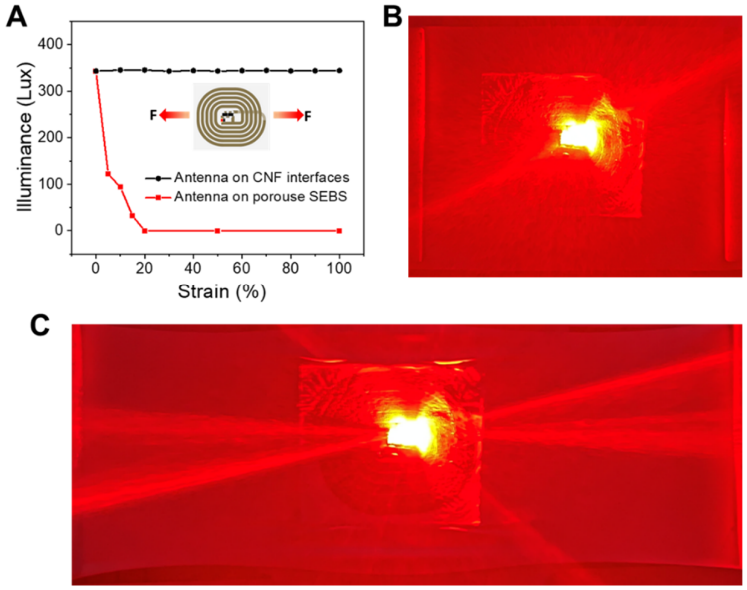


Figure 4.13. Performances comparison of wireless power transmitter system printed on CNFI and porous SEBS under strain. **A**, Quantitative brightness of the LED wirelessly powered by the transmitter printed on the CNFI and bare porous SEBS under strain. Insets is the design of the wireless powering system. **B**, Optical images of the LED wirelessly powered by the transmitter printed on the CNFI under stretching of 0 (**B**) and 100% (**C**).

ECG recordings obtained from electrodes on the CNFI demonstrate negligible signal deterioration, with a signal-to-noise ratio (SNR) of 28.7 dB prior to strain application and 28.4 dB under 100% strain (**Figure 4.14**, top). In comparison, ECG

signals from electrodes on porous SEBS exhibit a comparable SNR of 28.5 dB in the absence of strain but become indiscernible at 100% strain (**Figure 4.14**, bottom).

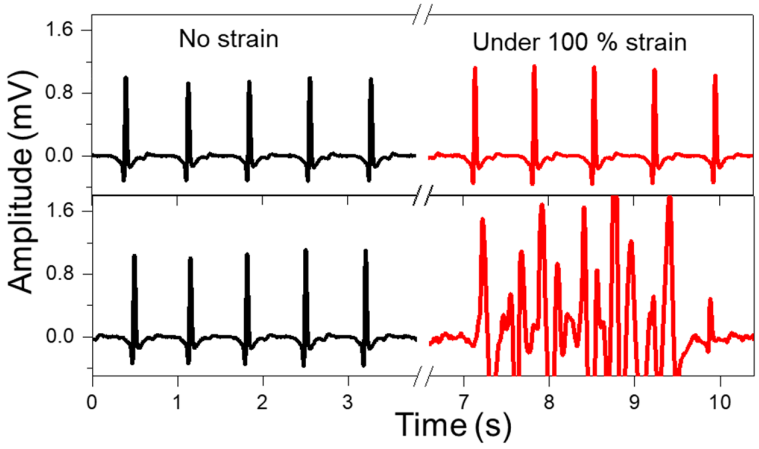


Figure 4.14. ECG signals recorded using the electrodes printed on the CNFI (top) and bare porous SEBS (bottom) under no strain (black)100% strain (red).

Beyond electrochemical sensors based on voltammetry (**Figure 4.12B**), we also test stretchable sensors for Na^+ sensor based on open-circuit potential (OCP) (**Figure 4.15**).

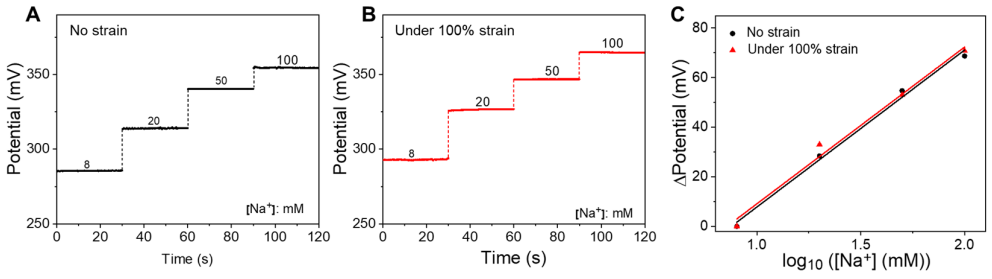


Figure 4.15. Performance of Na^+ sensors pinted on CNFI under strain. **A**, Dynamic OCP responses of the Na^+ sensor under no strain **(A)** and 100% strain **(B). C**, Calibration of Na^+ sensors printed on the CNFI tested under no strain (black) and under 100% strain (red). The sensitivity is 63.33 mV/decade and 63.21 mV/decade for the sensors under no strain and 100% strain, respectively, demonstrating its excellent strain-resilience performances.

The sensor exhibits stable sensitivity (less than 0.2% sensitivity change) even under 100% strain, marking important advancements in the field of stretchable and wearable

bioelectronics.

4.4 Design and characterization of the CNFI for MFCs

The inherent abundance of carboxyl groups within cellulose renders it naturally hydrophilic, thereby facilitating the penetration of aqueous liquids into its fibril matrix. This characteristic is pivotal for the fabrication of MFCs designed for the continuous collection and transfer of sweat. As depicted in **Figure 4.16A**, water mixed with dye is efficiently dispersed across custom-designed cellulose patterns without diffusing into the adjacent porous SEBS substrates. Prior to the MFCs design, an investigation into the liquid wicking kinetics of the cellulose channel was undertaken. This involved measuring the travel distance and corresponding time for channels of varying widths (**Figure 4.16B**) and thicknesses (**Figure 4.16C**). **Figure 4.16B** reveals that for a constant channel thickness of 0.2 mm, the travel distance within the channel increases with the channel width over the same time. Similarly, **Figure 4.16C** illustrates that for a channel of constant width (2 mm), the travel distance increases with channel thickness over a given time.

Applying the simplified Washburn equation (*34*) allows for the calculation of liquid travel speed within the microfluidic channels,

$$L = D\sqrt{t}$$

where L is the travel distance, D is the diffusion coefficient depending on the tube size and liquid properties and t is the travel time. And the calculated D values of channels with specific thickness of 0.2 mm are 2.18 $mm/s^{1/2}$ for 1 mm width, 2.60 $mm/s^{1/2}$ for 2 mm width, and 3.28 $mm/s^{1/2}$ for 3 mm width. And travel speeds of channels for fixed width of 2 mm are 2.24 $mm/s^{1/2}$ for 0.15-mm of thickness, 2.87 $mm/s^{1/2}$ for 0.25-mm thickness.

Leveraging the insights gained from the liquid travel speed calculations, a MFC

system was meticulously designed to enhance sweat collection efficiency. This system features a thickness of 0.2 mm, with eight inlets converging into an outlet channel.

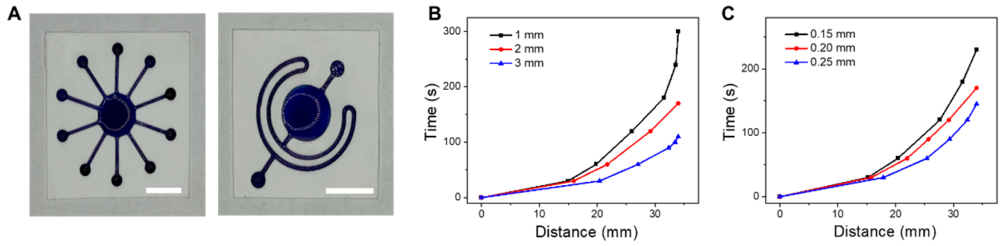


Figure 4.16. Liquid diffusion on CNFI. **A**, Customized CNF patterns on porous SEBS wetted by blue ink. Scale bar: 5 mm. **B**, Relationship between liquid travel time and travel distance in the MFC with varying channel widths. **C**, Relationship between liquid travel time and travel distance in the MFC with varying channel thickness.

The outlet channel is characterized by a length of 8.7 mm and a width of 1 mm, as illustrated in **Figure 4.17**. This configuration achieves a wicking rate of 13 µl min^{-1}, ensuring the timely collection and discharge of sweat, which is critical for maintaining the integrity of sweat analysis over extended periods of wear.

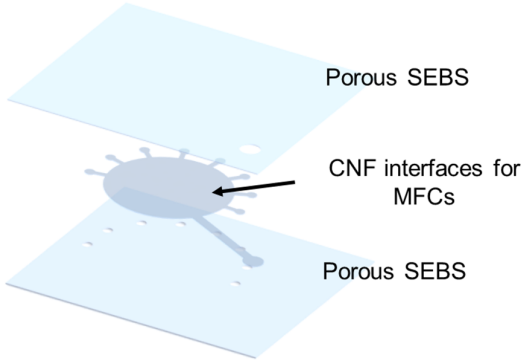


Figure 4.17. Schematic illustration of the design of MFC, which includes two SEBS layer on both side and CNFI at the center.

The on body sweat sampling experiment (**Figure 4.18A**) showcases the MFC capability for rapid sweat collection. Notably, the sensing chamber achieved complete filling approximately 7 minutes after sweat induction via iontophoresis, which agrees

well with the results of FEA simulation (**Figure 4.18B**).

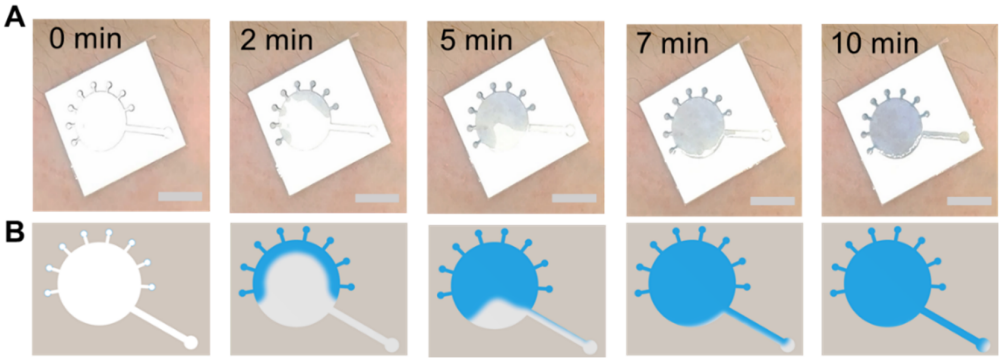


Figure 4.18. Filling progress of the CNFI based MFCs. **A**, Photographic images of the MFC sweat filling during an iontophoresis induced sweat sampling process. Scale bar: 5 mm. **B**, FEA simulation of the microfluidic filled process by sweat.

To further explore the performances of MFCs, FEA is employed to examine the refresh time in response to changes in the concentration of biomarkers, specifically β-HB and glucose. The analysis focused on the time required for the MFC system to adjust to 90% of a new solution concentration following a change. For a concentration shift of β-HB from 0.5 mM to 1.2 mM, the refresh time is found to be approximately 3.8 minutes, as depicted in **Figure 4.19A**. A streamline diagram representing the 200 s mark (**Figure 4.19B**) illustrates the direction and state of sweat flow within the system. Additionally, when evaluating the refresh time for varying concentrations of β-HB - specifically changes from 0.5 mM to 1.1 mM and from 0.5 mM to 1.3 mM, the system demonstrated refresh times of 3.6 minutes (for 1.1 mM) and 4 minutes (for 1.3 mM), respectively, as shown in **Figure 4.19C**. This indicates minimal variation in refresh time despite differing concentration changes. The experimental data for β-HB concentrations over time (**Figure 4.19D**) correlates closely with the simulation results, validating the cellulose-based MFC's ability to rapidly update in response to changes in sweat composition.

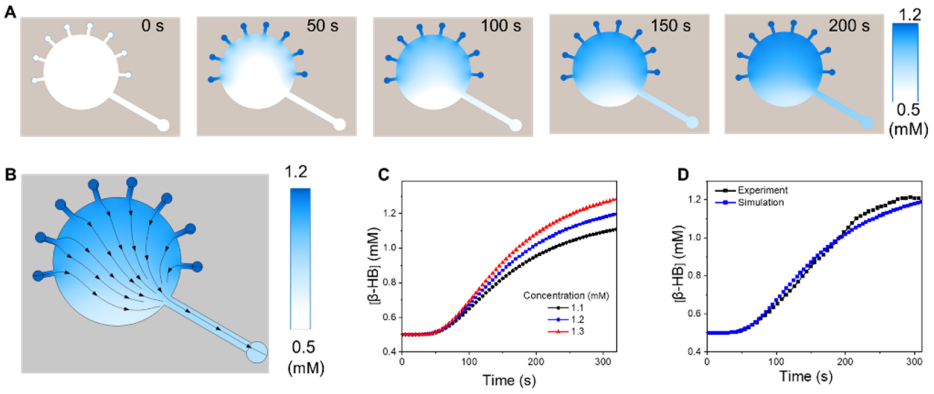


Figure 4.19. Refreshing progress of the CNFI based MFCs for β-HB. **A**, FEA simulation of the microfluidic refreshing process of the β-HB for a change from 0.5 mM to 1.2 mM. **B**, Fluidic diagram obtained from the FEA simulation at the 200s of the MFCs. **C**, Simulations of the time evolution of the concentration change for refreshing using β-HB solutions with different concentrations. **D**, Comparison of the time evolution of the concentration changes obtained by FEA simulation and experimental result. β-HB, β- hydroxybutyrate.

Parallel outcomes were observed for the glucose sensor, as detailed in **Figure 4.20**. This confirmation underpins the potential of CNFI based MFCs for real-time monitoring in practical applications, offering a promising solution for continuous health and wellness tracking through non-invasive sweat analysis.

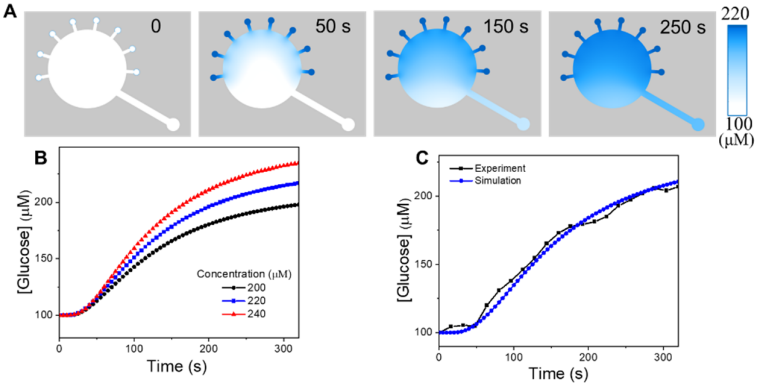


Figure 4.20. Refreshment process of the glucose in the MFC. **A**, FEA simulation of the microfluidic refreshing process of the glucose for a change from 100 uM to 220 uM. **B**, fluidic diagram obtained from the FEA simulation at the 200s of the MFC. **C**, comparison of the time evolution of the concentration change obtained by FEA simulation and experimental results.

4.5 Antimicrobial, biocompatibility and hemocompatibility study

The prolonged and continuous application of on-skin wearable devices raises concerns about vulnerability to pathogenic bacteria, such as Methicillin-resistant *Staphylococcus aureus* (MRSA), *Escherichia coli* (*E. Coli*), and *Pseudomonas aeruginosa* (*PA*). To mitigate this issue, epsilon polylysine (ε-PL) was incorporated into the porous SEBS matrix, and the antimicrobial properties of the material were evaluated. The results, as presented in **Figure 4.21A**, demonstrate that the ε-PL-enhanced porous SEBS exhibits outstanding antibacterial efficacy, achieving greater than 99.9% bactericidal activity against MRSA, *E. Coli*, and *PA*. The antibacterial activity of the ε-PL-enhanced porous SEBS was further confirmed using a live/dead assay, where live bacteria were stained green and dead bacteria were stained red. The results showed a significant increase in the number of dead cells (stained red) compared to the control group, indicating the effectiveness of the ε-PL-enhanced porous SEBS against bacterial growth (**Figure 4.21B**). This high level of antimicrobial performance is attributed to the ability of ε-PL to disrupt the bacterial membrane structures. Furthermore, it was observed that the inclusion of printed inks does not detrimentally affect the antibacterial properties of the material.

To assess the biocompatibility of these materials, cytotoxicity test was conducted using a variety of human cell lines, including the keratinocyte cell line (HaCaT), human dermal fibroblast (HDF-α), myeloid leukemia cell line (U937), and promyelocytic leukemia cell line (HL-60). The results, detailed in **Figure 4.21C** and **D**, indicate no significant differences ($P > 0.05$) in cell viability between cells cultured with the ε-PL-integrated porous SEBS and the control group. Further, results revealed similar cell morphology in the ε-PL-integrated porous SEBS-treated group and the control group. Additionally, the use of ε-PL and the PEDOT: PSS/AgNWs patterns

were observed to have no adverse impact on the biocompatibility of the substrates.

Subsequently, to assess the blood compatibility of the developed material, a hemolysis assay was performed. The hemolysis results of all the developed materials elucidated negligible hemolysis (~3.2 ± 0.5%), which falls in the safe range (*35, 36*). These results underscore the potential of ε-PL-enhanced porous SEBS as a promising material for on-skin wearable devices, offering both effective antimicrobial protection, excellent biocompatibility and hemocompatibility.

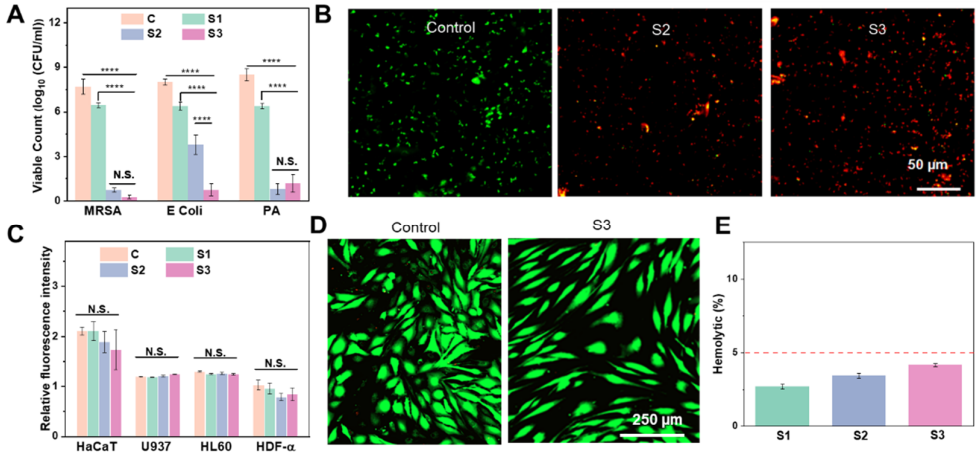


Figure 4.21. Antimicrobial, biocompatibility and hemocompatibility study. **A**, Bactericidal activity against MRSA, *E. Coli*, and *PA* on various materials for 6 hours. **B**, Live/Dead staining of MRSA on various materials 6 hours. **C**, Cell viability of various materials after 5 days. **D**, Live/Dead staining of HDF cells on control and S3. **E**, Hemolysis (%) of various materials against erythrocyte cells. C: control; S1: porous SEBS; S2: porous SEBS with ε-polylysine; S3 porous SEBS with ε-polylysine and PEDOT: PSS/Ag NWs.

4.6 Wireless and multimodal metabolism types monitoring

β-HB is the principal component of ketone bodies, predominantly synthesized during periods of fasting. Besides its crucial role in managing type 1 diabetes, where excessive production of β-HB poses risks and can lead to diabetic ketoacidosis, β-HB also plays a vital role in energy metabolism, brain health, and gene expression, and

serves as an essential biomarker for monitoring metabolic states (*37, 38*). To enable real-time monitoring of metabolic states and β-HB concentration levels in the human body, we have developed a multimodal bioelectronic device (**Figure 4.22)**. This device integrated with β-HB sensors, glucose sensors and EEG sensors fabricated on CNF interfaced porous SEBS substrates. By integrating with a mobile data acquisition circuit, the device can achieve in situ data processing and wireless data transmission via Bluetooth Low Energy.

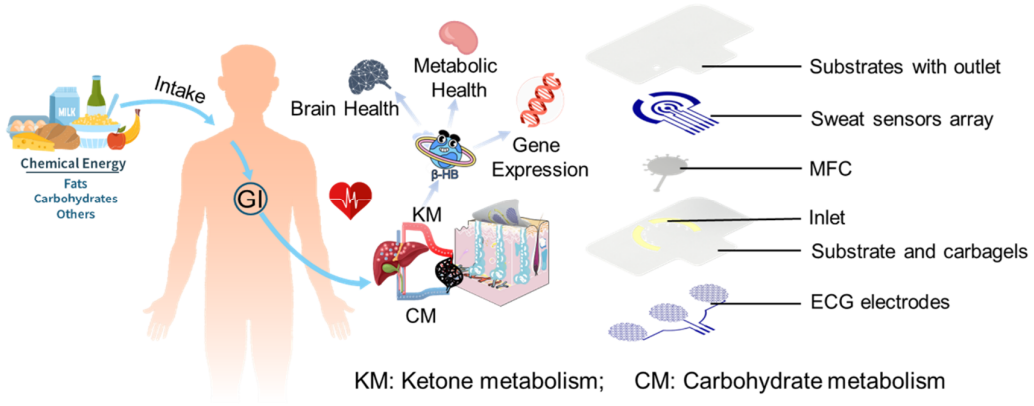


Figure 4.22. Illustration of the CNFI enhanced wearable bioelectronics that continuously monitor multimodal biochemicals and ECG from skin for diverse metabolism monitoring.

β-HB sensors are constructed by immobilizing β-hydroxybutyrate dehydrogenase (HBD) and nicotinamide adenine dinucleotide (NAD^+) onto electrodes that are decorated with the electron mediator toluidine blue O (TBO). The oxidation of β-HB to acetoacetate (AcAc) leads to the conversion of NAD^+ to NADH, which can be detected by TBO, facilitating their transfer to the working electrodes for detection, as illustrated in **Figure 4.23A**. The electrode, prior to its functionalization with HBD and NAD^+ on the working electrodes, demonstrates excellent sensing performance for NADH. This is validated by the dynamic current response, the linearity of the calibration plot, and selectivity (**Figure 4.23B-D**). The exceptional performance of the β-HB sensors was also demonstrated by similar results, as shown in **Figure 4.23E-G**.

Furthermore, over a prolonged period of 7 days, the β-HB sensors exhibited good stability, as depicted in **Figure 4.23H**.

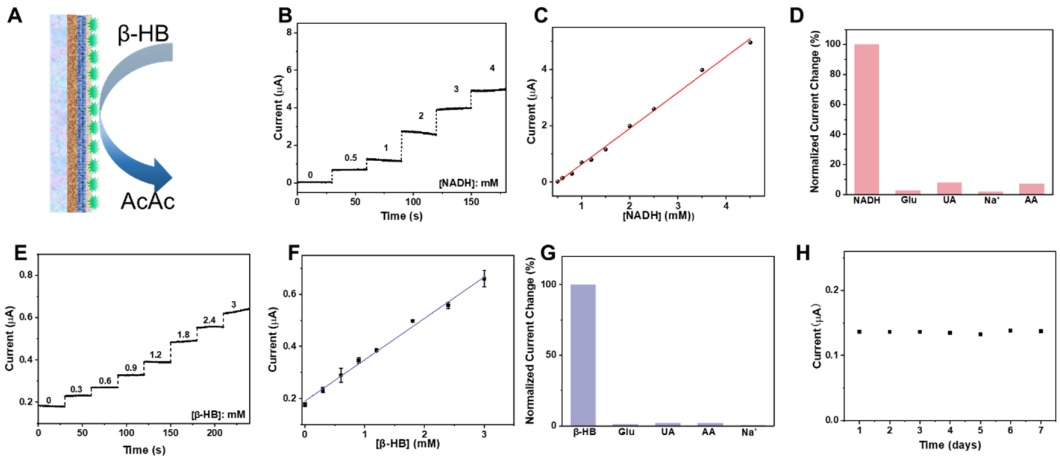


Figure 4.23. Characterizations of the nicotinamide adenine dinucleotide (NADH) and β-hydroxybutyrate (β-HB) sensors. **A**, Detection mechanism of β-HB where the electrodes include PEDOT: PSS base electrodes, gold nanoparticles, and decorated toluidine blue O and β-hydroxybutyrate dehydrogenase. **B**, dynamic current responses to different NADH concentrations from 0 to 4 mM, calibration plot (**C**), and selectivity test (**D**) of the NADH sensors. **E-H**, dynamic current responses to different β-hydroxybutyrate concentrations from 0 to 3 mM, calibration plot (**F**), selectivity test (**G**) and stability test of the β-hydroxybutyrate sensors All the tests were conducted in 0.1 M phosphate buffer solution (pH: 6.0). R^2 is 0.996 for the line fit in (**C**). The sensitivity is ~1.27 μA/mM and the limit of detection is ~0.02 mM. R^2 is 0.994 for the line fit in (**F**). The sensitivity is ~158.6 nA/mM and the limit of detection is ~0.015 mM.

The glucose sensors were fabricated based on the PEDOT: PSS based electrodes and gold nanoparticles (25 nm) were first deposited with by sputter. Next, Prussian blue solution was added by dropping coasting. The glucose sensors were finalized by the addition of the glucose oxidase mixed solution and Nafion on the decorated electrodes followed by the drying under 4 °C. As shown in **Figure 4.24**, the obtained glucose sensors exhibit excellent performances, demonstrated by the dynamic current response (**Figure 4.24A**), the linearity of the calibration plot (**Figure 4.24B**),

selectivity (**Figure 4.24C**) and stability (**Figure 4.24D**).

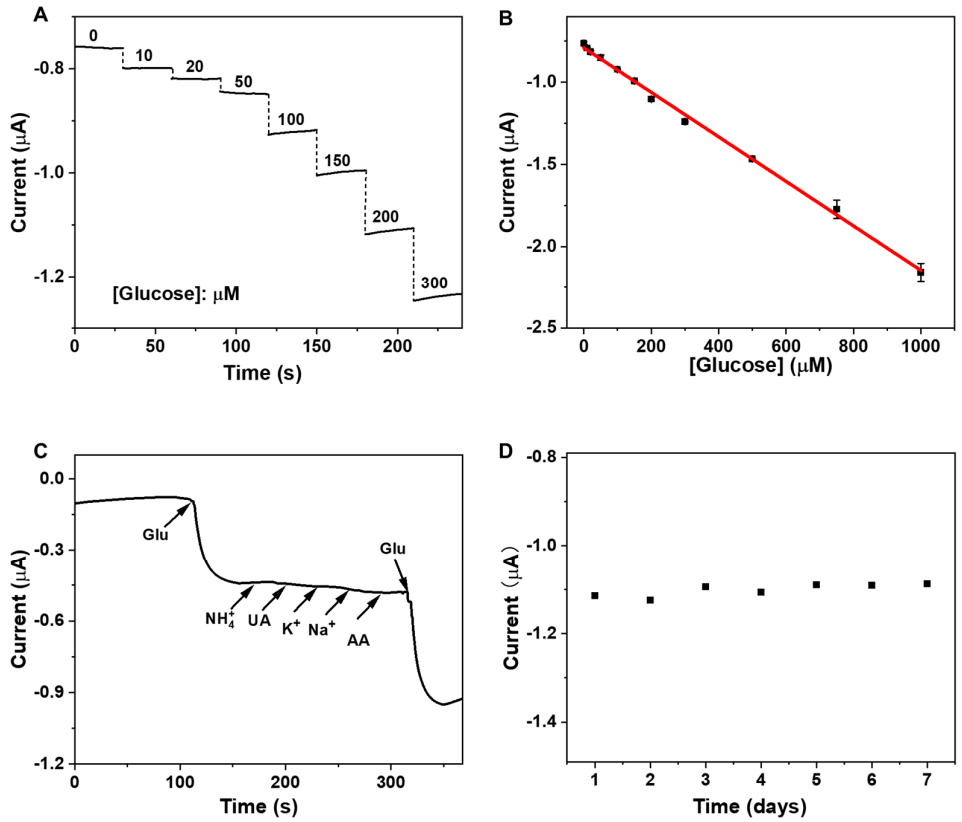


Figure 4.24. Characterizations of the glucose sensor. Dynamic current responses to different glucose concentrations from 0 to 300 μM (**A**), calibration plot (**B**), selectivity test (**C**) and stability test (**D**) of the glucose sensors. All the tests were conducted in 0.1 M phosphate buffer solution (pH: 6.0). R^2 is 0.997 for the line fit in (**B**). The sensitivity is ~1.35 nA/μM and the limit of detection is ~1.82 μM.

Both the β-HB sensors and glucose sensors show stable sensitivity under 100% strain as displayed in **Figure 4.25**. The incorporation of MFCs enables long-term and stable monitoring of β-HB and glucose levels in sweat, heart rate (HR), heart rate variability (HRV, indicated by the standard deviation of R-R intervals, SDRR), and energy expenditure (EE), all of which contribute to monitoring metabolism types.

The devices were employed to monitor those signals under different metabolic conditions, as depicted in **Figure 4.25A**and **B**. Here, we find that the volunteer after fasting for 12 hours exhibits a low glucose concentration, while a relatively high β-HB

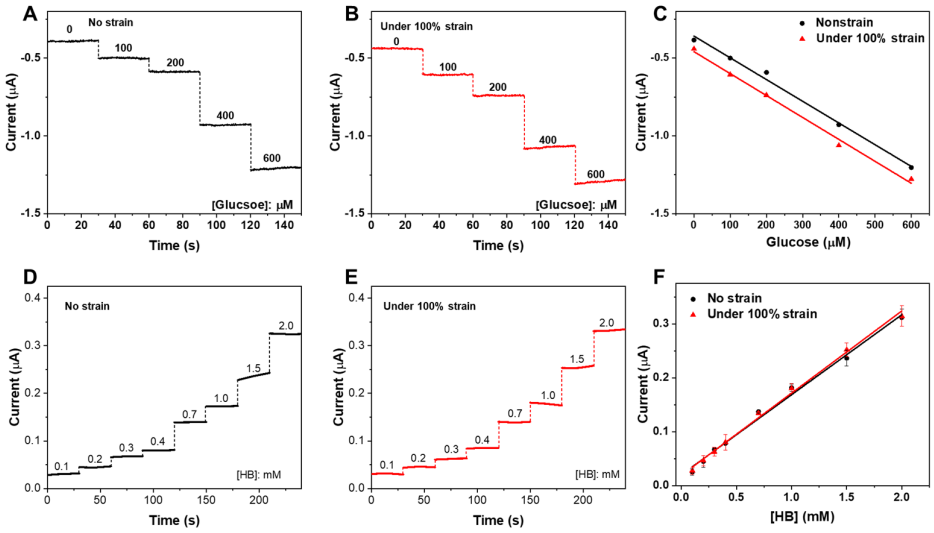


Figure 4.25. Characterizations of the glucose and β-HB sensors under strain. **A**, Dynamic current responses of the glucose sensor with no strain, under 100% strain (**B**) and corresponding calibration plots (**C**). **D**, Dynamic current responses of the β-HB sensors with no strain, under 100% strain (**E**) and corresponding calibration plots (**F**). The sensitivity is ~1.40 nA/mM and ~1.41 nA/mM for the β-HB sensors under no strain and 100% strain respectively, demonstrating the excellent strain-resilience performances of CNFI in β-HB sensors.

levels in sweat. In the first scenario, representing typical ketone metabolism, the fasting volunteer consumed keto drink, resulting in an increase in β-HB levels and a further decrease in glucose levels. This trend persisted until the intake of carbohydrates (**Figure 4.26A**). In another scenario under carbohydrate metabolism, the fasting volunteer consumed bread, leading to a sharp decline in β-HB levels and an increase in glucose levels, with glucose levels gradually decreasing over time, while the opposite trend was noted for β-HB levels. The consumption of a keto drink further increased β-HB concentrations, as shown in **Figure 4.26B**. In addition to the biochemicals monitoring, HR and HRV were also successfully tracked and the increase in HR and a decrease in HRV due to cycling were observed in both scenarios (**Figure 4.26A** and **B**).

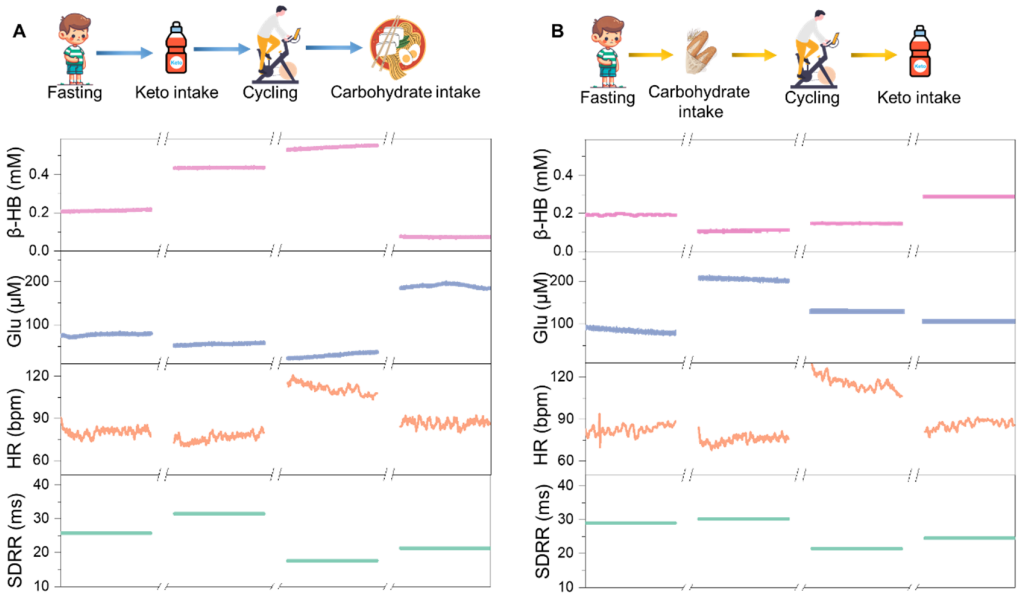


Figure 4.26. On body evaluation of the CNFI enhanced wearable bioelectronics for diverse metabolism monitoring**. A**, Multimodal monitoring of β-HB and glucose in sweat, together with ECG during a ketone-dominated metabolic processes. **B**, Multimodal monitoring of β-HB and glucose in sweat, together with ECG during a carbohydrate-dominated metabolic processes. β-HB, β-hydroxybutyrate; Glu, glucose; HR, heart rate; bpm, beats per minute; SDRR, standard deviation of R-R interval.

4.7 Conclusion

Through the integration of CNFI with porous substrates, our research marks substantial progress in the realms of surface smoothing, strain isolation, and the application of MFCs, culminating in the high-quality fabrication of sensors with unparalleled operational stability under strain. This innovation highlights the adaptability and scalability of CNFI across diverse substrates, such as porous SEBS in this work, heralding new avenues in the creation of sophisticated, multimodal wearable technologies. Our discoveries laid the groundwork for spotlighting the extensive potential of CNFI to refine device manufacturing and functionality. This leap forward promises profound advancements in personalized healthcare and precision medicine.

4.8 Materials and methods

Materials. 2,2,6,6-tetramethylpiperidine-1-oxyl (TEMPO), sodium bromide (NaBr), sodium hypochlorite (NaClO), sodium hydroxide (NaOH), sodium chloride (NaCl), uric acid (UA), ascorbic acid (AA), glucose. glucose oxidase, toluidine blue O (TBO), β-hydroxybutyrate dehydrogenase from Pseudomonas lemoignei (EC 1.1.1.30, 25 UN) β-nicotinamide adenine dinucleotide hydrate (oxidized form), β-nicotinamide adenine dinucleotide (reduced), Tris−HCl buffer solution (1 M, pH 7.5) were purchased from Sigma-Aldrich. Chloroform, PBS buffer solutions and Dulbecco's modified Eagle's medium (DMEM), RPMI 1640, fetal bovine serum (FBS) penicillin-streptomycin were purchased from Fisher Scientific.

Preparation of CNF. 10 g of softwood pulp were thoroughly dispersed in 500 mL of distilled water (DI) under vigorous stirring. Subsequently, 0.16 g of TEMPO, 1 g of NaBr, and 30 mL of NaClO solution (12.5 wt% in water) were added sequentially into the dispersion to initiate the cellulose oxidation process. Throughout this procedure, the solution's pH was maintained at approximately 10 by the addition of NaOH solution, until the solution transitioned from yellow to colorless and maintained the stable pH. Following overnight stirring, the CNF was washed with DI water several times until the pH approached 7. The final CNF product was dried at 60°C and stored for subsequent use.

Preparation of CNF ink. The CNF ink was created by dispersing the previously obtained CNF into water at a specific ratio, followed by sonication using a Branson SFX550 tip at 30% amplitude for 30 minutes. For the long CNF inks, the amplitude of the sonication is adjusted to 20%. The mixed ink was prepared by combining L-CNF with short CNF inks at a predetermined ratio.

Preparation of bifunctional inks for extrusion printing. The preparation of the

bifunctional ink commenced with the freeze-drying of the PEDOT: PSS solution (Clevios™ PH1000, Heraeus Electronic Material) over a duration of 72 hours, to yield PEDOT: PSS nanofibrils. Subsequently, these nanofibrils were re-dispersed in water to achieve a concentration of 10 wt% using a planetary mixer (AR-100, THINKY). The preparation of the bifunctional inks proceeded with the incorporation of 5% silver nanowire (Ag NWs) ink (in water and EG with a mass ratio of 3:2) into the 10% PEDOT: PSS inks with different ration according to the applications. To adjust the final concentration of PEDOT: PSS to 5% in the ink, additional EG, (3-Glycidyloxypropyl) Trimethoxysilane (GOPS), and water were added. The solvent composition was finalized to water and EG with a mass ratio of 4:1, and the GOPS mass was adjusted to 5% of the PEDOT: PSS mass.

Printing procedure. The extrusion printing process was performed utilizing a benchtop robotic system (Fisnar F4200N) equipped with a 3-axis micropositioning stage, adhering to a predefined patterning protocol. The composite CNF ink underwent extrusion printing onto plasma-treated, porous SEBS substrates following a specific programmed pattern. Subsequently, the bifunctional inks were deposited onto the designated CNF regions in accordance with the targeted application to achieve high-resolution printouts. The inkjet printing phase was carried out employing a specialized Microelectronic printer (Scientific 3, Mi Fang Electronics), tailored for precision in microfabrication tasks.

Fabrication of cellulose based MFCs. The MFC was prepared by initially dispersing softwood pulp in water with a concentration of 30 mg ml^{-1} under vigorous stirring. This mixture was then transferred, measuring 10 mL, into a petri dish with a diameter of 90 mm and subsequently subjected to drying in an oven at 60°C, facilitating the formation of a cellulose membrane. Post-drying, the membrane

underwent a hot-pressing procedure for 10 minutes, applying a pressure of 20 MPa and a temperature of 120°C, to yield a densified membrane structure. The final membrane was then precisely cut into the pre-designed structure utilizing a CO_2 laser to obtain the MFC.

Fabrication of biochemical sensors. The glucose-sensing electrode was prepared by functionalizing the PEDOT: PSS electrode with thick Au nanoparticles, Prussian blue, and glucose oxidase using our previously published procedures. The β-HB sensor was developed by the functionalizing of the PEDOT: PSS electrodes with thick Au nanoparticles, TBO, and β-hydroxybutyrate dehydrogenase.

Characterizations and measurements. The SEM images were taken with FEI Quanta 600F Environmental SEM Helios Hydra UX DualBeam SEM. TEM images were collected with JEOL JEM-1400 TEM. Surface roughness were measured using optical profilometer (Vecco NT 9109). Dantec Dynamics Digital Image Correlation (DIC) was used for the measurement of the strain change during stretch. Electrophysiological measurements were validated and conducted using PowerLab T26 (AD Instruments) and Electrochemical characterizations were conducted using an electrochemical station (CHI660E, CH Instruments Inc.) The electronic mechanical tests were conducted with dual-channel source meter (2604B, Keithley Instruments) and Mark-10 ESM303 tensile tester.

Antibacterial activity. The investigation into the antibacterial effectiveness of developed materials S1, S2, and S3 was validated against three bacterial strains: MRSA (USA300), *E. Coli* and *Pseudomonas aeruginosa* E411-17 (*PA).* The samples were separately added to 1 ml of respective bacterial suspension (10^8 CFU/ml) in PBS and incubated at 37 ^oC for 6h. At the set time point, following the dilution of a bacterial solution by a factor of 1000, 10 µl the solution was spread onto the LB-agar

plate and the log reduction of bacteria was calculated as follows:

Log reduction = log (cell count of control) – log (survivor count in the treatment group)

Additionally, a live-dead assay was conducted to assess the viability of bacteria. This was achieved using the LIVE/DEAD Bacterial Viability Kit from Invitrogen.

Cytocompatibility and hemocompatibility assay. The cytotoxicity of the developed materials was assessed in four different cell lines: HaCaT, HDF, U937, and HL 60, as reported(*8*). Briefly, for HaCaT, and HDF, DMEM media supplemented with 10 % FBS and 1% penicillin-streptomycin was used to culture, while an RPMI 1640 media supplemented with 10 % FBS and 1% penicillin-streptomycin was used to grow U937 and HL 60. The cells were seeded in a 48-well plate at a density of 10^4 cells/well, and the sterilized and precut (1 x 1 cm) samples were transferred to each well using well-inserts. The cells were incubated at 37 ºC for 3 days, and cell toxicity was determined by adding 20 µL CCK-8 per well, and absorbance was measured at 450 nm using a microplate reader. In addition, following staining using the LIVE/DEAD cell viability kit, the cells were examined using an inverted fluorescence microscope.

Hemolysis test. The hemolysis assay performed to examine the blood compatibility of the developed materials as reported earlier. The anticoagulated human blood was centrifuged at 1500 rpm for 10 minutes, and the pellet of RBCs that had been obtained was washed with 1x PBS. Subsequently, the RBCs were diluted to achieve a final RBC concentration of 10.0% (v/v). 200 µl of the aforementioned solution was added to each sample and kept for 1 h at 37 ºC. Later, the samples were collected after centrifugation and absorbance was measured at 540 nm. Additionally, the positive control (100 %) was generated using 1% Triton-X, while the negative control (0 %) was prepared without any treatment.

Experimental setup, and numerical simulations of CNF interfaced strain isolation. The FEA simulations for biaxial tensile tests, as depicted in Figure 4.7b, and Figure 4.78, and Figure 4.10C, were conducted utilizing COMSOL Multiphysics version 6.0. Within these simulations, the "Stationary Study" feature was engaged through the "Solid Mechanics Interface." A hyperelastic, incompressible Mooney-Rivlin model, characterized by five parameters, was employed for the analysis. The prescribed displacements are applied on the gripped region and the strain and stress field are calculated in region near the CNF. In addition, the biaxial tensile test was performed in a biaxial tensile machine, and the 3D Digital Image Correlation (DIC) System Q-400 (Dantec Dynamics, Tonsbakken, Skovlunde, Denmark) was used for displacement field measurements.

Numerical simulations of sweat dynamics in microfluidics. All simulations in Figure. 4.18- Figure. 4.20 were carried out utilizing COMSOL Multiphysics version 6.0. To simulate the process of sweat filling in an empty cellulose channel, a computational fluid dynamics module (Two-Phase Flow, Level Set interface) was used in Fig. 4e. Additionally, the solute diffusion was modeled using a combination of the "Transport of Diluted Species Interface" and the "Laminar Flow Interface". The concentration of the solute at the center of the circular channel was monitored over time to determine the refresh time.

4.9 References

1. S. Lee, S. Franklin, F.A. Hassani, T. Yokota, O.G. Nayeem, Y. Wang, R. Leib, G. Cheng, D.W. Franklin, T. Someya, Nanomesh pressure sensor for monitoring finger manipulation without sensory interference, *Science* **370**, 966-970 (2020) .

2. Y. Luo, M.R. Abidian, J.-H. Ahn, D. Akinwande, A.M. Andrews, M. Antonietti, Z. Bao, M. Berggren, C.A. Berkey, C.J. Bettinger, Technology roadmap for flexible sensors. *ACS Nano*

17, 5211-5295 (2023)

3. A. Miyamoto, S. Lee, N.F. Cooray, S. Lee, M. Mori, N. Matsuhisa, H. Jin, L. Yoda, T. Yokota, A. Itoh, M. Sekino, H. Kawasaki, T. Ebihara, M. Amagai, T. Someya, Inflammation-free, gas-permeable, lightweight, stretchable on-skin electronics with nanomeshes, *Nat. Nanotechnol.* **12**, 907-913 (2017).

4. Y. Xu, B. Sun, Y. Ling, Q. Fei, Z. Chen, X. Li, P. Guo, N. Jeon, S. Goswami, Y. Liao, S. Ding, Q. Yu, J. Lin, G. Huang, Z. Yan, Multiscale porous elastomer substrates for multifunctional on-skin electronics with passive-cooling capabilities, *Proc. Natl. Acad. Sci. U. S. A.* **117**, 205-213 (2020).

5. B. Zhang, J. Li, J. Zhou, L. Chow, G. Zhao, Y. Huang, Z. Ma, Q. Zhang, Y. Yang, C.K. Yiu, J. Li, F. Chun, X. Huang, Y. Gao, P. Wu, S. Jia, H. Li, D. Li, Y. Liu, K. Yao, R. Shi, Z. Chen, B.L. Khoo, W. Yang, F. Wang, Z. Zheng, Z. Wang, X. Yu, A three-dimensional liquid diode for soft, integrated permeable electronics, *Nature* **628**, 84–92 (2024).

6. Z. Ma, Q. Huang, Q. Xu, Q. Zhuang, X. Zhao, Y. Yang, H. Qiu, Z. Yang, C. Wang, Y. Chai, Z. Zheng, Permeable superelastic liquid-metal fibre mat enables biocompatible and monolithic stretchable electronics, *Nat. Mater.* **20**, 859–868 (2021).

7. J. Li, Y. Fu, J. Zhou, K. Yao, X. Ma, S. Gao, Z. Wang, J.G. Dai, D. Lei, X. Yu, Ultrathin, soft, radiative cooling interfaces for advanced thermal management in skin electronics, *Sci. Adv* **9**, eadg1837 (2023).

8. Y. Xu, Y. Su, X. Xu, B. Arends, G. Zhao, D.N. Ackerman, H. Huang, S.P. Reid, J.L. Santarpia, C. Kim, Z. Chen, S. Mahmoud, Y. Ling, A. Brown, Q. Chen, G. Huang, J. Xie, Z. Yan, Porous liquid metal-elastomer composites with high leakage resistance and antimicrobial property for skin-interfaced bioelectronics, *Sci. Adv*. **9**, eadf0575 (2023).

9. P. Wang, X. Ma, Z. Lin, F. Chen, Z. Chen, H. Hu, H. Xu, X. Zhang, Y. Shi, Q. Huang, Y. Lin, Z. Zheng, Well-defined in-textile photolithography towards permeable textile electronics, *Nat. Commun*. **15**, 887(2024).

10. X. Ma, P. Wang, L. Huang, R. Ding, K. Zhou, Y. Shi, F. Chen, Q. Zhuang, Q. Huang, Y. Lin, Z. Zheng, A monolithically integrated in-textile wristband for wireless epidermal biosensing, *Sci. Adv.* **9**, eadj2763 (2023).

11. G. Zhao, Y. Ling, Y. Su, Z. Chen, C.J. Mathai, O. Emeje, A. Brown, D.R. Alla, J.

Huang, C. Kim, Laser-scribed conductive, photoactive transition metal oxide on soft elastomers for Janus on-skin electronics and soft actuators, *Sci. Adv*. **8**, eabp9734 (2022).

12. S. Zhang, Y. Zhou, A. Libanori, Y. Deng, M. Liu, M. Zhou, H. Qu, X. Zhao, P. Zheng, Y.-L. Zhu, J. Chen, S.C. Tan, Biomimetic spinning of soft functional fibres via spontaneous phase separation, *Nat. Electron*. **6**, 338–348 (2023).

13. H. Liu, H. Li, Z. Wang, X. Wei, H. Zhu, M. Sun, Y. Lin, L. Xu, Robust and Multifunctional Kirigami Electronics with a Tough and Permeable Aramid Nanofiber Framework, *Adv. Mater.* **50**, 2207350 (2022).

14. Y.-S. Guan, F. Ershad, Z. Rao, Z. Ke, E.C. da Costa, Q. Xiang, Y. Lu, X. Wang, J. Mei, P. Vanderslice, C. Hochman-Mendez, C. Yu, Elastic electronics based on micromesh-structured rubbery semiconductor films, *Nat. Electron.* **5**, 881-892 (2022).

15. Z. Jiang, N. Chen, Z. Yi, J. Zhong, F. Zhang, S. Ji, R. Liao, Y. Wang, H. Li, Z. Liu, Y. Wang, T. Yokota, X. Liu, K. Fukuda, X. Chen, T. Someya, A 1.3-micrometre-thick elastic conductor for seamless on-skin and implantable sensors, *Nat. Electron.* **5** ,784-793 (2022).

16. L. Xu, S.R. Gutbrod, A.P. Bonifas, Y. Su, M.S. Sulkin, N. Lu, H.J. Chung, K.I. Jang, Z. Liu, M. Ying, C. Lu, R.C. Webb, J.S. Kim, J.I. Laughner, H. Cheng, Y. Liu, A. Ameen, J.W. Jeong, G.T. Kim, Y. Huang, I.R. Efimov, J.A. Rogers, 3D multifunctional integumentary membranes for spatiotemporal cardiac measurements and stimulation across the entire epicardium, *Nat. Commun.* **5**, 3329 (2014).

17. Y. Hui, Y. Yao, Q. Qian, J. Luo, H. Chen, Z. Qiao, Y. Yu, L. Tao, N. Zhou, Three-dimensional printing of soft hydrogel electronics, *Nat. Electron.*, **5**, 893-903 (2022).

18. B. Lee, H. Cho, S. Moon, Y. Ko, Y.-S. Ryu, H. Kim, J. Jeong, S. Chung, Omnidirectional printing of elastic conductors for three-dimensional stretchable electronics, *Nat. Electron.* **6**, 307-318 (2023).

19. A.G. Kelly, T. Hallam, C. Backes, A. Harvey, A.S. Esmaeily, I. Godwin, J. Coelho, V. Nicolosi, J. Lauth, A. Kulkarni, S. Kinge, L.D. Siebbeles, G.S. Duesberg, J.N. Coleman, All-printed thin-film transistors from networks of liquid-exfoliated nanosheets, *Science* **356** ,69-73 (2017).

20. M. Kuang, L. Wang, Y. Song, Controllable printing droplets for high-resolution patterns, *Adv. Mater.* **26**, 6950-6958 (2014).

21. J. Lessing, A.C. Glavan, S.B. Walker, C. Keplinger, J.A. Lewis, G.M. Whitesides, Inkjet printing of conductive inks with high lateral resolution on omniphobic "R(F) paper" for paper-based electronics and MEMS, *Adv. Mater.* **26**, 4677-4682 (2014).

22. W. Wang, S. Wang, R. Rastak, Y. Ochiai, S. Niu, Y. Jiang, P.K. Arunachala, Y. Zheng, J. Xu, N. Matsuhisa, X. Yan, S.-K. Kwon, M. Miyakawa, Z. Zhang, R. Ning, A.M. Foudeh, Y. Yun, C. Linder, J.B.H. Tok, Z. Bao, Strain-insensitive intrinsically stretchable transistors and circuits, *Nat. Electron.* **4**,143-150 (2021).

23. Y. Zhao, B. Wang, J. Tan, H. Yin, R. Huang, J. Zhu, S. Lin, Y. Zhou, D. Jelinek, Z. Sun, K. Youssef, L. Voisin, A. Horrillo, K. Zhang, B.M. Wu, H.A. Coller, D.C. Lu, Q. Pei, S. Emaminejad, Soft strain-insensitive bioelectronics featuring brittle materials, *Science* **378**, 1222-1227(2022).

24. D. Zhong, C. Wu, Y. Jiang, Y. Yuan, M.G. Kim, Y. Nishio, C.C. Shih, W. Wang, J.C. Lai, X. Ji, T.Z. Gao, Y.X. Wang, C. Xu, Y. Zheng, Z. Yu, H. Gong, N. Matsuhisa, C. Zhao, Y. Lei, D. Liu, S. Zhang, Y. Ochiai, S. Liu, S. Wei, J.B. Tok, Z. Bao, High-speed and large-scale intrinsically stretchable integrated circuits, *Nature* **627**, 313-320 (2024).

25. T. Li, C. Chen, A.H. Brozena, J.Y. Zhu, L. Xu, C. Driemeier, J. Dai, O.J. Rojas, A. Isogai, L. Wagberg, L. Hu, Developing fibrillated cellulose as a sustainable technological material, *Nature* **590**, 47-56 (2021).

26. D. Cao, Y. Xing, K. Tantratian, X. Wang, Y. Ma, A. Mukhopadhyay, Z. Cheng, Q. Zhang, Y. Jiao, L. Chen, H. Zhu, 3D Printed High-Performance Lithium Metal Microbatteries Enabled by Nanocellulose, *Adv. Mater.* **31**, 1807313 (2019).

27. E. Abraham, V. Cherpak, B. Senyuk, J.B. ten Hove, T. Lee, Q. Liu, I.I. Smalyukh, Highly transparent silanized cellulose aerogels for boosting energy efficiency of glazing in buildings, *Nat. Energy* **8**, 381–396 (2023).

28. U. Mogera, H. Guo, M. Namkoong, M.S. Rahman, T. Nguyen, L. Tian, Wearable plasmonic paper-based microfluidics for continuous sweat analysis, *Sci. Adv.* **8** ,eabn1736 (2022).

29. B. Zhong, X. Qin, H. Xu, L. Liu, L. Li, Z. Li, L. Cao, Z. Lou, J.A. Jackman, N.J. Cho, L. Wang, Interindividual- and blood-correlated sweat phenylalanine multimodal analytical biochips for tracking exercise metabolism, *Nat. Commun.* **15**, 624 (2024).

30. N.W. Bartlett, M.T. Tolley, J.T. Overvelde, J.C. Weaver, B. Mosadegh, K. Bertoldi,

G.M. Whitesides, R.J. Wood, SOFT ROBOTICS. A 3D-printed, functionally graded soft robot powered by combustion, *Science* **349**, 161-165 (2015).

31. Y. Chen, Z. Deng, R. Ouyang, R. Zheng, Z. Jiang, H. Bai, H. Xue, 3D printed stretchable smart fibers and textiles for self-powered e-skin, *Nano Energy* **84**, 105866 (2021).

32. Y. Zhou, D. Jiang, R. Sharma, Y.M. Xie, A. Singh, Enhancement of 3D printed cementitious composite by short fibers: A review, *Constr. Build. Mater.* **362**, 129763 (2023).

33. P. Langan, Y. Nishiyama, H. Chanzy, A Revised Structure and Hydrogen-Bonding System in Cellulose II from a Neutron Fiber Diffraction Analysis, *J. Am. Chem. Soc.* **121**, 9940-9946 (1999).

34. M. Liu, J. Wu, Y. Gan, D.A.H. Hanaor, C.Q. Chen, Evaporation Limited Radial Capillary Penetration in Porous Media, *Langmuir* **32**, 9899-9904 (2016).

35. Y. He, X. Cheng, T. Zhou, D. Li, J. Peng, Y. Xu, W. Huang, beta-Hydroxybutyrate as an epigenetic modifier: Underlying mechanisms and implications, *Heliyon* **9**, e21098 (2023).

36. R. de Cabo, M.P. Mattson, Effects of Intermittent Fasting on Health, Aging, and Disease, *N. Engl. J. Med.* **381**, 2541-2551 (2019).

37. P. Singh, S.M. Andrabi, U. Tariq, S. Gupta, S. Shaikh, A. Kumar, Functionally multifaceted scaffolds delivering bioactive compounds for treatment of infectious chronic and ischemic wounds, *Chem. Eng. J.* **457**, 141359 (2023).

38. B. Fatma, S.M. Andrabi, S. Gupta, V. Verma, A. Kumar, C. Pitsalidis, A. Garg, Biocompatible, breathable and degradable microbial cellulose based triboelectric nanogenerator for wearable transient electronics, *Nano Energy* **114**, 108628 (2023).

Chapter 5. Conclusion

This dissertation presents a series of innovative advancements in the field of skin-interfaced bioelectronics, showcasing the development of novel materials and fabrication techniques that significantly enhance the functionality, applicability, and sustainability of wearable and implantable devices. The research initially focused on leveraging commonplace materials like pencils and paper to create on-skin electronic devices capable of performing real-time, continuous, and high-fidelity monitoring of a broad spectrum of vital biophysical and biochemical signals. The qualities of these devices are comparable to those obtained through conventional methods, yet they offer the added benefits of flexibility, biodegradability, and cost-effectiveness. Advancing further, the dissertation explores the laser scribing of metallic conductive materials on soft elastomers, introducing a method to embed bioelectronics directly onto tissue-like surfaces with high electrical conductivity and biocompatibility. This technique supports the development of responsive bioelectronics, including soft actuators and sensors that adapt to dynamic environmental stimuli and biological signals, enhancing the interaction between electronic devices and biological systems. To address the challenges associated with the mechanical and electrical performance of stretchable bioelectronics, a novel in-situ phase separation method was developed to create conductive elastic composites. These materials maintain their electrical properties under extreme deformation, dramatically reducing the percolation threshold and enhancing the durability and functionality of bioelectronic devices under physiological conditions. Finally, the research incorporates advanced material science techniques to refine the surface properties and integrate microfluidic functionalities into porous bioelectronics, using CNF interfaces. This approach not only smoothens the surface textures for improved printing quality but also ensures robust performance under

mechanical strain, making these devices particularly suitable for continuous monitoring and management of health-related biomarkers.

Overall, this dissertation contributes to the broader field of bioelectronics by integration of these innovative materials and methods paves the way for the next generation of bioelectronics that can seamlessly interface with human tissue, offering more natural and effective monitoring and therapeutic solutions. Future research should focus on scaling these technologies for mass production and exploring their long-term reliability and safety in clinical settings.

VITA

Ganggang Zhao earned his Bachelor of Engineering in Chemical Engineering and Technology from Central South University, Changsha, China, in 2016. He completed his Master of Engineering in 2019 under the supervision of Prof. Xiaobo Ji at the same university. In 2019, he began his pursuit of a Doctor of Philosophy degree in the Department of Mechanical and Aerospace Engineering at the University of Missouri-Columbia, under Prof. Zheng Yan's guidance. Over the past 5 years, his research primarily focuses on the development and fabrication of innovative on-skin wearable electronics and devices for long-term, real-time, and non-invasive health monitoring and has published 12 research works. Among them, four are first/co-first authored research works in world-known prestigious journal like *Nature Nanotechnology*, *Science Advances*, *Proceedings of National Academy of Sciences of the United States of America*, and *Advanced Functional Materials*. Additionally, he has two first/co-first authored manuscripts that will be submitted. The publications are listed below:

1. **Zhao, G**.; Chen, Z.†; Wang, S.; Chen, S.; Xu, Y.; Zhang, F.; Ouyang, Q.; Andribi, S. M.; Su, Y.; Qian, X.; Shi, L.; Ling, Y.; Xie, J.; Yan, Z. "Multifunctional Cellulose Nanofibril Interfaces for High-Quality Printing, Strain Resilience, and Microfluidics in Porous Bioelectronics". ***To be submitted*** (2024).
2. **Zhao, G**.†; Ling, Y.†; Su, Y.; Chen, Z.; Mathai, C.; Emeje, O.; Brown, A.; Alla, D.; Huang, J.; Kim, C.; Chen, Q.; He, X.; Stalla, D.; Xu, Y.; Chen, Z.; Chen, P.; Gangopadhyay, S.; Xie, J.; Yan, Z. "Laser-Scribed Conductive, Photoactive Transition Metal Oxide on Soft Elastomers for Janus on-Skin Electronics and Soft Actuators". ***Science Advances,*** **8**, 25, eabp9734. (2022)
3. Xu, Y.†; Ye, Z.†; **Zhao, G**.†; Fei, Q.; Chen, Z.; Li, J.; Yang, M.; Ren, Y.; Berigan, B.; Ling, Y.; Qian, X.; Shi, L.; Ozden, I.; Xie, J.; Gao, W.; Chen, P.; Yan, Z. "Phase-Separated Porous Nanocomposite with Ultralow Percolation Threshold Enables Strain-

Resilient Wireless Stretchable Bioelectronics." ***Nature Nanotechnology*** doi.org/10.1038/s41565-024-01658-6 (2024)

4. Ling, Y. †; **Zhao, G.** †; Su, Y.; Wu, Q.; Xu, Y.; Chen, Z. H.; Arends, B.; Emeje, O.; Huang, G.; Xie, J.; Yan., Z. "Skin-Inspired Porous Mesh Bioelectronics with Built-in Multifunctionality for Concurrently Monitoring Heart Electrical and Mechanical Functions." ***Advanced Functional Materials***, **33**, 2362681. (2023)
5. Xu, Y.†; **Zhao, G**. †; Zhu, L.; Fei, Q.; Zhang, Z.; Chen, Z.; An, F.; Chen, Y.; Ling, Y.; Guo, P.; Ding, S.; Huang, G.; Chen, P.-Y.; Cao, Q.; Yan, Z., "Pencil-paper on-skin Electronics." ***Proceedings of the National Academy of Sciences,*** **117** (31), 18292-18301. (2020)
6. Xu, Y.; Su, Y.; Xu, X.; Arends, B.; **Zhao, G.**; Ackerman, D. N.; Huang, H.; Reid, S. P.; Santarpia, J. L.; Kim, C.; Chen, Z.; Mahmoud, S.; Ling, Y.; Brown, A.; Chen, Q.; Huang, G.; Xie, J.; Yan, Z. "Porous Liquid Metal-Elastomer Composites with High Leakage Resistance and Antimicrobial Property for Skin-Interfaced Bioelectronics." ***Science Advances,*** **9**, 1, eadf0575. (2023)
7. Huang, L.; Liu, Y.; Li, G.; Song, Y.; Su, J.; Cheng, L.; Guo, W.; **Zhao, G.**; Shen, H.; Yan, Z.; Tang, B. Z.; Ye, R., "Ultrasensitive, Fast-Responsive, Directional Airflow Sensing by Bioinspired Suspended Graphene Fibers." ***Nano Letters,*** **23**, 2, 597. (2023)
8. Zhao, N.; Zhang, H.; Yang, S.; Sun, Y.; **Zhao, G.**; Fan, W.; Yan, Z.; Lin, J.; Wan, C. "Direct Induction of Porous Graphene from Mechanically Strong and Waterproof Biopaper for On-Chip Multifunctional Flexible Electronics." ***Small,*** **6**, 2300242. (2023)
9. Ling, Y.; Pang, W.; Liu, J.; Page, M.; Xu, Y.; **Zhao, G.**; Stalla, D.; Xie, J.; Zhang, Y.; Yan, Z. "Bioinspired Elastomer Composites with Programmed Mechanical and Electrical Anisotropies." ***Nature communications,*** **13**, 1, 524. (2022)
10. Zheng, B.; **Zhao, G.**; Yan, Z.; Xie, Y.; Lin, J. "Direct Freeform Laser Fabrication of 3D Conformal Electronics." ***Advanced. Functional. Materials***. **3**, 2210084 (2022).
11. Xu, Y.; Fei, Q.; Page, M.; **Zhao, G.**; Ling, Y.; Chen, D.; Yan, Z. "Laser-Induced Graphene for Bioelectronics and Soft Actuators." ***Nano Research*****, 44**, 23033-3050. (2021)
12. Xu, Y.; Fei, Q.; Page, M.; **Zhao, G.**; Ling, Y.; Stoll, S. B.; Yan, Z. "Paper-based wearable electronics." ***Isciences*****, 24**, 7, 102476. (2021)
13. Ling, Y.; Pang, W.; Li, X.; Goswami, S.; Xu, Z.; Stroman, D.; Liu, Y.; Fei, Q.; Xu, Y.; **Zhao, G.**; Sun, B.; Xie, J.; Huang, G.; Zhang, Y.; Yan, Z. "Laser-Induced Graphene for Electrothermally Controlled, Mechanically Guided, 3D Assembly and Human-Soft Actuators Interaction." ***Advanced Materials,*** **32**, 17, 1908475. (2020)